uOttawa

L'Université canadienne
Canada's university

FACULTÉ DES ÉTUDES SUPÉRIEURES ET POSTOCTORALES

uOttawa

L'Université canadienne
Canada's university

FACULTY OF GRADUATE AND POSDOCTORAL STUDIES

Vahesan Srirajasingam
AUTEUR DE LA THÈSE / AUTHOR OF THESIS

M.A.Sc (Electrical Engineering)
GRADE / DEGREE

School of Information Technology and Engineering
FACULTÉ, ÉCOLE, DÉPARTEMENT / FACULTY, SCHOOL, DEPARTMENT

Design and Fabrication of an Optical Fiber Interrogation Instrumentation System

TITRE DE LA THÈSE / TITLE OF THESIS

J. Yao
DIRECTEUR (DIRECTRICE) DE LA THÈSE / THESIS SUPERVISOR

CO-DIRECTEUR (CO-DIRECTRICE) DE LA THÈSE / THESIS CO-SUPERVISOR

EXAMINATEURS (EXAMINATRICES) DE LA THÈSE / THESIS EXAMINERS

B. Syrett

T. Yeap

Gary W. Slater
Le Doyen de la Faculté des études supérieures et postdoctorales / Dean of the Faculty of Graduate and Postdoctoral Studies

DESIGN AND FABRICATION OF AN OPTICAL FIBER INTERROGATION INSTRUMENTATION SYSTEM

By

Srirajasingam Vahesan

A Thesis submitted to the Faculty of Graduate Studies and Postdoctoral Studies in partial fulfillment of the requirements for the degree of Master of Applied Science, Electrical Engineering

September 2006

Ottawa-Carleton Institute for Electrical and Computer Engineering

School of Information Technology and Engineering

University of Ottawa,

Ottawa, Ontario, Canada

Your file Votre référence
ISBN: 978-0-494-34112-4
Our file Notre référence
ISBN: 978-0-494-34112-4

Abstract

The design and fabrication of an Optical Fiber Interrogation Instrumentation System is studied in this thesis. The objective is to design a Fiber Bragg Grating Interrogation (FBGI) instrumentation system using a Fiber Fabry Perot Tunable Filter (FFP-TF). An FBGI instrumentation system is designed to monitor the back-reflected wavelength shifts from a Distributed Fiber Bragg Grating (DFBG) network and to interpret those wavelength shifts into environmental temperature, strain and pressure variations.

This thesis encapsulates the complete system development lifecycle, inclusive of an applied case study of an FBGI Instrumentation system for monitoring the movements of bedsore patients. Specifically, in this thesis, an overview of Fiber Bragg Grating based fiber-optic sensors and their applications are presented, a novel design and implementation of an FBG interrogation system is described, which includes a detailed study on embedding techniques of FBGs in carbon composite, and an analysis of the test results from different embedding configurations is included. The discussion combines the novel approaches taken to resolve multiple peaks and peak-splitting phenomena observed in the reflected spectrum. A novel approach to remove the undesired temperature effect during strain sensing has been illustrated using neutral layer embedding of temperature FBG sensors.

This thesis proposes the system architectures for the designs of a single-board microprocessor and a DAQ card based interrogation system using FFP-TF scanning technology. A 16-bit microprocessor ADSP-2181 from Analog Devices and a Data

Acquisition Card DAQ-6015 from National Instruments is used as the front-end signal-processing circuit. The electronics circuit is built on a 4-layer printed circuit board. By incorporating an optical switch in the design and implementing a multiplexing technique, more FBGs are detected. This novel approach is successful due to the quasi-static nature of the measured environmental changes.

This thesis demonstrates a detailed analysis and experiments on the optical path of the design. These involve design and verification of a 980-nm laser pump circuit, design and experiments of an ASE source and an EDFA design where it is shown that EDFA design is necessary to provide the required amplification to the reflected signal spectrum. In addition, EDFA gain flattening, FFP-TF characteristics verification, optical-receiver design and the like are described. It is demonstrated that co-directional pumping is better than counter-directional pumping. In addition, the dependency of EDFA gain on the wavelength, the input power of the signal and the length of the erbium doped fiber is discussed. Novel approaches such as linear segmentation and look-up table implementation are proposed to compensate for the non-linear characteristics of the FFP-TF filter. An innovative coarse and fine sampling technique is implemented to improve the sampling speed while keeping the tuning speed of FFP-TF low in the range of 100 – 300 Hz to achieve better resolution of the FFP-TF output. Finally recommendations are suggested for future work. In general the performance can be improved by running the signal processing algorithms on an on-board high-speed processor.

TABLE OF CONTENTS

LIST OF FIGURES

LIST OF TABLES

LIST OF SYMBOLS

n	RI of the materials between two mirrors in the filter
λ	Wavelength
λ_c	Cut-off wavelength
n_{eff}	Average RI of the material
Λ	Physical period of the fiber grating
η	Quantum efficiency
$\Re$	Responsivity
α	Attenuation factor
ADSP	Analog Devices Signal Processor
A*STAR	Agency for Science, Technology and Research
A/D	Analog to Digital Converter
ASE	Amplified Spontaneous Emission
CDMA	Code Division Multiplex Access
D	The distance between two mirrors in the filter
D/A	Digital to Analog Converter
DAQ	Data Acquisition
DFBGS	Distributed Fiber Bragg Grating System
DWDM	Dense Wavelength Division Multiplexing
DSP	Digital Signal Processor
E_g	Bandgap energy
EDFA	Erbium Doped Fiber Amplifier
EMI	Electro Magnetic Interference
FBG	Fiber Bragg Grating
FBGIS	Fiber Bragg Grating Interrogation System
FFP-TF	Fiber Fabry Perot Tunable Filter
FSR	Free Spectral Range
FWHM	Full Width Half Maximum
GUI	Graphical User Interface

I_{in}	Light intensity of input spectrum
I_t	Light intensity of transmission spectrum
I_r	Light intensity of reflection spectrum
I	Current
I_{th}	Threshold current
LD	Laser Diode
LPF	Low Pass Filter
M.A.Sc	Master of Applied Science
MQWLD	Multi Quantum Well Laser Diode
NTU	Nanyang Technological University
OPM	Optical Performance Monitor
OSA	Optical Spectrum Analyzer
OSNR	Optical Signal to Noise Ratio
PCB	Printed Circuit Board
PD	Photo Detector
NA	Numerical Aperture
V	Normalized Frequency
RI	Refractive Index
SDM	Space Division Multiplexing
TDM	Time Division Multiplexing
TIA	Trans-impedance Amplifier
UV	Ultra Violet
WDM	Wavelength Division Multiplexing

ACKNOWLEDGEMENTS

The optical interrogation system thesis has been a challenge and added invaluable experience to me. The success of the thesis would not have been possible without the continuous encouragement, leadership and support of my supervisors and the excellent assistance of my research partners at Nanyang Technological University/Singapore, new friends in the research team and my office staff. The dedicated teamwork and the supportive and conducive environment made the research experience pleasant and memorable.

First of all, I would like to express my sincere appreciation to my supervisor Prof. Jianping Yao for his precious advice, supervision, and priceless encouragement, which motivated me to conquer the difficulties, challenges faced and to do my finest work in the thesis for my M.A.Sc. Many thanks go to my co-supervisor Prof. Chao Lu of Nanyang Technological University, for allowing me to work at his laboratory. I would also like to thank Dr. Jian Zhong Hao Emily and Mr. Chin-Yi Liaw for their immense support and invaluable guidance during every experimental stage of the research. My sincere thanks go to Mr. Feng Zhang and Miss. Kai Hsing Goh for suggestions, discussions, and contributions during this thesis writing. I wish to recognize the invaluable support from Miss. Yang Shu and Mr. Jun Hong Ng during this thesis writing and fabricating and embedding the FBG sensors for the FBGI system. My sincere thanks go to my supervisors at work, Director Mr. Steve Wilson and Vice President Mr. Peter Galan, for granting me the time needed and for their encouragement.

Above all, I would like to thank my wife Mrs. Pushpashanthini Markandu, and children Master. Vahesan Purushothanan and Miss.Yaswini Vahesan for their understanding, support and loving encouragement through all the stages of this extremely challenging thesis.

Chapter 1

Introduction

1.1 Background

With the advance in technology and today's increased information processing requirements, it has become necessary to collect vital and sensitive information ubiquitously. By embedding smart sensors in the body of structures, these structures can be made smart to capture and encode the information about how they react to environmental perturbations. Captured information is passed to a built-in or remote sensing system for further data analysis such that propagation of irregularities and dynamics of the structure can be monitored in advance so as to avoid catastrophic failures [1]. Embedded sensors can find applications in areas such as aerospace, telecommunications, defense, civil structures, bio-medical, and chemical engineering. Fiber sensors are increasingly preferred to other types of sensors due to their properties such as being light weight, low loss, small in size, immune to electromagnetic fields, able to withstand high temperature and easy to embed during construction [1]. Fiber Bragg Gratings (FBGs) are one of the key components for fiber-optic sensing. In an optical sensing system, an FBG can act as a transducer to transform the parameters such as strain, pressure, temperature into optical domain parameters such as optical energy, phase, wavelength shifts, polarization and dispersion. The success of the fiber sensor system relies on the magnitude of transformation produced in the optical domain by the optical sensor being detected and measured accurately [1]. Choosing the type of fiber, the

embedding technique, compensation techniques and the detection mechanism are crucial in designing a fiber sensor technology based interrogation system.

1.2 Motivation

Due to the perceived advantages of Optical FBG sensors, industries and institutes are attracted towards using FBG sensor technology in their sensor applications and carrying out further research on the technology to benefit from the unique properties. The beneficial properties of an FBG sensor include electrical isolation, usability in high voltage environments, usability in high temperature environments, wide bandwidth, wavelength encoded information, independency of light intensity and high sensitivity. As such, FBG sensors may capture a large portion of the sensor market in the future. FBGs offer supplementary advantages such as their capability to be embedded in composites with ease, allowing for greater strength and range of sensitivity. Above all, FBGs can be configured as a sensor network together with multiplexing techniques such as TDM, WDM, SDM and CDMA.

1.3 Objectives and scope of this thesis

The objective of this thesis is to design and develop an interrogation instrumentation system to remotely process, monitor and record the signal spectrum reflected by embedded DFBGS (Distributed FBG System).

This will include study of:

(1) FBG fundamentals, existing applications, interrogation technologies, FBG fabrication and embedding techniques, and performance characterization of the embedded sensors.

(2) The FBG interrogation system design, which shall detect the wavelength shifts caused by pressure, strain and temperature, display the useful information in a graphical user interface and use the FFP-TF to scan and detect the reflected FBG spectrum.

(3) System integration, case study analysis of bed-sore patient monitoring, providing recommendations for future designs.

This thesis does not discuss the software implementation, though there will be some citations made for some key techniques such as sampling techniques, moving average filters and the like.

1.4 Major contributions

1. Theoretical study on Fiber Bragg Grating Sensors and different technologies of interrogation systems: A detailed study on existing fiber optic sensor technology is conducted and the advantages of FBG sensors over the other types of sensor technologies are illustrated. Different interrogation techniques are studied and their advantages and disadvantages are analyzed. FFP-TF based interrogation technique is proposed for quasi-static strain sensing.

2. FBG sensor fabrication and Embedding: FBGs are fabricated using the Phase Mask technique. The FBGs inscribed on the fiber are coated with acrylate and annealed at 100°C - 120°C to eliminate the fast decay of the modulated refractive index of the fiber. Bragg wavelengths change as the result of annealing has been observed across the FBGs. Apodization techniques are used to smoothly vary the intensity of the UV beam such that refractive index modulation can be smooth and not abrupt. It is demonstrated that by applying varied longitudinal strain on the fiber during fabrication, different Bragg wavelengths can be achieved when the fiber is relaxed.

   FBGs are embedded between carbon laminar to increase the strength, the linear sensing range and the sensitivity of the fiber sensors. Embedding techniques are studied and the FBGs are embedded in different configurations such as 0°-uni ply, 90°-uni ply on neutral layer and above/below the neutral layer. The performances of the embedded FBGs are characterized via the experimental results. It is

demonstrated that if the adjacent layers are at 90°-uni ply, it ruptures the fiber and results in multiple peaks. In addition, it is demonstrated that neutral layer embedding is not sensitive to any strain or pressure changes.

3. Electronic, optical circuit design and schematic capture: The selection of electronic components involves the analysis and feasibility study, limits and specification checking and verification. The electronic circuit is captured on the schematic using a Mentor Graphic schematic tool. The Electronics circuit design consists of microprocessor, memory, ADC, DAC, current controller, temperature controller, filter and noise suppression circuits, OP-Amps, power supply, linear regulators, reset circuit and other logics. In addition, the circuit consists of optical components such as Photo-diodes, FFP-TF, and a 980nm laser pump. Later, the microprocessor circuit is replaced by a DAQ card and an optical switch is incorporated to switch between FBG channels.

   The optical circuit design involves the optical component selection, verification, 980nm pump circuit design and verification, ASE source and EDFA design and experiments, gain flattening, measurements of signal power loss due to coupling and splicing, FFP-TF characterization, optical-receiver design and analysis. It is demonstrated that co-directional pumping is better than counter-directional pumping and EDFA gain is dependent on the wavelength, the input power of the signal and the length of the erbium doped fiber.

4. Printed Circuit Board (PCB) design and Board bring up: A four-layer PCB is designed to accommodate all the electronic circuits and to provide place holders for the necessary optical circuits. The PCB design involves footprint creation, layer stack-up definition, component grouping and placement, layout, provision for ground and power plane, gerber generation, fabrication, printed circuit board assembly and electrical testing. The bare board is inspected for open and short circuits and then the components are assembled. The circuit is tested for correct voltage and frequency levels to ensure correct operation before the software is downloaded. The source code provided by the manufacturer of ADSP-2181 is modified to fit to our custom needs to incorporate communication with ADC, DAC, display, PC and miscellaneous I/O port controls. For future versions, it is proposed that, by keeping all the processing algorithms on board, the efficiency of processing and speed performance can be substantially improved.

5. Verification and Testing: Verification and Testing are carried out on all three disciplines, namely Electronics, Optics and in Software. A case study is carried out with LABVIEW-based software and the DAQ-based system. SLED diode is replaced with a 980nm laser pump, the power supply circuit is re-designed to support enough current draw with less dissipation, a larger heat sink and a fan are added to keep the circuit away from thermal run-away, and current and temperature controllers are tuned to stabilize the 980nm laser pump. Op-Amp gains are adjusted to limit the input voltage to the ADC. Filtering circuits are tuned to suppress the ground and power line noise. Software is used to control the

processing speed, sampling speed and the FFP-TF tuning voltage speed. It is demonstrated that optimum FFP-TF tuning speed is between 100 Hz – 300 Hz. Fine and coarse sampling techniques are proposed to improve the tuning speed of the FFP-TF. Ripple noise is found in the ADC samples and moving average filters are implemented in the software to eliminate the ripple noise. Background ASE noise subtraction method is discussed to set the threshold in software to detect the peaks, after executing the background ASE noise subtraction from the EDFA amplified signals. Optical components and circuits are verified during FBG fabrication, FBG embedding, 980nm laser pump design, ASE source design, EDFA design and gain flattening, FFP-TF characterization, optical receiver design and gain adjustment of the Op-Amp.

1.5 Organization of the thesis

This thesis is organized into seven chapters. Chapter 1 presents an introduction to the thesis, highlighting its scope specifying its objectives, illustrating the major contributions and summarizing how this thesis is organized. Chapter 2 presents theoretical analyses on the fundamental working principles of the grating sensors to better understand the behavioral nature and the functional mathematical relationship of the fiber sensors. Chapter 3 presents a topic on applications of Fiber Optic Sensor and discusses fundamental approaches to sensing and monitoring. Chapter 4 presents an approach to the embedding methods of FBGs, discussing the results from different ways of embedding the FBGs, and the different behavioral effects of the embedded FBGs. Chapter 5 presents an approach to the FBGI system design and development in detail. Chapter 6 presents an approach to the system integration and analysis. Finally, Chapter 7 summarizes the efforts and presents recommendations for future enhancements of the design.

1.6 Summary

This chapter presented an introduction to the overall research. In this chapter, advantages of FBGs as a sensor over other sensors have been presented. In addition, the motivation behind selecting this research, the objectives of this research and the major contributions were described in detail.

Chapter 2

Grating Sensors and FBG Fundamentals

In this chapter, the fundamentals and structure of FBGs are studied and the mathematical relationships associated with temperature, strain and pressure variations are presented. The strain and temperature effects are discussed in detail.

2.1 Fundamentals of FBG structure

Fiber Bragg Gratings are in fact considered as filters for the light traveling in the optical waveguide. As shown in Figure 2-1, FBG reflects the wavelength λ_B that matches the grating period of the FBG and transmits the rest of the wavelengths.

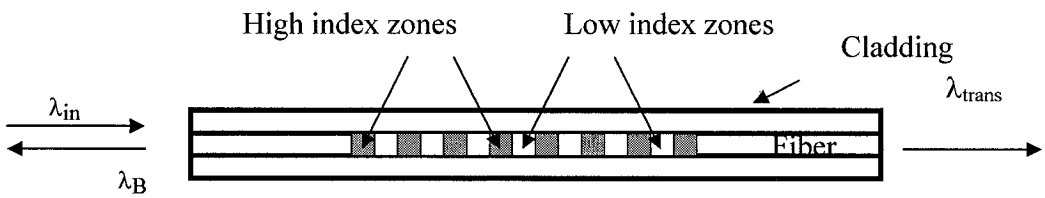

Figure 2-1 FBG structure showing High and Low index zones [3].

In general, simple forms of FBGs work like a chip filter and they stop and reflect a narrow band of light out of the full spectrum and pass through the rest of the light spectrum with little attenuation. However, FBGs can be made in such a way that they exhibit complex filter responses [2]. By inscribing the fiber with a laser, these spectral filters are made to inherently reside inside the same fiber that carries the light signal. FBGs are fabricated in the fiber by permanently modulating the refractive index (RI) of

the core along the length of the fiber using the interference pattern technique [3] [4] or the phase mask technique [3]. The fundamental attribute of an FBG is that the light at the center wavelength of the FBG is reflected backward. The operation mechanism of an FBG is based on the principle of Bragg condition and the reflection satisfying this condition is referred to as Bragg reflection. During the writing of the FBG, UV interference creates permanent alternating segments of High and Low RI regions as shown in Figure 2-1. The period of the written FBG is half of the period of the phase mask that is used to write the grating on the fiber [3]. When light travels through these periodically alternating regions of high and low RI, there is a certain amount of backward reflection that takes place at each interface [2]. The pitch between these high and low RI regions can be made such that all the partial reflections are additive in phase for a specific wavelength corresponding to a defined pitch length. The sum of the reflections at a particular wavelength that satisfies the "Bragg condition" would end up in constructive interference and would result in resonance. All the other wavelengths would result in high transmission. This is due to the out-of-phase partial reflections which result in destructive interference [2] [3].

Figure 2-2 shows the typical transmission and reflection spectrum of an FBG when a broadband light source is launched into an optical fiber that contains an FBG. In Figure 2-2, the transmission spectrum exhibits the characteristics that the broadband light has passed through a narrow band stop spectral filter. The FBG resonance wavelength, which is the center wavelength of the back-reflected light, will be decided by the effective refraction index of the core and the periodicity of the grating.

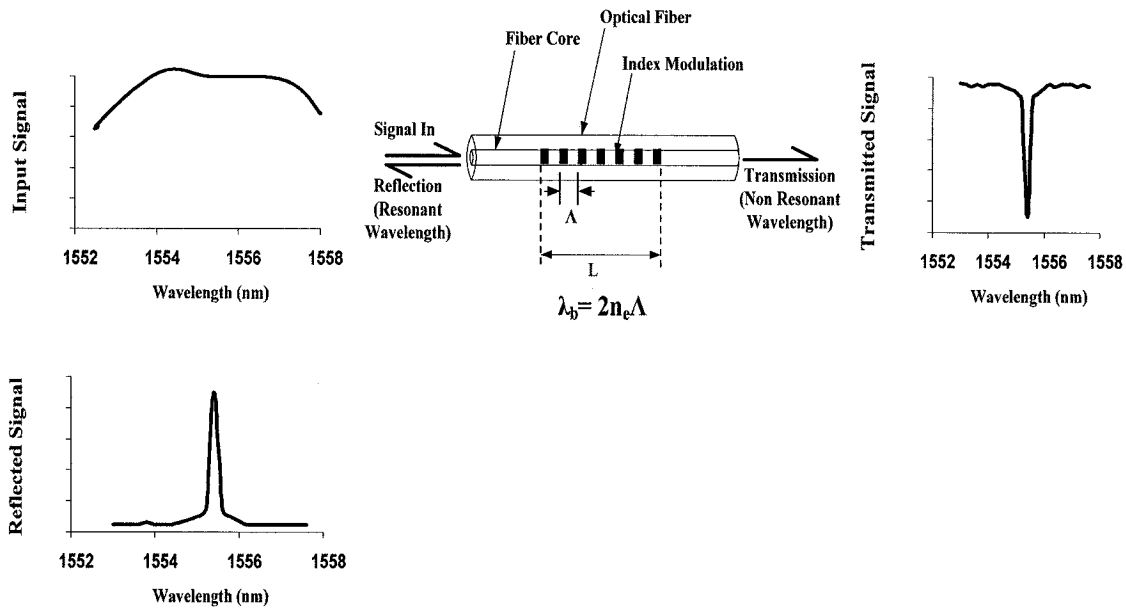

Figure 2-2 Transmission and reflection spectrum of an FBG [3].

The Bragg wavelength or the center wavelength of the reflected band of spectrum is defined by [3]

$$\lambda_B = 2n_{eff}\Lambda \qquad (2-1)$$

where Λ is the grating pitch and n_{eff} is the effective refractive index of the core. If n_{eff} or Λ changes, λ_B changes as a result.

The strain effect and the temperature effect on λ_B can be explained by partial differentiation of equation (2-1) with respect to change in periodicity and in temperature.

$$\Rightarrow \frac{\partial \lambda_B}{\partial l} = \frac{\partial (2 n_{eff} \Lambda)}{\partial l}$$
$$= 2\left(n_{eff} \frac{\partial \Lambda}{\partial l} + \Lambda \frac{\partial n_{eff}}{\partial l} \right)$$

$$\Rightarrow \frac{\partial \lambda_B}{\partial T} = \frac{\partial (2 n_{eff} \Lambda)}{\partial T}$$
$$= 2\left(n_{eff} \frac{\partial \Lambda}{\partial T} + \Lambda \frac{\partial n_{eff}}{\partial T} \right)$$

Hence the change in the Bragg wavelength due to strain and temperature changes is given by:

$$\Delta \lambda_B = \frac{\partial \lambda_B}{\partial l} \Delta l + \frac{\partial \lambda_B}{\partial T} \Delta T$$
$$= 2\left(n_{eff} \frac{\partial \Lambda}{\partial l} + \Lambda \frac{\partial n_{eff}}{\partial l} \right) \Delta l + 2\left(n_{eff} \frac{\partial \Lambda}{\partial T} + \Lambda \frac{\partial n_{eff}}{\partial T} \right) \Delta T \qquad (2-2)$$

The overall change on the center wavelength is the addition of the changes due to strain and temperature.

Strain induces change in the grating periodicity and in the refractive index of the core due to its strain dependency. Temperature also induces change in the grating periodicity and in the refractive index of the core due to its thermal dependency. Figure 2-3 depicts the changes on the center wavelength when the FBG undergoes tension. Tension shifts the FBG spectrum to the right and causes a red shift, while compression shifts the FBG spectrum to the left and causes a blue shift [5].

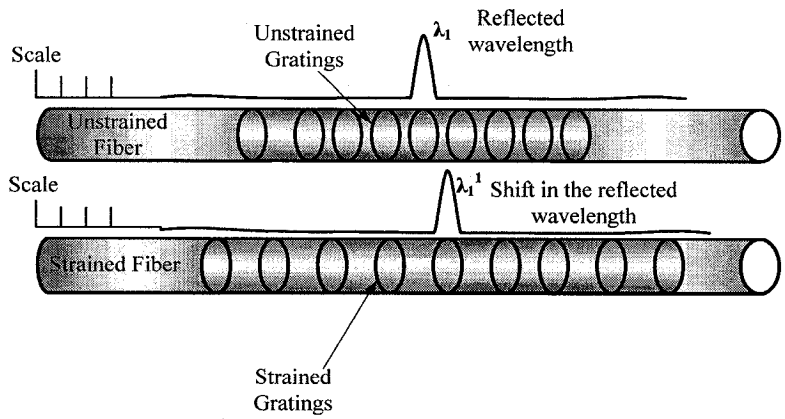

Figure 2-3 Tension effects on FBG.

2.2 FBG Properties

2.2.1 Maximum reflectivity and the full bandwidth of the reflected spectrum

The refractive index of the inscribed grating on the core of the fiber can be characterized as a uniform sinusoidal modulation along the axis of the core [3] [6].

$$n(z) = n_{core} + \delta n[1 + \cos(\frac{2\pi z}{\Lambda})] \tag{2-3}$$

where n_{core} is the un-modulated refractive index of the core and δn is the index modulation due to exposure to the UV beam.

The peak reflectivity R_{max} of the grating at the Bragg condition is defined by Eq. (2-4) [6].

$$R_{max} = \tanh^2(\kappa L) \tag{2-4}$$

where L = length of the grating, and κ = coupling coefficient.

The full bandwidth $\Delta\lambda$, of the reflected spectrum, where peak reflectivity is valid, can be defined as [6]

$$\Delta\lambda = \frac{\lambda_B^2}{\pi n_{eff} L}[(\kappa L)^2 + \pi^2]^{1/2} \tag{2-5}$$

2.2.2 Full Width at Half Maximum (FWHM)

The spectral width of light spectrum is expressed as FWHM bandwidth. FWHM is the spectral width between the points where the signal peak power has decayed to half value [7]. FWHM bandwidth is also expressed as -3dB bandwidth.

A rough calculation of FWHM bandwidth of the reflected spectrum is given by [6].

$$\Delta\lambda_{FWHM} \approx \lambda_B s[(\frac{\delta n}{2n_{core}})^2 + (\frac{\Lambda}{L})^2]^{1/2} \tag{2-6}$$

where $s \approx 1$ for gratings with high reflectivity around 100%

$s \approx 0.5$ for gratings with poor reflectivity around 5%

FBGs with low reflectivity are useful to stabilize the laser pump to operate at the center frequency of the pump.

2.2.3 Thermal properties of Fiber Bragg Grating

A FBG is sensitive to temperature variations due to inherent thermal expansion properties of the fiber and due to the thermo-optic characteristics of the refractive index profile [8]. The amount of wavelength shift in a Fiber Bragg Grating due to strain and temperature changes is given by [3] [8] [9].

$$\frac{\Delta\lambda}{\lambda_B} = \varepsilon\{1 - 0.5n_{eff}^2[P_{12} - \nu(P_{11} + P_{12})]\} + \xi\Delta T \qquad (2\text{-}7)$$

where ε = Axial strain in the optical fiber core

ΔT = Temperature change

P_{ij} = Strain-optic constant (Pockel's coefficient)

ν = Poisson's constant for the fiber

n_{eff} = Effective refractive index of the fiber that the propagation mode sees

ξ = Thermo-optic coefficient of fiber

Most of these parameters remain constant for different fibers. For standard 3M fiber Eq. (2-7) can be simplified to [9].

$$\frac{\Delta\lambda}{\lambda_B} = 0.79\varepsilon + \xi\Delta T \qquad (2\text{-}8)$$

3M has experimentally characterized the "Thermo-optic coefficient ξ", for the standard 3M fibers as $6.3\text{x}10^{-6}/°\text{C}$ [9].

Alen D. Kersey et al have shown that the effective strain-optic constant is (1 – (~0.22)) = ~0.78 [8]. This results in the following relationship for silica fiber at constant temperature [8].

$$\frac{1}{\lambda_B}\left(\frac{\delta\lambda_B}{\delta\varepsilon}\right) = 0.78\times10^{-6}\,\mu\varepsilon^{-1} \tag{2-9}$$

This results in a theoretical prediction of the strain-dependent wavelength shift being ~1 pm/uε at a wavelength of 1300 nm [8]. The wavelength strain sensitivity of a 1550nm Bragg grating is ~1.21pm/uε. In silica fiber, the thermal response is dominated by the rate of change of the refractive index with respect to temperature change and it accounts for about 95% of the observed shift in the Bragg wavelength. The normalized thermal sensitivity at constant strain is given by [8].

$$\frac{1}{\lambda_B}\left(\frac{\delta\lambda_B}{\delta T}\right) = 6.67\times10^{-6}\,{}^{o}C^{-1} \tag{2-10}$$

Temperature sensitivity is ~10 pm/°C at 1550nm.

2.2.4 Mechanical properties of the Fiber Bragg Grating

When the FBG is subjected to mechanical stress, it is transferred on to the FBG sensors as longitudinal strain or compression. The resultant longitudinal strain or compression causes a limited change in the grating pitch, leading to a change in the fiber index due to photo elastic effects [8].

Therefore, the wavelength shift, $\Delta\lambda_B$, resulting from change in force per unit area/pressure, ΔP, is given by [3].

$$\frac{\Delta\lambda_B}{\lambda_B} = \frac{\Delta(n\Lambda)}{n\Lambda} = \left(\frac{1}{\Lambda}\frac{\delta\Lambda}{\delta P} + \frac{1}{n}\frac{\delta n}{\delta P}\right)\Delta P \tag{2-11}$$

The assumption here is there is no change in the fiber diameter or cross section due to the applied pressure/change in force. Hence only the fiber experiences longitudinal strain or compression. As such for SM fiber the strain relationship and the index change can be given as [3],

$$\frac{\Delta L}{L} = -\frac{(1-2v)P}{E} \tag{2-12}$$

and

$$\frac{\Delta n}{n} = \frac{n^2 P}{2E}(1-2v)(2\rho_{12}+\rho_{11}) \tag{2-13}$$

where E = Young's Modulus of Fiber.

Since $\Delta L/L = \Delta\Lambda/\Lambda$, substituting $\Delta L/L = \Delta\Lambda/\Lambda$ in Eq.(2-12), the normalized pitch pressure can be expressed as,

$$\frac{1}{\Lambda}\frac{\delta\Lambda}{\delta P} = -\frac{(1-2v)}{E} \tag{2-14}$$

Similarly from Eq.(2-13), the normalized index-pressure coefficient can be expressed as

$$\frac{1}{n}\frac{\delta n}{\delta P} = \frac{n^2}{2E}(1-2v)(2\rho_{12}+\rho_{11}) \tag{2-15}$$

Substituting Eq. (2-14) and (2-15) into Eq. (2-11), the wavelength-pressure sensitivity will be given by [3].

$$\Delta\lambda_B = \lambda_B[-\frac{(1-2v)}{E}+\frac{n^2}{2E}(1-2v)(2\rho_{12}+\rho_{11})]\Delta P \qquad (2\text{-}16)$$

2.3 Summary

In this chapter, the FBG structure has been analyzed and FBGs are considered as filters. It has been highlighted that the period of the written FBG is half of the period of the phase mask that was used to write the grating on the fiber. Light reflection and transmission phenomena and the Bragg condition of the FBG were discussed. Equations were given for the temperature effect and the strain effect on the shift in the Bragg wavelength.

The periodic refractive index of the inscribed grating along the axis of the fiber has been described as a uniform sinusoidal modulation along the axis of the core. The relationship between the peak reflectivity to the length of the FBG has been described. In addition, the full bandwidth and the FWHM bandwidth of the reflected spectrum have been given. The thermal properties and mechanical properties of FBGs have been discussed in detail.

Chapter 3

Applications of fiber optic sensors

In this chapter, application areas of FBG and the existing technologies for interrogation methods are studied. Interrogation techniques for quasi-static strain sensing and dynamic strain sensing are described. The efficiency of parallel detection using array waveguide and photo diode array interrogation is highlighted. Temperature and strain sensing and the influence of temperature over strain sensing have been explained. Usage of TDM and CDMA for extending the number of FBGs on a network is discussed.

3.1 Introduction

FBG technology has found its way into an extensive range of applications. In the telecommunications industry, some key areas where FBGs are used include: narrowband filters for WDM add/drop requirements; stabilizing the wavelength of pump lasers; and functioning as Gain-Flattening Filters (GFFs) by having asymmetric reflectivity for different wavelengths [2].

Gratings play a vital role in stabilizing the laser emission from laser diodes. Gratings with low reflectivity are inscribed in the pig-tail of the laser diodes to stabilize the laser emission at a particular wavelength. Since the grating reflects a unique wavelength, the pump laser will force itself to operate at the center wavelength of the grating, and thus the

pump efficiency will be high. This way the FBG indirectly contributes to laser output power stability and the reduction of high-frequency noise [2].

Applications of GFF have need of chirped gratings whose period monotonically increases length-wise according to the spectrum requirements. Different wavelengths across the amplifier bandwidth are reflected with different intensity so as to flatten the EDFA gain profile. To transmit different intensity of light levels at different wavelengths, chirp gratings are written with different reflectivity at each point along the length of the grating [2]. Because the spectrum of the GFF made from a chirp grating is fixed, this GFF alone is not suitable for dynamically changing gain profiles. Adaptive GFFs are available whose gain varies dynamically depending on the feedback on the intensity level at different wavelengths of the output spectrum. The promising applications for FBGs are to use them as sensors for extensive structural safety monitoring [3] [4], widespread health-care monitoring, advanced testing of gas turbine engines, monitoring biological agents in chemicals and the like.

3.2 FBG interrogation technologies and techniques

The key to successful signal sensing is the sensor technology itself plus the interrogation technique used to detect the signal accurately. FBG interrogation is the commonly used name for detecting the signals reflected by the FBG sensors in the network. Some of the currently used more popular FBG interrogation techniques are: Tunable Laser Interrogation System, Acousto-Optic Tunable Filter (AOTF) Interrogation [7] [10], FFP-TF Scanning Interrogation [11], Mach-Zehnder Interferometer, and Micro-Opto-Electrical-Mechanical-System (MOEMS) Filter Interrogation [12], Array Waveguide

Grating (AWG) and Photo Diode (PD) Array Interrogation [13]. Except for the Array Waveguide and Photo Diode Array Interrogation method, all the above interrogation techniques are based on a scanning mechanism.

3.2.1 Quasi-static strain sensing

There are many ways to do quasi-static strain wavelength analysis. Tunable passband filters such as FFP-TF are commonly used for tracking the FBG signals [8].

Figure 3-1 shows the fundamental approach of an interrogation system using a scanning FP filter.

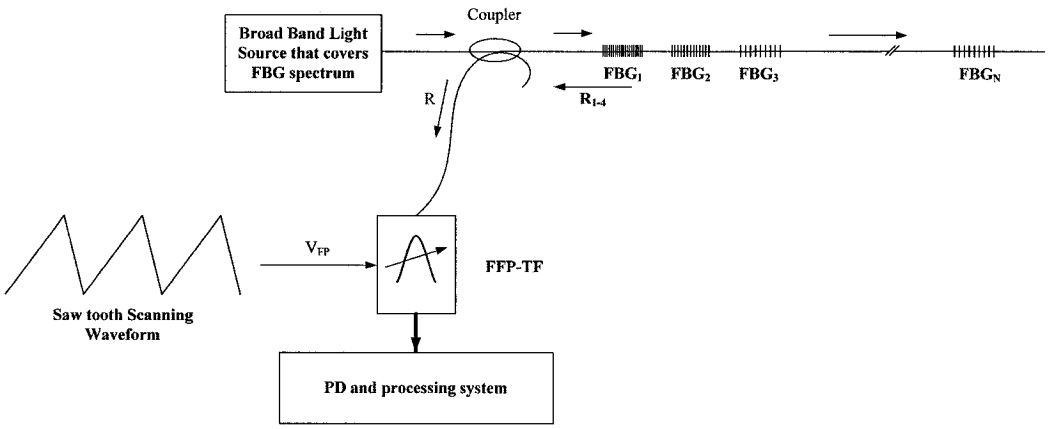

Figure 3-1 FBG interrogation system based on Scanning FFP-TF detection method [8].

The resonant pass band wavelength is controlled by electrically tuning the distance between the piezoelectric elements. The wavelengths of the detected signals can be calculated from the voltage applied to the piezoelectric elements of the FFP-TF [8]. Though FFP-TF exhibits a slight non-linear behavior, by doing a continuous calibration

or using a look-up table with pre-recorded "FFP-TF tuning voltage (or corresponding ADC counts) vs. pass-band wavelength" for the direction of the tuning voltage, the accuracy of the detected wavelengths can be greatly improved. Since the number of FBGs per fiber is mainly limited by the scanning bandwidth of the filter, an optical switch would help to expand number of FBGs by connecting the number of fiber channels of FBG arrays to the different ports of the optical switch and scanning one channel at a time. Although many FBGs can be scanned using an optical switch, the drawback is that this is achieved at the expense of speed and thus loss of some real-time spectral information. Figure 3-2 shows an example of optical switch implementation [8].

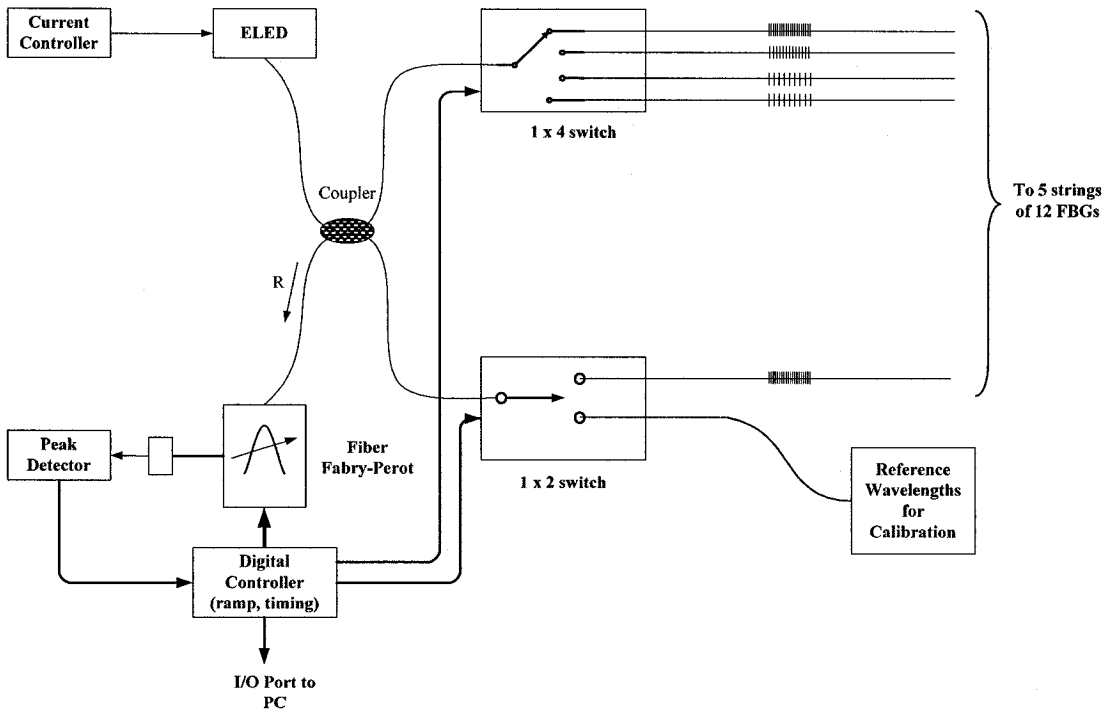

Figure 3-2 Multi-channel quasi–static strain monitoring system [8].

A drawback of scanning detection is that the reflectivity of the FBGs should be stronger. FBGs with strong reflectivity of around 95% are good to be used in a DFBG network. In

addition, a brighter light source is required for the detected signal to be measurable. CCD (Charged Coupled Devices) and array waveguides eliminate this limitation [8].

3.2.2 Usage of TDM and WDM

With WDM technology, reflected wavelengths of many FBGs embedded in a single fiber can be detected as long as the spectrum of the input light source and bandwidth of the interrogation system covers the wavelength of all FBGs [8]. By merging other multiplexing techniques such as TDM, CDMA, and the like, the number of detectable FBGs can be expanded.

3.2.3 Real-time strain monitoring

Interferometric techniques are widely accepted for dynamic strain sensing. Figure 3-3 illustrates a Mach-Zehnder interferometer setup which is to detect the reflected spectrum from a FBG sensor. The relationship between the input and output of an unbalanced Mach-Zehnder interferometer can be expressed in the form $\{1 + \cos\phi\}$. This equation can be expanded to $\{1+ k\cos(\Phi(\lambda_B) + \varphi)\}$ to highlight the wavelength dependency of the output, where k is the interference fringe visibility, $\Phi(\lambda_B) = \frac{2\pi nd}{\lambda_B}$, n is the effective refractive index of the core, d is the physical length difference between the fiber arms, λ_B is the Bragg wavelength of the light reflected and φ is the phase offset of MZI [3]. The input is transformed in terms of phase. Hence changes in the Bragg wavelengths are expressed in terms of phase change. By varying the optical path difference between the

two arms, the interferometer output can be changed. The relationship between output phase change $\Delta\Phi(\lambda_B)$, Bragg grating wavelength shift $\Delta\lambda_B$ and optical path difference (OPD) *nd* is given by [8].

$$\Delta\Phi(\lambda_B) = \frac{2\pi nd}{\lambda_B^2}\Delta\lambda_B \tag{3-1}$$

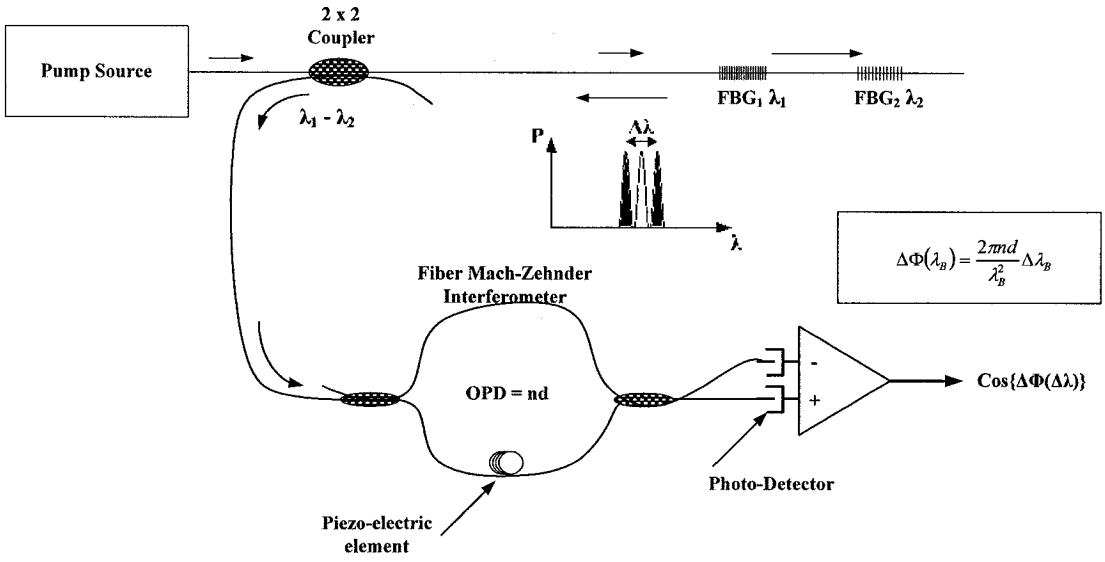

Figure 3-3 Interferometer detection for FBG sensor system [8].

3.2.4 Temperature and strain sensing

Since FBGs are sensitive to both strain and temperature changes, unless the individual effects caused by strain and temperature are separately quantifiable, the measurement of the total wavelength shift would be meaningless in many instances. E.g. measurements of the earth's movement. In this example, if the temperature effects are not segregated from

the total wavelength shift, measurements will lead to erroneous interpretations. One solution is to use different Bragg sensors with different sensitivities to measure the temperature and strain and solve the parameters from the two equations for the total wavelength shifts. Alternatively a fiber-reinforced carbon composite with neutral layer embedded grating can be used to measure the wavelength shifts due to temperature changes only. Neutral layer is the center layer of a carbon composite which is insensitive to any strain or pressure effects. In order to derive the wavelength shifts caused due to pressure, the wavelength shifts caused by the sensor embedded in the neutral layer is to be subtracted from the wavelength shifts caused by the sensor embedded in the non-neutral layer. However, there are ways by which different sensor types such as long period gratings together with FBGs can be used to measure temperature and strain changes simultaneously [8].

3.2.5 Array Waveguide Grating (AWG) and Photo Diode (PD) array interrogation

Simultaneous FBG interrogation techniques are the fastest and safest way of detecting the reflected signals from a DFBG network to minimize real-time signal loss. Figure 3-4 shows a simultaneous FBG interrogation technique using an AWG and a PD array.

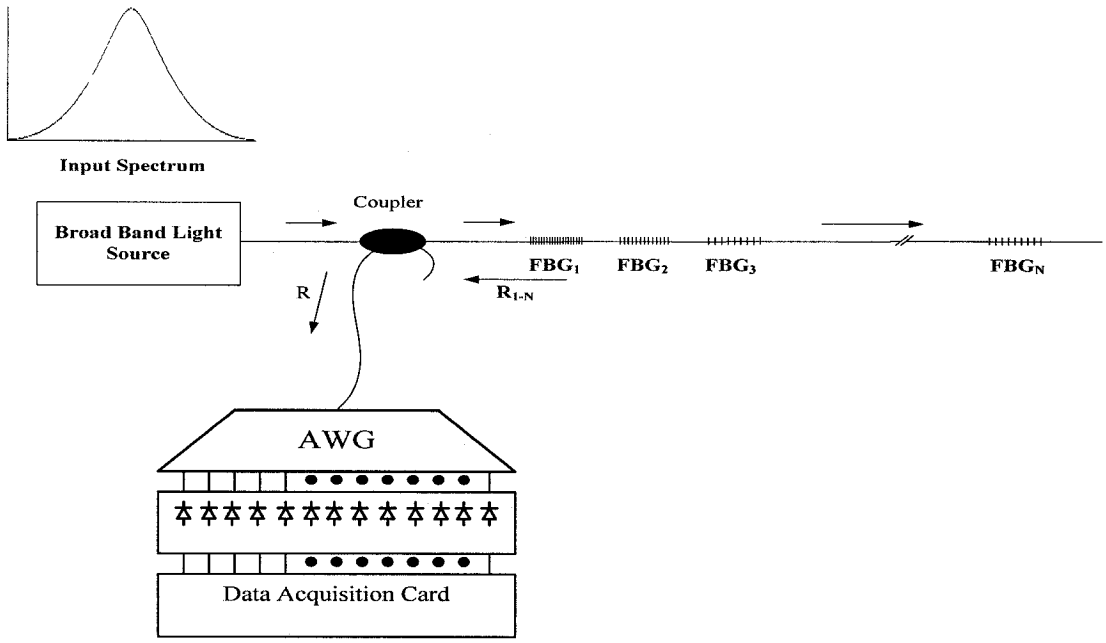

Figure 3-4 FBG Spectrum interrogation by AWG and PD array [13].

The simultaneous FBG interrogation technique by AWG and the PD array consists of two separate functions: 1) First wavelength de-multiplexing of the reflected FBG spectrum by the AWG grating which actually utilizes the WDM technology; and 2) High resolution monitoring of the FBG arrays reflected spectrum by the linear PD array [14] [15]. FBG interrogation by AWG grating and PD array actually realizes the dream of real time monitoring. Information from all the wavelengths is detected by the PD array in parallel and, in addition, this information can be processed simultaneously [13]. Interrogation by optical narrowband scanning filters has the drawback of loss of real time signal information. When using a pass-band filter scanning technique, only a narrow slice (chip) of information is sampled every time. The information outside of this chip, both in time domain and space domain, is lost [8]. However, by sticking to Nyquist sampling rate the signals can be re-constructed.

3.3 Summary

In this chapter, various applications of FBGs were studied to obtain a general understanding of the FBG application and to provide relevance to our FBG interrogation system design. The use of FBGs as narrowband filters for WDM add/drop requirements, GFF, and to stabilizing laser diodes has been discussed.

In addition to FBG sensor technology, various interrogation techniques used to detect the signal have been presented. The fundamental approach of an interrogation system using a scanning FP filter has been studied and the simplicity of this method, drawbacks, and ways of overcoming the drawbacks of the scanning FP filter were briefly looked at. Possible ways of expanding the number of detectable FBGs by implementing an optical switch, TDM, CDMA methodologies were briefly considered. Mach-Zehnder interferometric technique was quickly glanced at for dynamic strain sensing. The undesirable effect of temperature sensitivity and the method to overcome or eliminate this undesirable effect of temperature sensitivity of FBG when FBG is used for strain sensing have been discussed. The importance of simultaneous FBG interrogation techniques by AWG and the PD array has been highlighted.

Chapter 4

FBG Embedding

In this chapter the necessity of increasing the strength of the fiber and embedding techniques are studied and the embedded FBGs are characterized in different strain and temperature environments. Apodization techniques are used during FBG writing. This is as a result of multiple peak power intensity values corresponding to multiple wavelengths, instead of a single peak power intensity value corresponding to the Bragg wavelength, which is observed in the reflected spectrum of the FBG. The reflected center wavelengths or the wavelength shifts are plotted against the applied strain and temperature to characterize the behavior of FBGs under different stress conditions.

4.1 Introduction

Direct strain sensing using a bare fiber or fiber with a cladding is not feasible due to its limited range of sensing, characterized by the fragile nature of the fiber to a larger force. It is not possible to apply a large perpendicular force on bare fibers as they become permanently deformed at a very early stage and eventually break. Permanent deformation of a fiber grating, coated with 10 μm thick polyamide over a 125 μm cladding (outer diameter 145 μm), can take place when the perpendicular applied force reaches about 10 N. When the force applied on the bare fiber is approximately around 18 N, the fiber can crack [16].

In line with previous experiments, fiber-reinforced carbon composite material (**Fiberdux: 913C-XAS**) [18] [17] is selected to embed the fiber, since it should be able to withstand a larger perpendicular force. Fiberdux 913C-XAS carbon composite consists of epoxy resin pre-impregnated into unidirectional carbon fibers and thus provides the highest tensile strength. The applied perpendicular force on the composite will produce a longitudinal strain on the composite. The maximum withstanding load of the fiber-reinforced carbon composite is around 60N, and depends on the number of layers and the dimension of the laminate. This result is in line with the work carried out by Hao et al [16].

The embedding material should be chosen such that its properties of sensitivity, linear sensing range and thermal expansion coefficient of the embedded sensor are within the required specification and effectively increase the sensitivity range of the bare FBG [16] [17]. Firstly, the amount of wavelength shift per unit of applied perpendicular force will decide the sensitivity of the sensor. Second, the composite sensors operating region should cover the elastic limits of the grating. Since Carbon fiber materials preserve their elasticity till total deformation, this should guarantee the linear and reproducible operation of the sensor. Third, the thermal expansion coefficient of an optical fiber-reinforced carbon composite in the longitudinal direction is $\sim 0.73 \times 10^{-6}$ /°C, that of a bare FBG is $\sim 6.3 \times 10^{-6}$/°C [9]. Hence, we can conclude that carbon fiber restricts change in the grating period of the FBG as the temperature changes i.e. the influence of the grating period change due to thermal sensitivity is now reduced.

4.2 Embedding

During the making of fiber-reinforced carbon composites, the Fiberdux 913C-XAS laminates are first taken out of the freezer to soften and then cut into the desired shapes. The laminates are then placed ply-by-ply on an aluminum plate. Tiny air-bubbles trapped between the plates are removed using a roller to even out the surface of the plies. Figure 4-1 shows the buried fiber with gratings between the laminates.

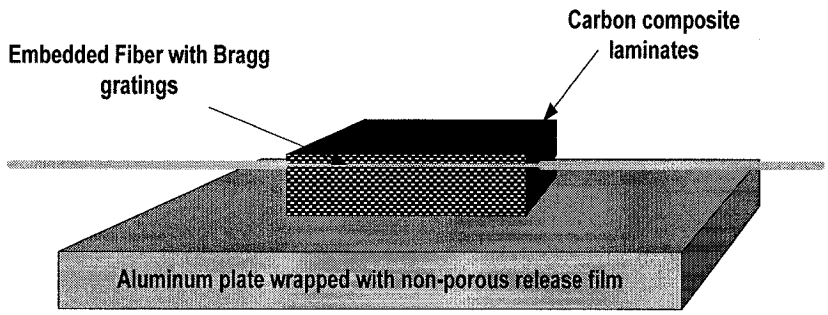

Figure 4-1 Carbon fiber reinforced laminates on an aluminum plate.

The aluminum plate has been used as a bottom support for this layout. This aluminum plate is wrapped with a layer of non-porous release film before laying the carbon laminates. Since dust particles weaken the cured laminates, the base aluminum plate is wrapped with non-porous release film and cleaned with acetone.

During the curing process the embedded fiber with the laminates are heated inside an oven at **100 °C - 120 °C** for **80 minutes**. During this process, the carbon fibers react chemically with the nearby fibers to produce a rigid cross-linked structure. The hardened

carbon composite enables the embedded FBG sensor to withstand a greater amount of pressure without breaking. Embedding the FBG in effect increases the linear sensing range of the sensor. These steps are in line with the work conducted by Hao et al [16] [19].

4.3 Orientation of the fiber during embedding

Prior experiments [16] [19] have proven that orientation of the fiber inside the laminate influences the sensitivity and the overall performance such as stiffness of the FBG sensor to a great extent. Because of the characteristics of the composites, the fiber-reinforced laminates achieve a very high tensile modulus along their axis. However, they have a low tensile modulus perpendicular to their axis. Thus the orientation of the fiber within the carbon composite decides the sensitivity and strength of the composite sensor. In Figure 4-2 (a), the grating fiber is in parallel with the axis of the carbon laminar. This structure is named as **0° uni-ply** laminated FBG sensor. As per earlier experiment results [19] from the Scanning Electron Microscopy (SEM), shown in Figure 4-3 (a) it can be seen that the grating fiber is nicely embedded within the plies.

In Figure 4-2 (b) the grating fiber is embedded perpendicular to the axis of the carbon laminar. This composite is commonly named as **90° uni-ply (cross-ply)** laminated FBG sensor. From Figure 4-3 (b), we can see that **90° uni-ply** laminated FBG sensor is completely fractured. The fiber is deformed and the acrylate coating is compressed and elongated voids have been formed.

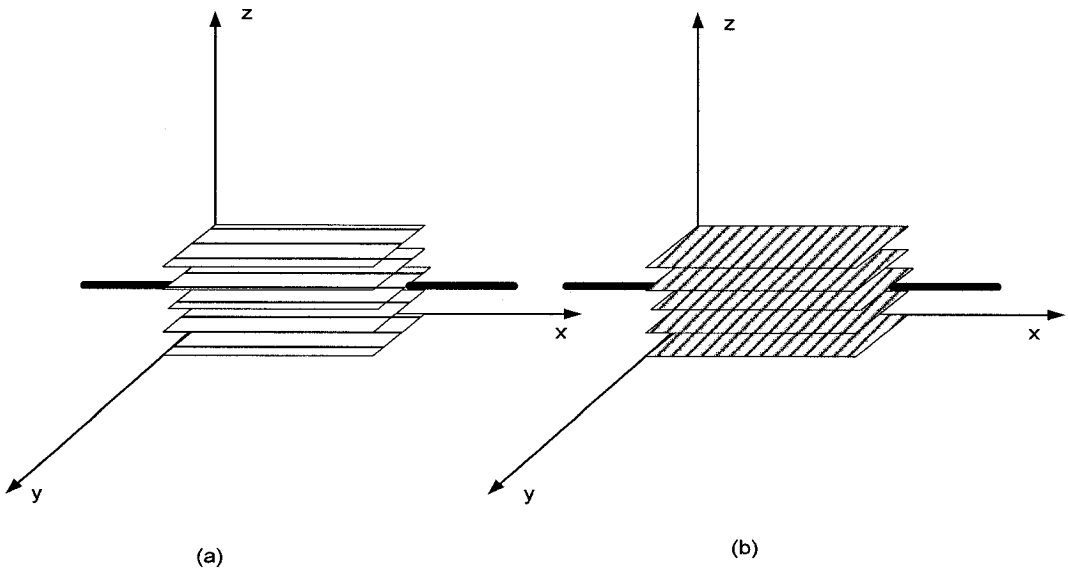

Figure 4-2 (a) Grating fiber is aligned in parallel to the axis of the laminate (0° uni-ply). (b) Grating fiber is aligned in perpendicular to the axis of the laminate (90° uni-ply) [20].

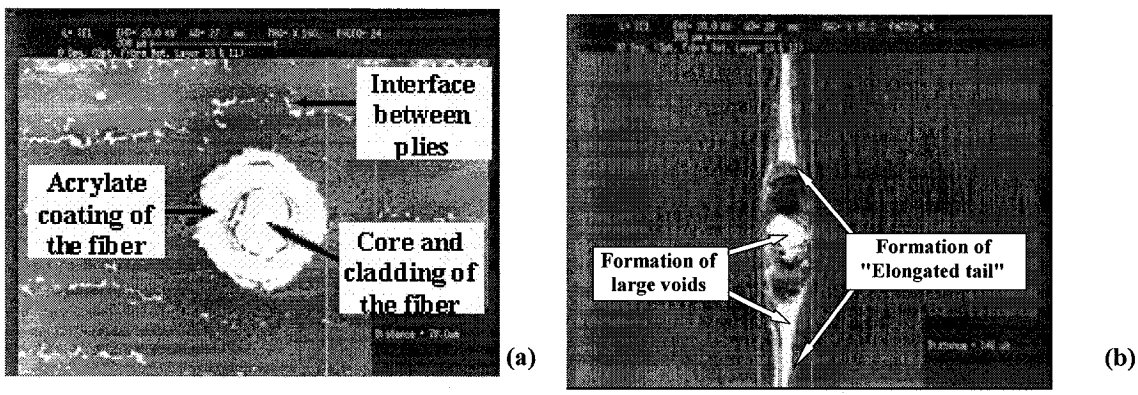

Figure 4-3 (a) SEM showing acrylate-coated fiber embedded at 0° to the axis of the laminates. (b) SEM showing acrylate-coated fiber embedded at 90° to the axis of the laminates. These pictures are taken from [19].

In line with these reasons, all the way through our research work, the grating fibers are embedded in parallel to the carbon laminates. However, prior studies [16] show that higher sensitivity can be achieved with cross-ply laminates provided orientation of the adjacent laminates to the grating fiber are **0° uni-ply.** The **0° uni-ply** orientation of the grating fiber as shown in Figure 4-3 (a) would result in a reflected spectrum with a single peak power density value corresponding to the Bragg wavelength. The **90° uni-ply** orientation of the grating fiber as shown in Figure 4-3 (b), would result in a reflected spectrum with multiple peak power density values corresponding to multiple wavelengths in addition to one for the Bragg wavelength [19]. By keeping the adjacent fibers of the cross-ply orientation to be **0° uni-ply,** multiple peaks that would result otherwise from a complete cross-ply orientation can be avoided.

4.4 Characterization of embedded sensors

Temperature change and strain variations can be monitored by using the property of the linear relationship of the composite sensor between the Bragg wavelength shift and the axial strain. An elongation would result in grating period increase and thus a red shift in the Bragg wavelength spectrum. Compression would result in grating period decrease and thus a blue shift in the Bragg wavelength spectrum.

4.4.1 Bending concepts

In general, materials undergo tension and compression at the same time. When a structure is subjected to bending, it forms an arc. On the inner part of the arc, the structure undergoes compression and the outside structure is stretched and it undergoes elongation [21]. This phenomenon is shown in Figure 4-4.

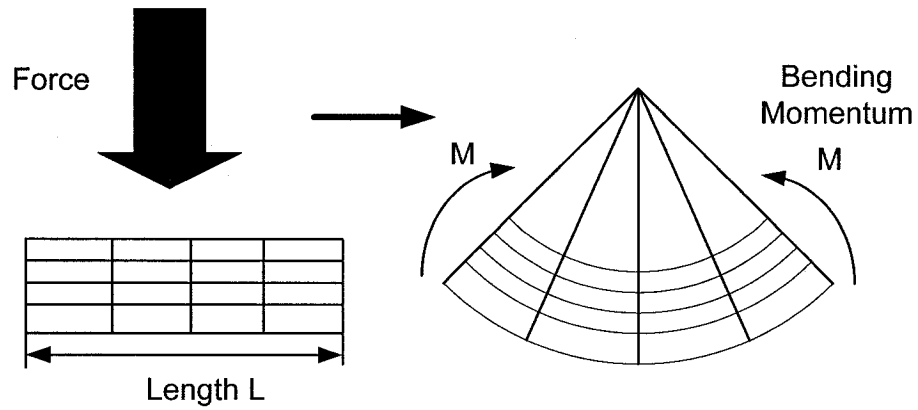

Figure 4-4 Bending phenomenon of a structure to a downward force [21].

During the bending, if we observe the behavior of the axial and transverse lines, the transverse lines will remain straight and will become radial lines. On the other hand the axial lines will bend to form circumferential lines. However, the central or axial line will not expand nor contract. The surface associated with the unstressed axial line is called neutral layer. As illustrated in Figure 4-5, one side of the structure to the neutral layer undergoes compression and the other, elongation (tension).

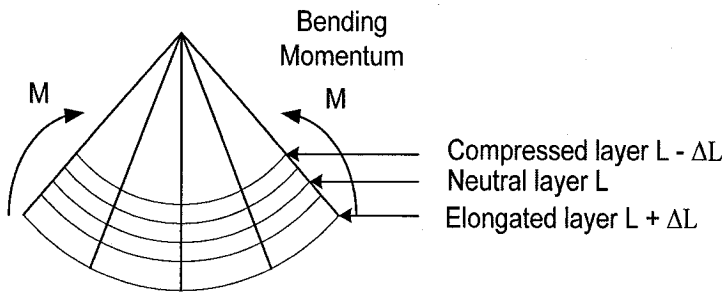

Figure 4-5 The neutral, elongated and compressed layers during bending [21].

4.4.2 Neutral layer embedding

In the (0/0/FBG1/0/0) fiber composite configuration, '0' indicates carbon lamina orientation is **0° uni-ply.** In Figure 4-6 (a), four of the carbon laminas, and in Figure 4-6 (b), six of the carbon laminas are in **0° uni-ply** orientation.

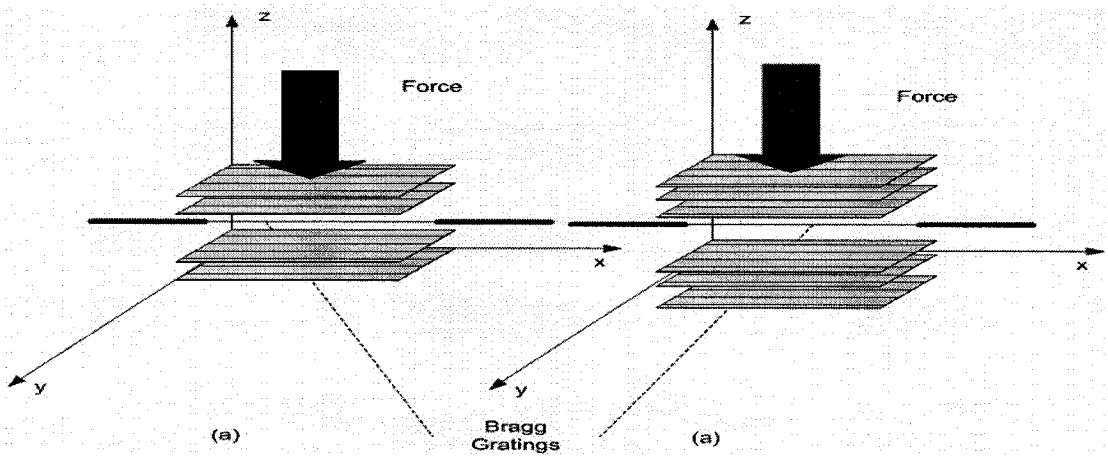

Figure 4-6 Fiber embedding in (a) 4-ply composites (0/0/FBG1/0/0) and (b) 6-ply composites (0/0/0/FBG2/0/0/0) configurations [20].

When the fiber is embedded in the neutral layer, the grating will not experience any compression or tension, hence the grating pitch will not change and there will not be any shift seen in the reflected center wavelength [16]. Using a "Digital Force Gauge", different force levels applied on 4-ply and 6-ply configurations are measured and the results are plotted as shown in Figure 4-7.

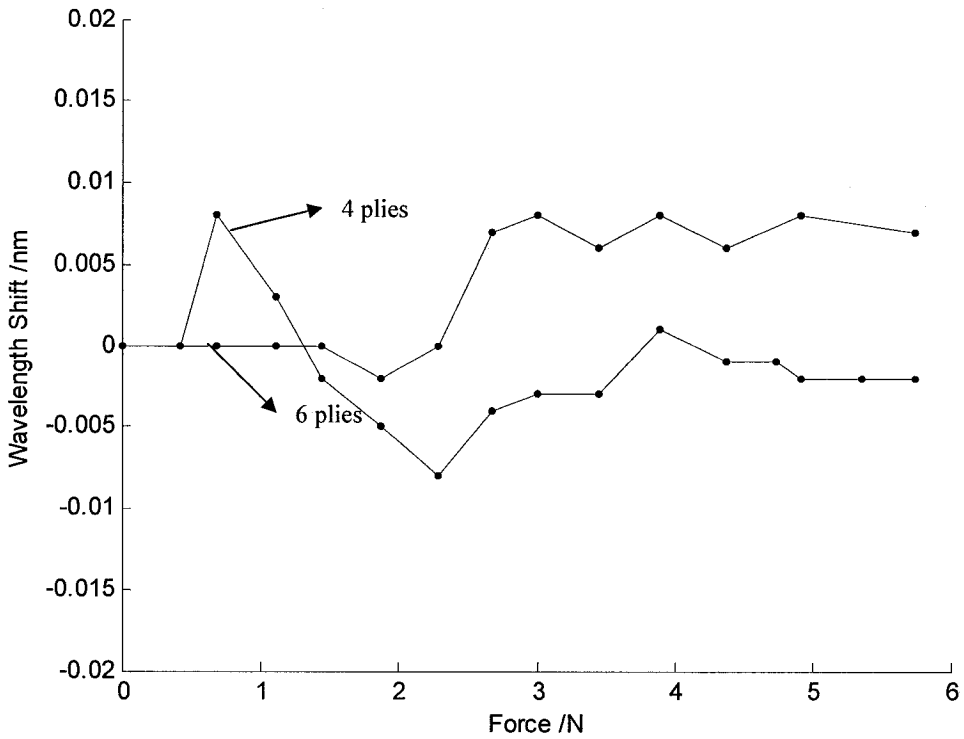

Figure 4-7 Wavelength responses when the grating fiber is embedded in the 0/0/FBG1/0/0 (Center wavelength 1543.728nm; FBG length = 10mm) and 0/0/0/FBG2/0/0/0 (Center wavelength 1549.051nm; FBG length = 10mm) configurations. Module length 50mm, width 5 mm. Imprinting Technique = Phase Mask [20].

From the results and the graph it can be seen that the variation on the reflected center wavelength is insignificant. This small variation can be associated with environmental perturbations and the non-uniformity in the thickness of the carbon lamina, etc.

4.4.3 Non-neutral layer embedding

The fiber-reinforced carbon composite configuration (0/FBG3/0/0/FBG4/0) shown in Figure 4-8 shows FBG3 is embedded above the neutral layer and FBG4 is embedded below the neutral layer.

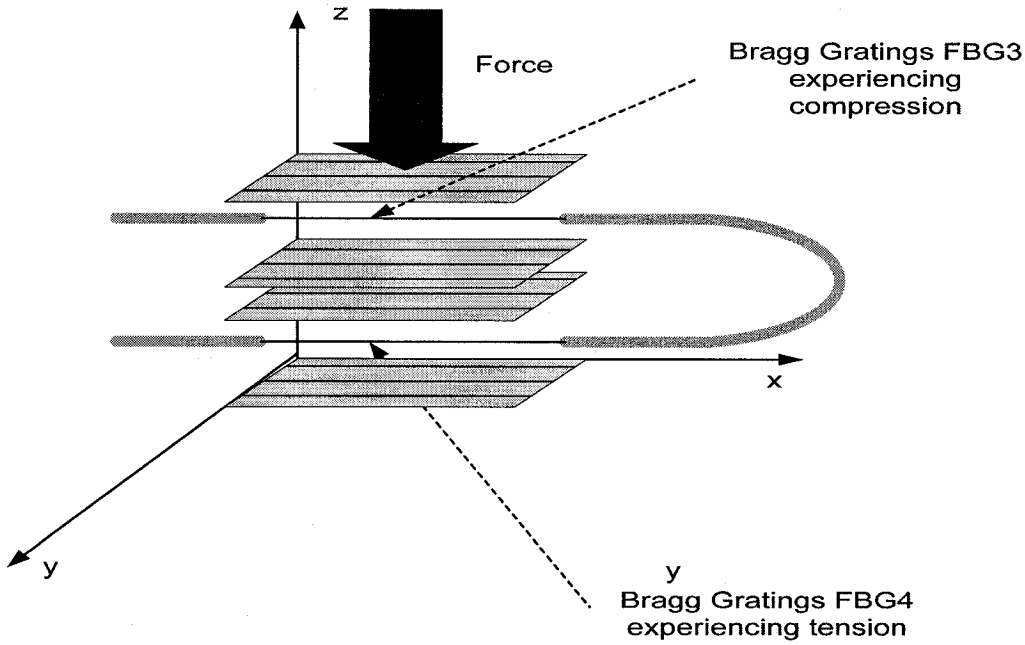

Figure 4-8 Hybrid module with 2 FBGs. The one above the neutral layer experiences compression and the one below the neutral layer experiences tension for the same downward force [20].

Hence, FBG3 will experience compression and produce a blue wavelength shift and FBG4 will experience tension and will produce a red wavelength shift. The center wavelengths of FBG3 and FBG4 are 1530.788 nm and 1531.168 nm, respectively.

Though FBG3 and FBG4 are inscribed using the same phase mask, some tension is applied to FBG3 and the fiber is held under tension during the inscription process such that there is wavelength shift when the fiber is relaxed. The shorter wavelength FBG3 is intentionally placed above the neutral layer and the longer wavelength FBG4 is placed below the neutral layer. This configuration avoids wavelength overlapping.

When the composite is subjected to a downward force, the shorter wavelength becomes even shorter, the longer wavelength becomes even longer and the difference between two reflected wavelengths will continue to increase with the increase in the applied force.

From the graph shown in Figure 4-9, it can be seen that there is a linear relationship between the applied force and the shift in the wavelengths. As the correlation coefficients are very close to unity, we can have a high level of confidence in the reliability of the linear relationship. The square of the correlation coefficient (R^2) for FBG3 configuration is 0.9975 and that for FBG4 configuration is 0.9998. The correlation coefficient shows the strength and direction of a linear relationship between two random variables and when it is closer to 1, the linear relationship is stronger.

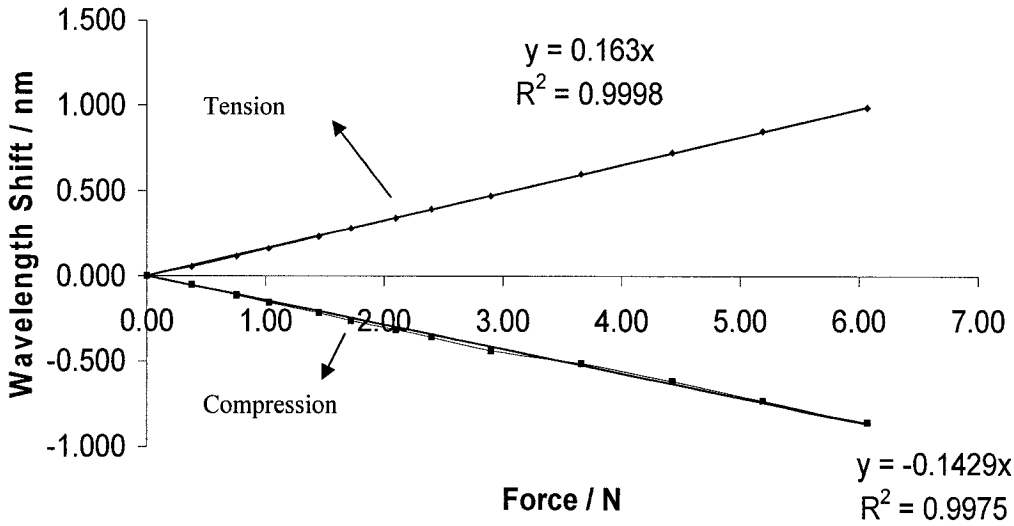

Figure 4-9 Wavelength shift vs. applied downward force when the FBG is embedded in 0/FBG3/0/0/FBG4/0 configuration [20]. Center wavelengths FBG3 configuration = 1530.788nm; FBG4 configuration = 1531.168nm. Lgrating = 10mm; Lmodule = 50mm; Mask period =1508.04 nm. Imprinting Technique = Phase Mask.

From the results shown in Figure 4-10, it can be seen that FBGs in different configurations show different sensitivities to the applied force. Sensitivity can be found from the gradient of the "Wavelength shift vs. Force graph". The negative gradient corresponds to compression and the positive gradient corresponds to tension. In addition, it can be observed that the further the distance from the neutral layer, the higher the sensitivity. The results show that our test results are in line with tests conducted by Hao et al [16].

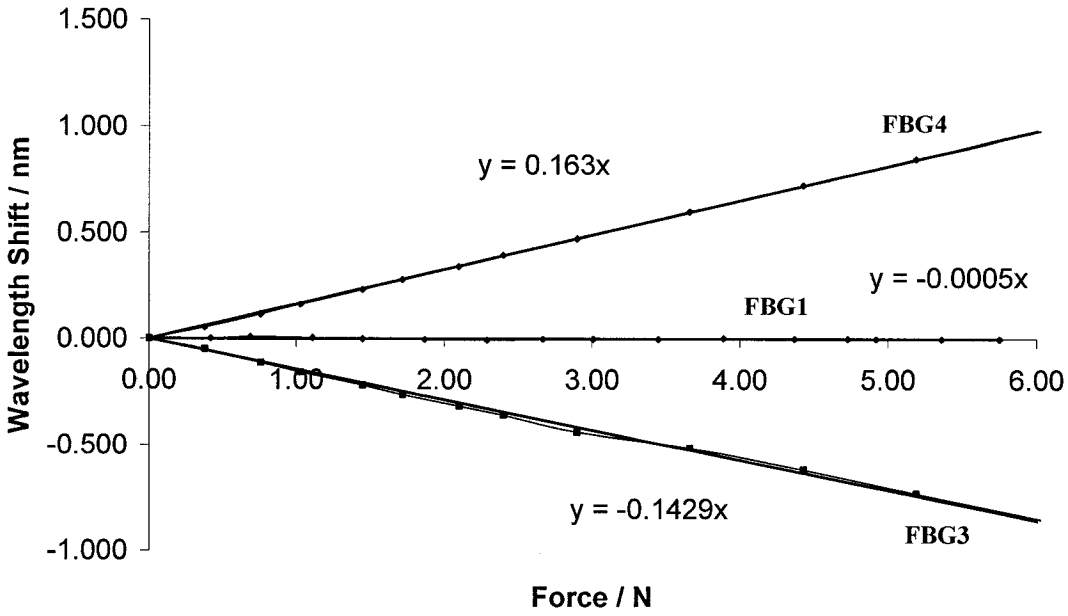

Figure 4-10 Comparisons between wavelength shifts when the FBGs are embedded in 2 different configurations: 0/FBG3/0/0/FBG4/0 and 0/0/FBG1/0/0 [20]. Lg = 10 mm; Module length = 50mm; FBG1 =1543.728, Mask period = 1066.79nm; FBG4=1531.168nm, Mask period = 1508.04nm; FBG3=1530.788, Mask period = 1508.04nm. Imprinting Technique = Phase Mask.

4.4.4 Sensor embedded in arc shape

An arc shape increases the sensitivity to single-point bending force. In case of flat composites, a 3-point bending force is required to subject the composite to a deformation. Figure 4-11 shows that fiber-reinforced carbon composites are formed in an arc shape. This has been possible as the carbon laminates were soft before the curing process.

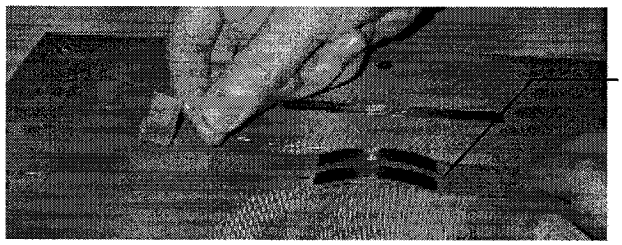

(a)

(b)

Figure 4-11 (a) Shows an FBG sensor embedded in an arc shape with the support of an arc-shaped metal bridge. (b) Shows the arc-shaped and the flat sensors after the curing process [20].

As shown in Figure. 4-12 (a), FBG5 and FBG6 are embedded in the 0/FBG5/0/0/0 and 0/0/0/FBG6/0/0/0 configurations, respectively, in an arc shape in a single fiber-reinforced composite.

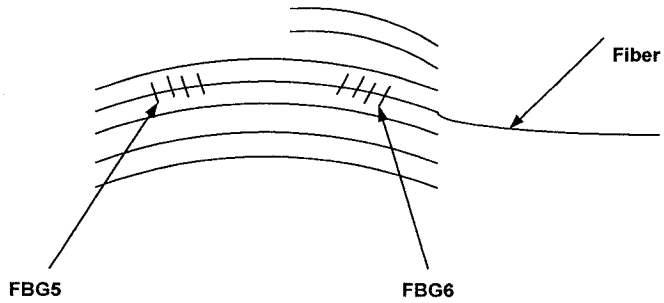

(a)

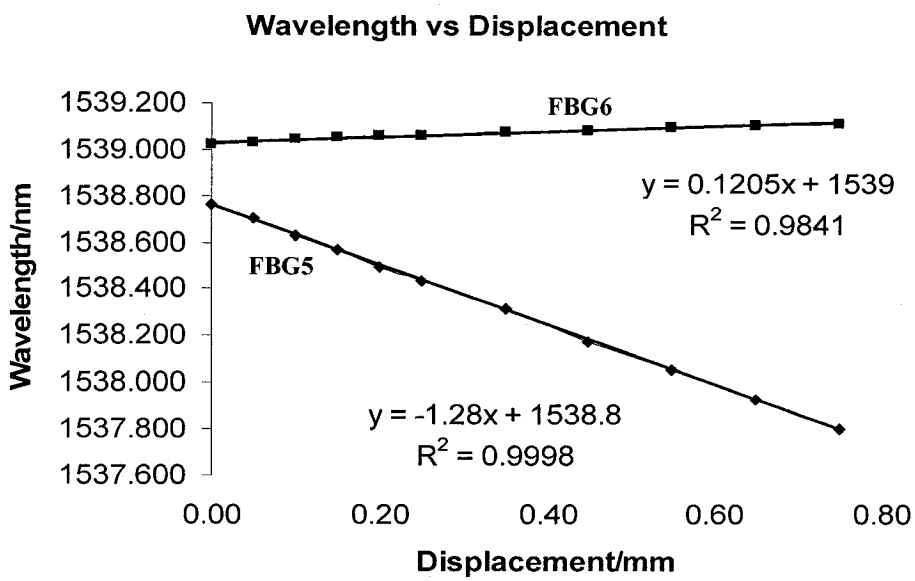

(b)

Figure 4-12 (a) Shows an arc-shaped hybrid carbon composite module with FBG5 is in 0/FBG5/0/0/0 configuration while FBG6 is in 0/0/0/FBG6/0/0/0 configuration. (b) Shows a plot for wavelength against Displacement. Lg = 10 mm; Module length = 50mm; FBG5 = 1538.763nm; FBG6= 1539.02nm; Imprinting Technique = Phase Mask [20].

The results showed that FBG5 has a sensitivity of **-1.28 nm/mm** and FBG6 has a low sensitivity of 0.1205**nm/mm**. The square of the correlation coefficient (R^2) between the wavelength and displacement are 0.9998 and 0.9841, respectively for FBG5 and FBG6.

4.4.5 Peak splitting

During the initial tests, the phenomenon of many peaks appearing has been observed in the reflected spectrum, when a force is applied. Figure 4-13 shows the reflected spectrum from a hybrid module made up of 2 FBGs inscribed in series, when no force is applied, and Figure 4-14 shows the reflected spectrum with many peaks, when a force is applied on the same hybrid module.

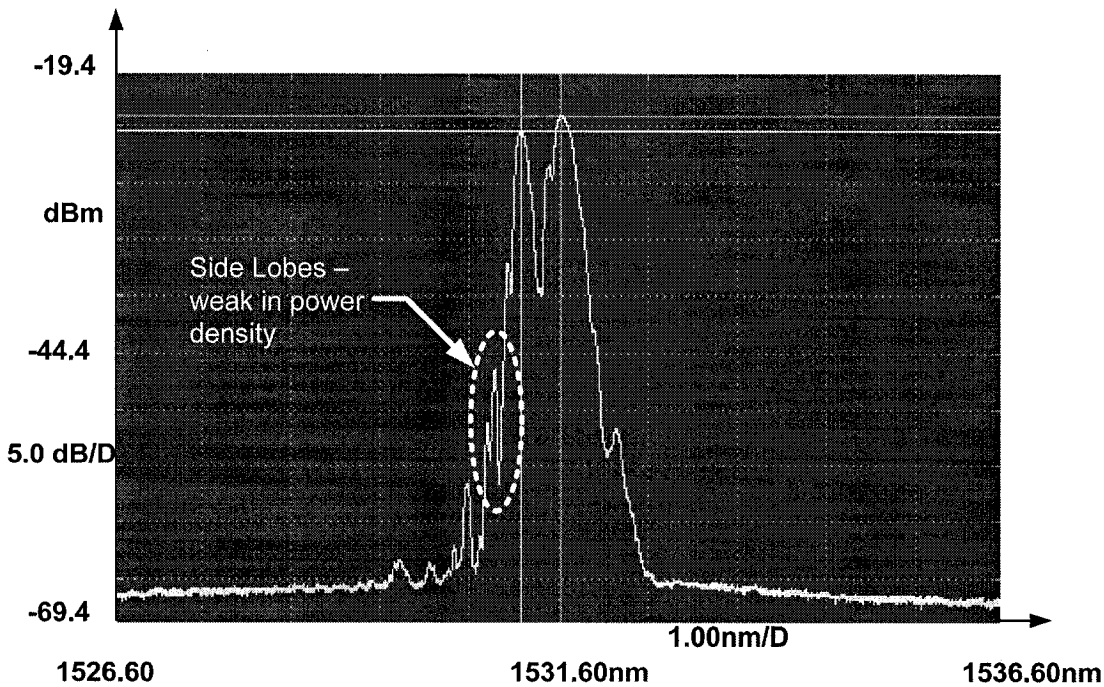

λ1 = 1531.631 nm;λ2 = 1531.175 nm Δλ = 0.456nm
L1=-23.50dBm;L2=-24.70dBm

Figure 4-13 Reflected spectrums when the FBG hybrid module is not subjected to any force. Side lobes are weak in power density [20].

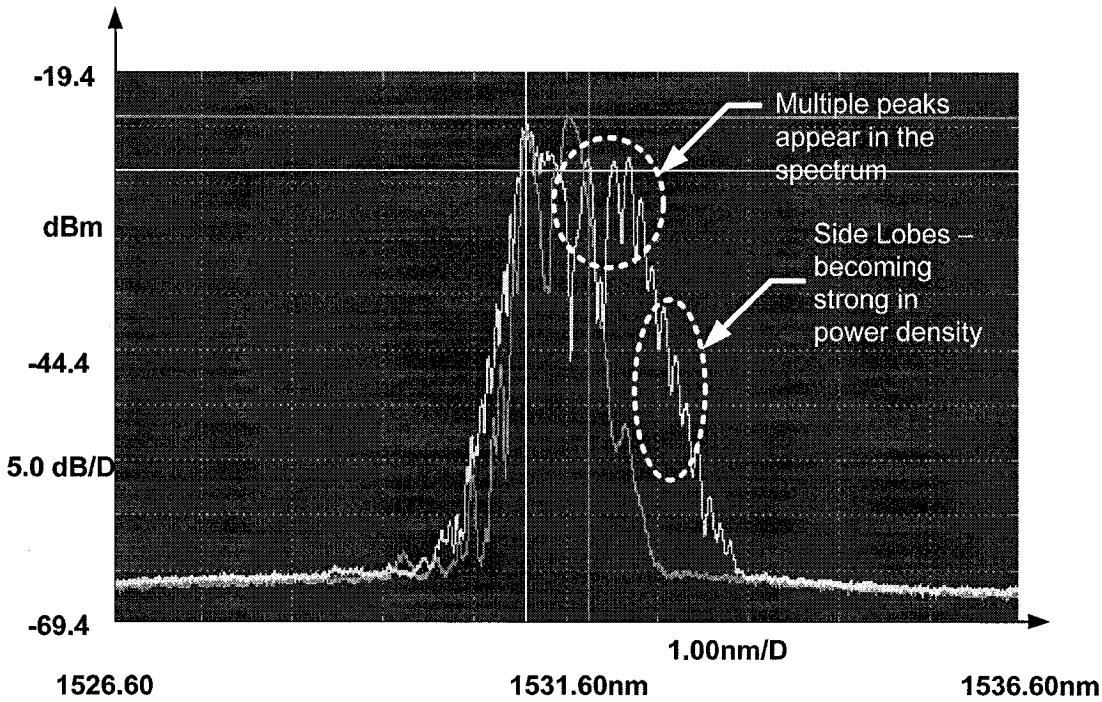

$\lambda 1 = 1531.858$ nm; $\lambda 2 = 1531.156$ nm $\Delta\lambda = 0.456$nm
L1=-23.50dBm;L2=-28.30dBm

Figure 4-14 Reflected spectrums when a downward force is applied on the FBG hybrid module. Multiple peaks appear and the side lobes are strong. The center curve is the same curve as in Figure 4-13 [20].

This widespread problem, which manifested itself during the course of the experiments when a force was applied on the embedded FBG, is known as **peak splitting**. Though the same phase mask is used to inscribe these 2 FBGs, to make them to have different wavelength at rest, they are subjected to different longitudinal tensions during FBG inscription. Hence, their Bragg wavelengths are 1531.175nm and 1531.631nm. As shown

in Figure 4-14 (curve shifted to the right), when the FBG composite is subjected to a perpendicular force, a peak splitting phenomenon is observed in the reflected spectrum.

Existence of the side lobes cause the peak splitting when the force is applied. In general, the power density of the side lobes is small. However, they increase with an increase in the applied force [3] [22]. In line with this concept, it has been proved from Figure 4-14 (curve shifted to the right), that the side lobes become more "prominent" with the increase in applied force.

In another experiment carried out with FBGs of center wavelengths of 1548.94nm, the peak splitting is not apparent when subjected to smaller force/displacement though it becomes apparent when subjected to increased force/displacement as shown in Figure 4-15 (a) and (b).

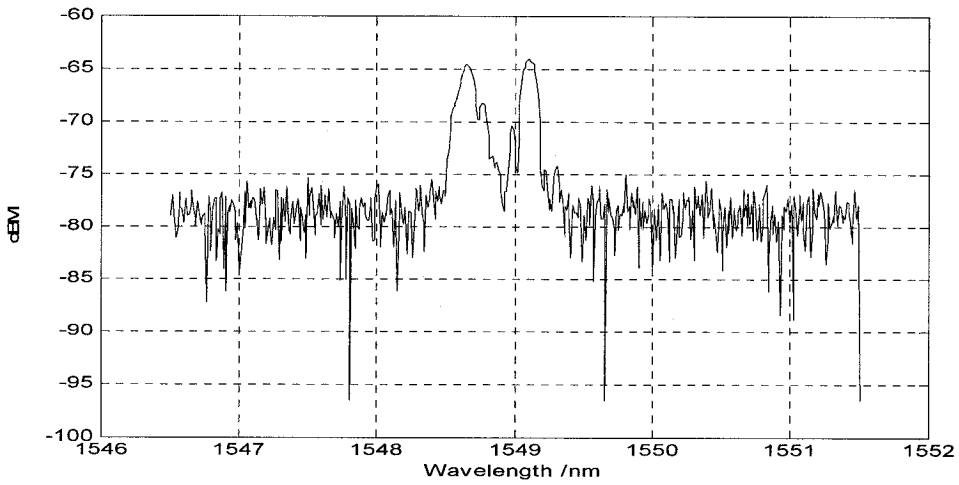

(a)

λ1 = 1548.660nm; λ2 = 1549.110nm; L1=-64dBm

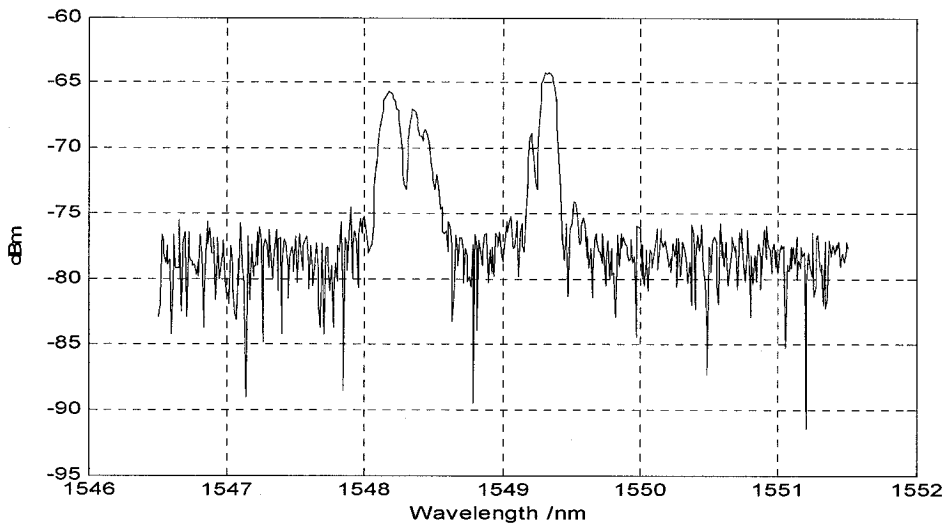

(b)

λ1 = 1548.180 nm;λ2 = 1549.330 nm; L1=-64dBm

Figure 4-15 (a) When smaller force/displacement is applied on the hybrid FBG module (b) When larger force/displacement is applied on the hybrid FBG module.

The key reason for side lobes to occur is because the index profile of the grating is rectangular. The index profile of the grating begins abruptly and ends abruptly. When we inscribe the gratings, the intensity of the 244nm UV Argon ion laser beam used to write the grating is of constant power density 500 mW. The constant power intensity of the UV laser ends up on even modulation of the fiber producing abrupt index change. The Fourier Transform of this 'rectangular' function will produce a *"sinc"* function, giving the side lobes structure. To solve the problem of peak splitting, we make use of an **apodization technique** (with Cosine, Hamming window, Blackman and the like to control the power density pattern of the UV laser beam) to create a gradually varying index profile and thus suppress the side lobes in the reflection spectrum [3] [22].

Figure 4-16 shows the reflection spectrum (center curve) of the apodized grating when no force is applied. We can see that the side lobes are very much reduced and the reflection spectrum is smooth. When the grating is subjected to perpendicular force, it is noted that no splitting of wavelength occurred on the reflected spectrum (curve with larger wavelength gap between the peaks). Hence, this proves that apodization of the grating while writing on the fiber not only reduces peak splitting but also produces a smooth reflection spectrum.

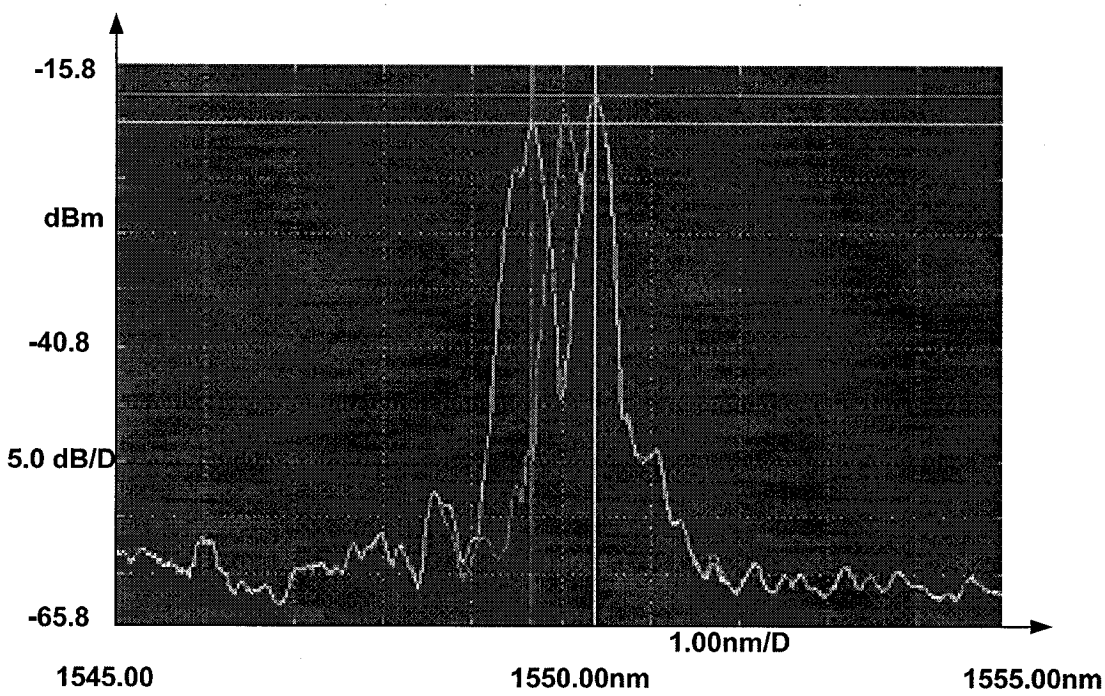

λ1 = 1550.37 nm;L1=-18.74dBm;

Figure 4-16 Side lobes are significantly suppressed by using an apodization technique during the writing of the FBGs [20].

4.4.6 Temperature effects

An FBG sensor with configuration 0/0/FBG/0 is heated from 31.8 °C to 68.7 °C in an oven. Since the "Digital force gauge" is not able to fit in the oven, a micro-screw meter is used and the wavelength shifts are measured against displacement as shown in Figure 4-17.

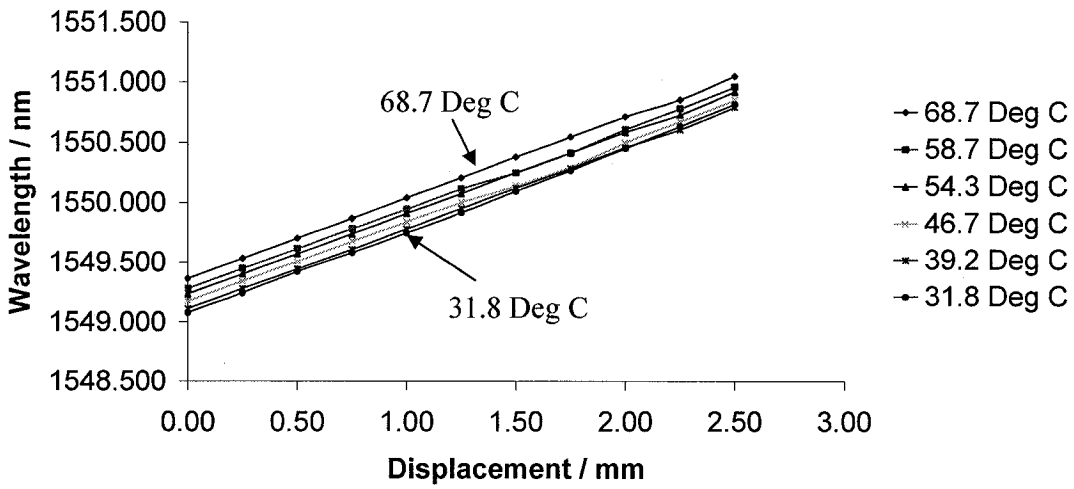

Figure 4-17 Relationship between wavelength, temperature and displacement [20]. Center Wavelength FBG = 1549.109nm at 39.2 Deg C with 0 displacement/force applied. Lg = 10mm; Module length = 50mm; Mask period =1070.59nm; Imprinting Technique = Phase Mask.

First, without any vertical displacement applied, the sensor is heated from 30 °C to 70 °C in the oven. Using the interrogation system from Micro Optics Inc., the Bragg wavelengths at 31.8 °C, 39.2 °C, 46.7 °C, 54.3 °C, 58.3 °C and 68.7 °C are measured. These steps are repeated for vertical displacement ranging from 0.25 mm to 2.5 mm at 0.05 mm increment. From Figure 4-17, it can be seen that the fiber-reinforced Bragg grating composite has a positive temperature coefficient.

4.4.7 Temperature compensation

When an FBG sensor is used to measure pressure or strain, the read wavelength shift information will be erroneous unless the temperature effect on the wavelength shift has been addressed properly. Case Study: When the FBG sensor composite is used to measure earth movement as shown in Figure 4-18, the interrogation system has no intelligence to differentiate between the wavelength shifts caused by temperature changes and by earth movement. Hence, it will attribute wavelength shift information as earth movement unless temperature compensation is performed.

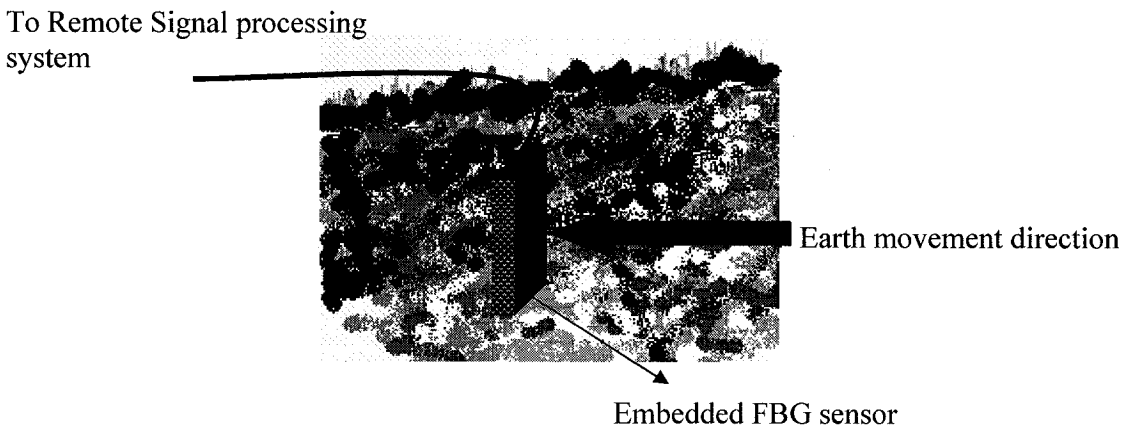

Figure 4-18 FBG sensor buried under the earth surface to monitor the motion of the soil [20].

One way to realize the wavelength shift due to earth movement is by using the temperature compensated strain sensor. This can be done by embedding two FBGs within the same fiber-reinforced carbon composite such that one FBG is embedded in the neutral layer, while the other is embedded above the neutral layer. As discussed in section 4.4.2, the FBG in the neutral layer is insensitive to applied force or pressure; hence, it can be

used as a temperature reference to compensate for temperature changes. An operating principal of temperature compensation is described in Figure 4-19.

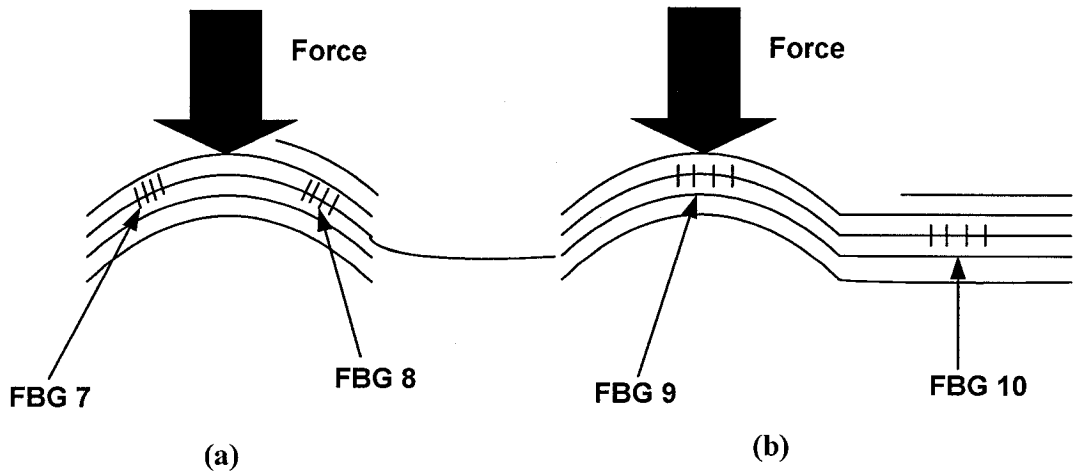

Figure 4-19 Hybrid FBG module (a) Full arc configuration. (b) Semi-arc configuration [20].

The two FBGs under consideration are embedded in the same composite such that they experience the same temperature [16]. In the configuration shown in Figure 4-19(a), the sensor FBG7 experiences wavelength shifts due to changes in both pressure/force and temperature. However, the sensor embedded in the neutral layer experiences wavelength shifts only due to changes in the temperature. The same explanation is applicable for FBG9 and FBG10. Bragg wavelength shift due to force only is found by subtracting the wavelength shifts of the two sensors.

Figure 4-20 shows the test results corresponding to the full-arc embedded configuration shown in Figure 4-19 (a).

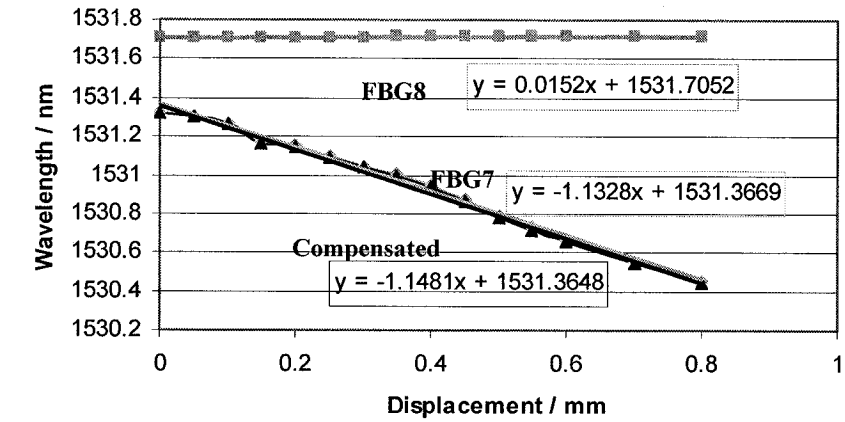

(a)

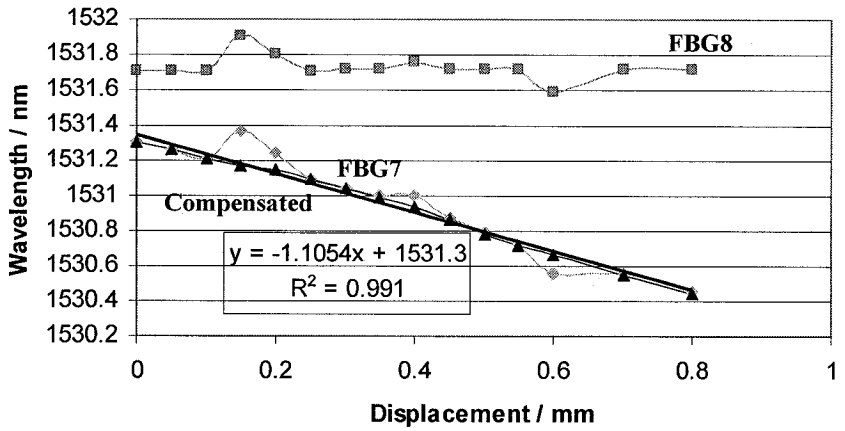

(b)

Figure 4-20 Test results of full-arc configuration. (a) At room temperature. (b) When temperature varies [20]. FBG7 is in 0/FBG7/0/0 configuration while FBG8 is in 0/0/FBG8/0/0 configuration. However, both FBG7 and FBG8 are in a single module. Lg = 10mm; Module length = 50mm; FBG7 = 1531.39nm; FBG8= 1531.712nm; Imprinting Technique = Phase Mask.

Figure 4-21 shows the test results corresponding to the semi-arc embedded configuration shown in Figure 4-19 (b).

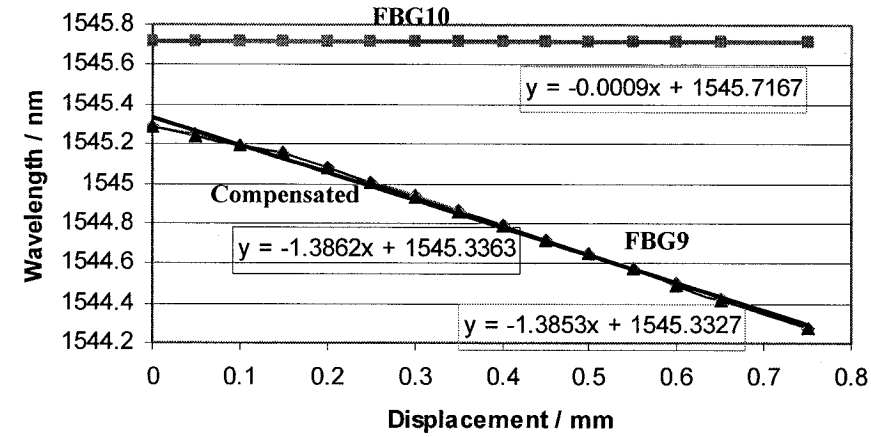

(a)

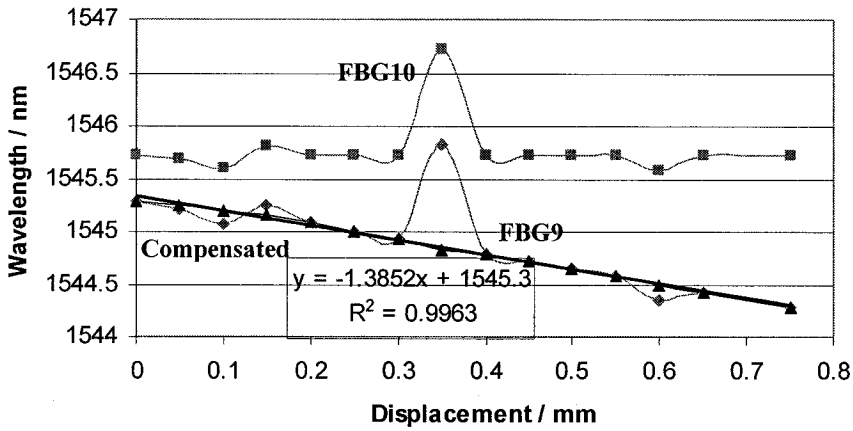

(b)

Figure 4-21 Test results of semi-arc configuration (a) At room temperature. (b) When temperature varies [20]. FBG9 is in 0/FBG9/0/0 Arc configuration while FBG10 is in 0/0/FBG10/0/0 Flat configuration. However, both FBG9 and FBG10 are in a single module. Lg = 10mm; Module length = 50mm; FBG9 = 1545.23nm; FBG10= 1545.68nm; Imprinting Technique = Phase Mask.

To test the operating principle, the fiber-reinforced composite sensor is heated in the oven and then placed in ice. During each of these processes, wavelength shifts are measured only when the readings are stabilized. Both Figures 4-20 and 4-21 show that temperature compensations have been achieved.

4.5 Summary

As the bare fiber or a fiber with cladding is fragile to applied force, it is significantly important to embed the optical fibers. The carbon fiber composite material Fiberdux (913C-XAS) was chosen as the embedding material due to its sensitivity, thermal expansion coefficient and its elasticity till total deformation.

When the grating fiber was embedded in parallel to the axis of the carbon laminar, the fiber was not damaged and the composite added strength to the fiber. The fiber was completely damaged when embedded perpendicular to the axis of the laminar.

The neutral layer in a composite does not change in length when a force is applied perpendicularly. Hence, FBGs embedded in the neutral layer do not show any wavelength shift to perpendicularly applied force. The sensitivity of FBGs increases when they are embedded further away from the neutral axis.

An FBG embedded in the neutral layer was used as a temperature reference sensor. By subtracting the wavelength shift seen in the temperature reference FBG sensor from that of the FBG sensors embedded away from the neutral layer, temperature compensation was achieved.

Chapter 5

FBGI System Design

In this chapter, the architecture of the FBGI system design, optical circuit design and electronic circuit design are studied. This chapter discusses the different approaches taken to design a successful FBGI system. The architectures of the single-board microprocessor-based FBGI design and the DAQ card based FBGI design are presented. The 980nm laser pump circuit design, ASE source design and EDFA design are visited in great detail and the ASE source and EDFA are characterized. The integrity of the GFF is highlighted, experiments are conducted and the gain profile of EDFA is plotted. FFP-TF interrogation and characterization are discussed in detail. Optical receiver circuit and a Sallen-Key filter circuits are designed. The rest of the key circuits in the FBGI schematic are discussed.

5.1 Introduction

Although there are commercial systems available with better-quality performance in speed and accuracy, the cost for purchase and maintenance are prohibitively high. These devices are also heavy and large, and are not suitable for portable applications. In general, the commercial way of simply increasing the number of available channels is done at the expense of available spectrum bandwidth per channel. This is achieved by dividing the total input wavelength spectrum across the required number of channels. This implies that if more channels are needed, each channel has less available light

spectrum and fewer FBG sensors can be installed per channel. Development takes place in two stages; first to design a single channel system and second to design a multi-channel system. Two types of systems are developed. First, efforts are taken to design a compact single-channel FBGI system using FFP-TF. The first one initially uses a SLED light source and then it makes use of the ASE as the light source, which is more successful. However, the disadvantages of the system are the reduction in resolution, speed and the limited capability of only single-channel detection. The second system is developed using a DAQ card and an optical switch for multi-channel quasi-distributed sensing.

5.2 FBGI system architecture

The FBGI system designed can be divided into an interrogation subsystem and a PC-based control subsystem. Figure 5-1 shows the architecture of the single-board microprocessor-based FBGI instrumentation system design. Figure 5-2 shows the architecture of the DAQ card based system with the optical switch for multi-channel scanning.

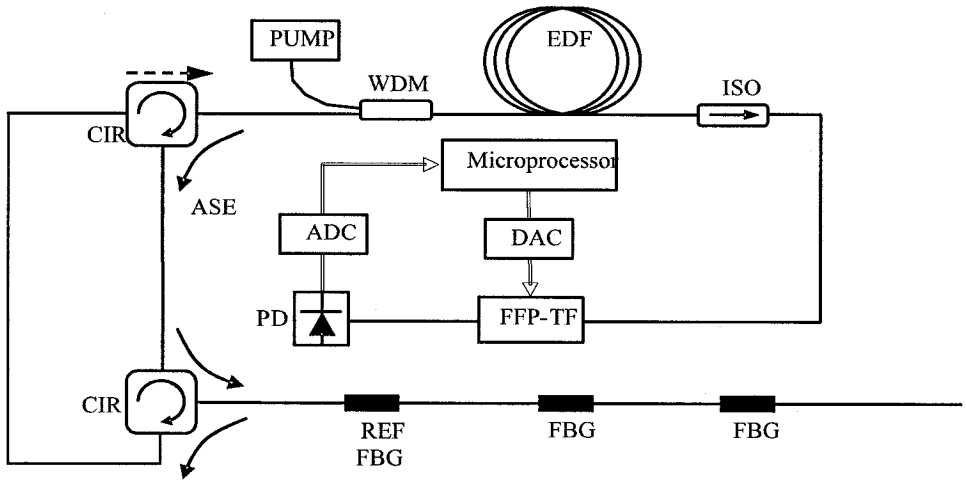

Figure 5-1 FBGI System - Onboard signal processing (Single Channel system).

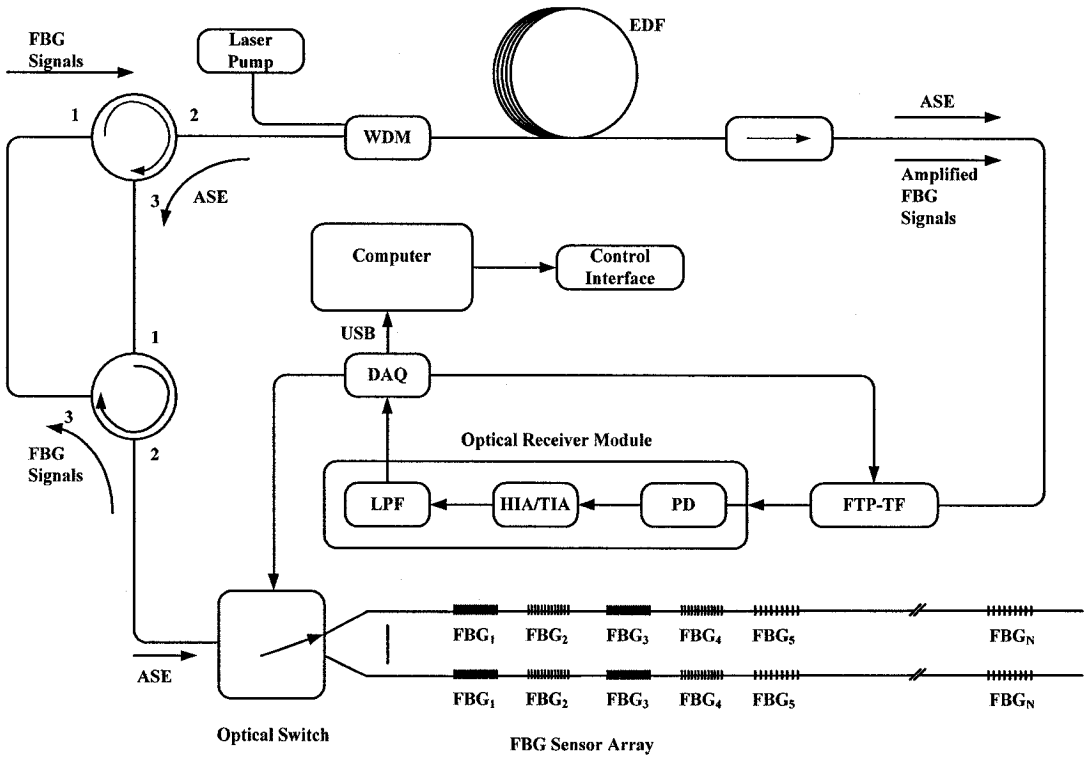

Figure 5-2 FBGI System - Onboard receiver module and a DAQ card [20].

The FBGI interrogation subsystem mainly consists of a combined optical source and an amplifier module, the key tuning element FFP-TF unit, an integrated receiver circuit and a microprocessor-based digital circuit with ADC and DAC. An ASE spectrum is used as the light source to launch light into the FBG array, which then reflects selected wavelengths. Next, the reflected FBG signals are amplified by the EDFA. Amplified FBG reflected signals are super-imposed on the ASE background noise. FFP-TF, which is controlled by the microprocessor via a DAC, scans the whole spectrum where the amplified FBG reflected signals are superimposed on the ASE background noise. It then detects the peak wavelength shifts of the FBG sensors. FFP-TF detected optical signals are then converted into electrical signals by a PD and then the ADC converts them to binary and sends the digitally encoded (binary) values to the microprocessor in the integrated receiver circuit. The transformed signals are then processed by the PC-based software and interpreted into strain information on a graphical user interface for the users. The configuration of using the ASE source also as the EDFA reduces the system cost and size at the expense, however, of signal to noise ratio due to the ASE background noise.

5.3 ASE Source design

5.3.1 The 980nm laser pump module construction

The laser pump module consists of a 980nm laser pump and a driving circuit. The laser pump used from Furukawa features a Fiber Bragg Grating (FBG) on its pig-tail to stabilize the center wavelength [23] [24]. The 980nm laser pump comes with a built-in cooler and a built-in thermistor that can be monitored externally. The driver circuit for the 980nm laser pump is mainly made up of a temperature control block and a current

driving block. The central unit of the temperature control block is a proportional integral loop-based ultra stable temperature controller WTC3243 [25], which maintains ultra-precise temperature regulation using an adjustable sensor bias current amplifier circuit that operates directly with a thermistor built in the laser pump.

The control temperature setting can be adjusted by changing the voltage reference level of pin 2 of WTC3243. This is implemented by using a constant voltage reference IC LM4040-2.5 and adjusting its output voltage by an adjustable voltage divider block. For the current driving block, the central unit is the IC WLD3343 [26], which provides an ultra stable current drive to the 980nm laser pump. To turn on/off the laser pump module, a 0V/5.0V voltage is applied to pin 1, which provides a way for internal digital modulation of the optical output signals of the laser pump. IC WLD3343 [26] provides two operation modes for the laser pump: one is the constant current (CC) mode; the other is the constant power (CP) mode. The selection of CC mode or the CP mode is implemented by either connecting a 1KΩ resistor or a 0.1uF capacitor respectively between pin 5 and pin 6 of IC WLD3343 [26]. This is achieved via a relay which is controlled by the microprocessor. Due to the fact that the laser pump is to be used for ASE source and EDFA in our FBGI system, constant power mode is easier to regulate. The laser pump output level can be adjusted by the voltage reference level of pin 2 of IC WLD3343, which is similar to the way of adjusting the temperature setting [25] [26]. Only manual adjustment is provided and the recommendation is to provide an automatic adjustment via the microprocessor.

Prevention of damage is the key element for construction of the laser pump module. There is insufficient heat removal from the laser pump circuitry which results in "Thermal runaway". The laser pump is stabilized at the set point temperature 25 ^{0}C and then the temperature drifts away. Heat sinks are necessary for proper and safe operation of the laser-pump circuitry [25]. In addition to heat-sinks, a DC 12V fan is added into the laser pump circuitry.

The reference voltage levels and the resistor values for the temperature controller and the current controller are calculated using the design calculator tools available at http://www.teamwavelength.com/tools for those ICs. The Proportional gain and Integral time are kept at 5 and 3s respectively. The control temperature is set to 25°C by setting the reference voltage of IC WTC 3243 to 1.0V. The laser pump rated output power 23 dBm is corresponding to 1.68 V reference voltage level for IC WLD3343 with typical PD current of 4mA. The laser pump output level can be adjusted by varying the reference voltage level "VSET" of IC WLD3343 [26]. The center wavelength of the laser pump is measured using an OSA. The peak λ is at 980.210nm, the spectral width and peak power are 0.103nm and 6.36 dBm at rated power. The extinction ratio is 47.90 dB. The stop band, the wavelength spacing between the upper and lower side modes next to the main mode [27], is 0.205nm.

5.3.2 ASE source construction

ASE source is constructed using an EDF and 980nm laser pump. Figure 5-3 shows the schematic for the ASE source setup. The laser pump chosen consists of a built-in pump stabilizer; this feature eliminates the need to install an isolator between the pump and the WDM coupler [23]. Low-reflection gratings inscribed in the fiber pigtail of the diode laser, which is used to pump ASE source and optical amplifiers, function as pump stabilizers. Since the grating reflects a unique wavelength, the pump laser will force itself to operate at the center wavelength of the grating, and thus the pump efficiency will be high. This way the gratings indirectly contribute to output power stability and the reduction of high-frequency noise [2].

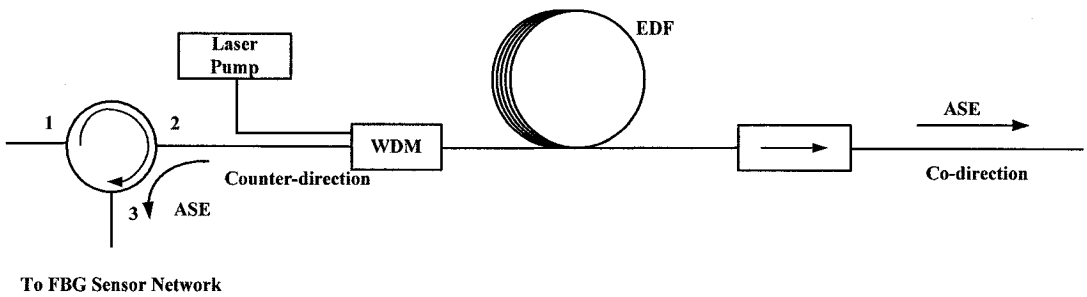

Figure 5-3 Schematic diagram showing EDF acting as an ASE source [20].

The WDM coupler enables the 980nm laser pump to be coupled to the signal fiber with minimum insertion loss while providing a low loss path for the signals [28] [29]. There are WDM couplers available as hybrids with isolators build into it (WDIH) [30]. The initial length of the EDF is 5.70m. The 980nm laser pump is coupled to the EDF through

a WDM coupler. An isolator is placed at the ASE output as an insurance to prevent reflections from disrupting source operation and making the laser pump unstable.

Measurements taken using counter directional and co-directional pumping as shown in Figure 5-4 are tabulated in Table 5-1. Results show that ASE noise has a wideband hill shape spectrum with output power dominant in C band (1520nm-1570nm). These results are in line with the expected characteristics of ASE noise generated by a gain unflattened EDF.

Experiments:

Test Conditions: EDF Length = 5.70m,LD output power = 23 dBm (rated), Set point Temperature= 25 °C, Spectral range ∈ [1520nm, 1570nm] Optical C band.

Results:

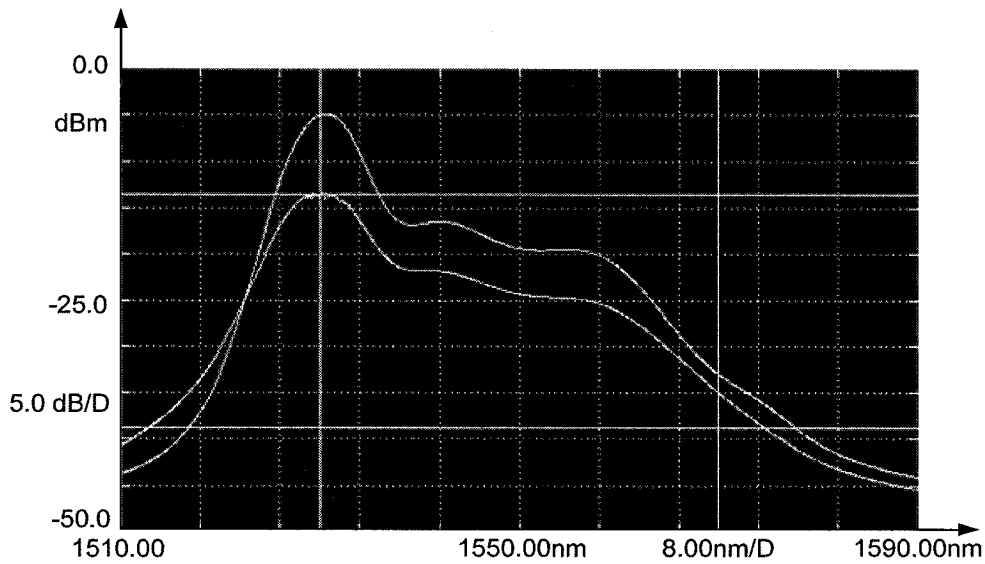

Figure 5-4 Graph of ASE Source; λ_1 = 1530.00nm, λ2 = 1570.00nm, Co-directional pumping = -5.0dBm peak, Counter directional pumping = -13.4dBm peak [20].

Table 5-1 ASE source pumping direction comparison results [20]

Parameters	Co-direction	Counter-direction
1550nm band total power (dBm) (Envelope power)	4.09	1.59
Peak (nm)	1530.4	1529.68
Peak spectral Power (dBm)	-5.01	-13.41
Power @ 1530nm (dBm)	-5.11	-13.61
Power @ 1550nm (dBm)	-19.43	-24.41
Power @ 1570nm (dBm)	-33.11	-35.07

Both co-directional and counter-directional pumping produced the ASE spectrum with steep hump around 1530nm. As shown in Table 5-1, co-directional pumping produces an ASE spectrum with larger total power compared to counter-directional pumping. In general, co-directional pumping has smaller noise figure compared with that of counter-directional pumping [3]. Hence co-directional pumping is adopted for EDFA configuration and counter-directional pumping configuration is used for FBG sensors. With counter-directional pumping, higher gain is possible [3]. Figure 5-5 shows the reflection spectrum of the test results carried out with ASE as source power to a single FBG and on an FBG array sensor configuration.

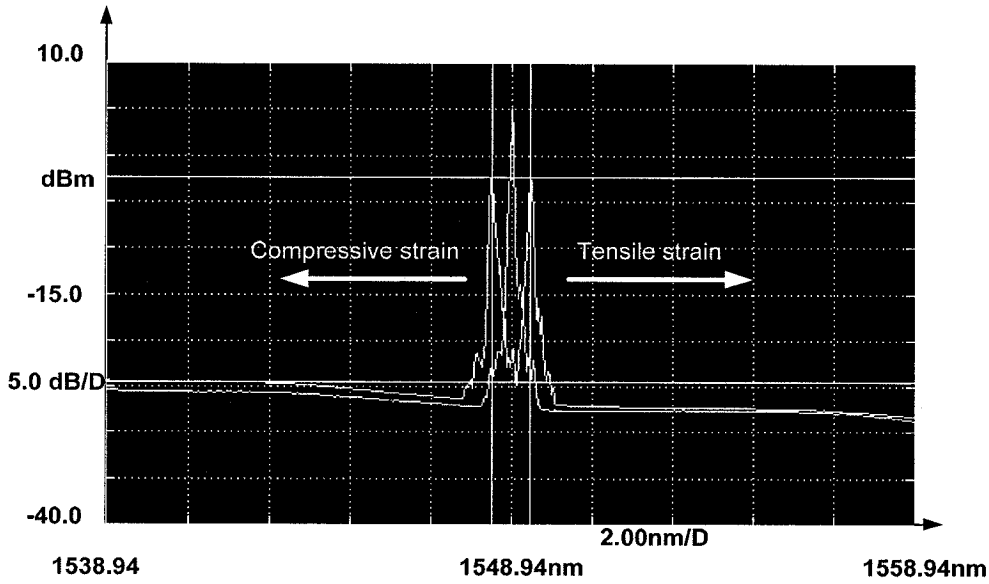

Figure 5-5 Reflection spectrum of FBG sensor modules with ASE source as the input; λ1 = 1548.46nm, Δλ = 0.920nm, ΔL=22.15dB [20].

The peak wavelength separation Δλ is 0.920nm. SNR, the difference of the FBG peak power and the ASE peak noise power, is 22.15 dB. However, due to the low peak power -2.25 dBm of the reflected spectrum the detection had been difficult and the optical receiver only showed a small peak. This phenomenon is shown in Figure 5-6. In an FBG sensor configuration with 8 to 10 sensors, the peak power of the reflected spectrum is even smaller and not even detected by the optical receiver. As a result, amplifying the FBG sensor signals before the optical receiver was deemed necessary. The next section focuses on optical amplifier design for the FBG interrogation system.

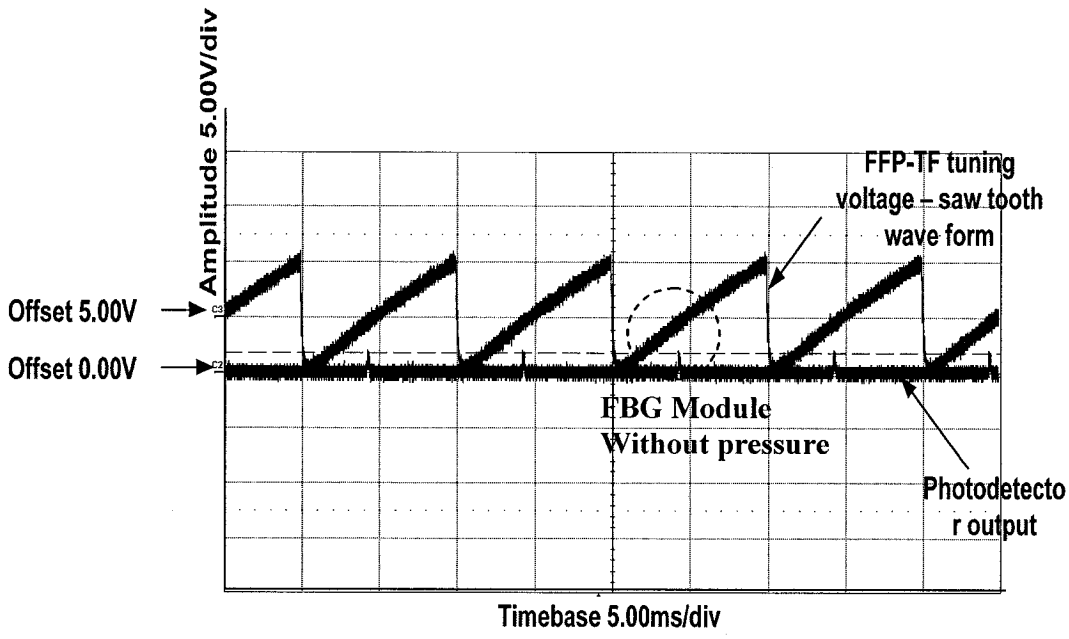

Figure 5-6 Optical Receiver Output of a single FBG sensor and the Tuning voltage of an FFP-TF; EDF length = 8.6m, Ramp up Signal frequency = 100 Hz, Amplitude = 10 Volt peak-to-peak with 5 Volt offset [20].

5.4 EDFA design

For amplifying the signal, both repeaters and optical amplifiers can be used. Though repeaters remove the noise and distortion on the line, they require complex O/E and E/O circuits and they are expensive. In contrast, with inline optical amplifiers, noise and distortion will be amplified with the signals, though there may be cost advantage. For our FBG interrogation system, an EDFA is desirable for signal amplification. The schematic diagram of an EDFA is shown in Figure 5-7.

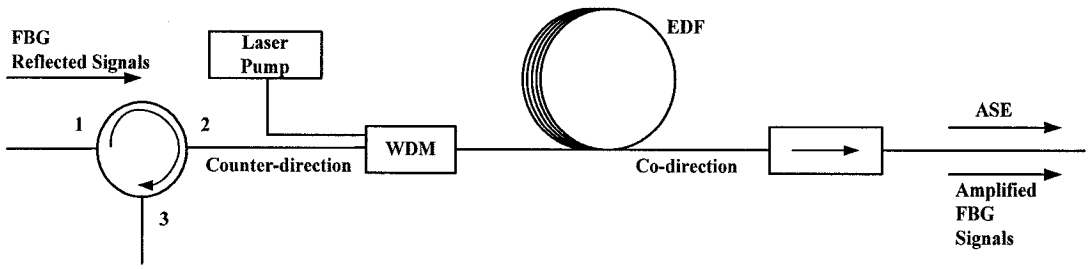

Figure 5-7 EDFA construction, schematic diagram showing an EDF acting as an optical amplifier [20].

A single EDF served as the EDFA and the ASE source for our FBGI system, though this configuration introduced the drawback of having the strong ASE background noise as illustrated in [3].

5.4.1 Amplifier design

The EDFA can be pumped using either 980nm or 1480nm laser pumps [7]. There are certain advantages and disadvantages associated with each pumping configuration. Since 1480nm is close to the EDFA gain spectrum some of the 1480nm pump photons will be

amplified rather than absorbed. More energy is required to maintain the 1480nm's two-energy-level population inversion compared to 980nm's three-energy-level population inversion. Pumping at 980nm is twice as efficient as that of 1480nm. EDFAs using a 980nm pump show less sensitivity to temperature changes whereas those using a 1480nm pump show significant changes in the gain characteristics for temperature changes [7]. ASE is the overriding noise in EDFA. The ASE noise power increases as the pumping power increases. During our tests, it has been shown that the ASE noise power in co-directional and counter-directional configurations are different [3]. It can be shown that ASE noise power is different for the dual-directional pumping as well. Another key factor affecting the ASE noise is the length of EDF. For proper operation, the link power should be budgeted using the following formula [3].

Source power – Total loss + Amplification ≥ Margin + Receiver sensitivity

where, source power is the output power of the ASE source. Amplification is the power gain from EDFA. Receiver sensitivity is the least optical power required by the receiver. Margin denotes the safety buffer.

The total loss includes fiber loss, coupling loss, and insertion loss of various optical devices, and is shown in Table 5-2.

Table 5-2 Loss Estimation for FBGI System Inter-Connects [20]

Items	Max measured insertion loss(IL)
Circulatorx2	0.6x2=1.2dB
980/1550nm WDM Coupler	0.2dB
EDF	Depends on Signal Power and wavelength
Transmission Fiber	0.05dB
1550nm Isolator	0.6dB
FFP-TF	4.5dB
Splice and Connector Losses	0.6dB
Total Loss	≥7.65dB

Gain and absorption coefficients of the EDF are key factors in designing the EDFA [30]. Gain and absorption are functions of length and they, too, depend on wavelength. Figure 5-8 shows the general absorption/gain characteristic of an EDFA against the wavelength.

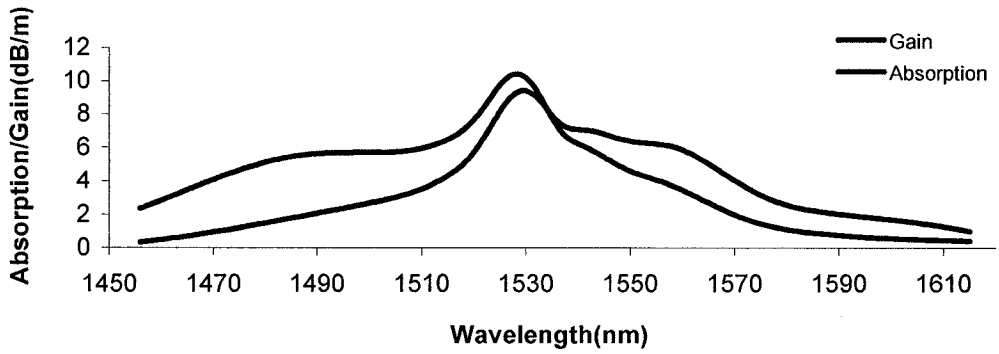

Figure 5-8 Gain and absorption coefficients of EDF-C [31].

However, in our interrogation system, the same EDF is used as the ASE source as well as the EDFA. The gain and absorption also depend on signal power and the pump power. Hence the EDF length required could only be best estimated by experiments. Though a large EDFA gain is desired, depending on the situation, large EDFA gain may result in adverse performance. For example, if the signal power level is high and the EDFA is working in the saturation region, the signal power level would not be increased much, though the Noise power may increase and will reduce the SNR. (Polarization dependent gain) [7].

Test results of the experiments conducted on an EDFA with 5.7m EDF show that EDFA gains for the FBGs are dependent on wavelength, FBG reflectivity and laser pump power, and vary significantly, ranging from 20 to 35 dB. The SNR, defined as the difference between peak power of the amplified FBG signal and the ASE noise peak power, ranges from 18 to 25 dB. Figure 5-9 and Figure 5-10 show the ASE spectrum with the reflected FBG spectrums at 1531.6nm and at 1549.0nm wavelengths respectively.

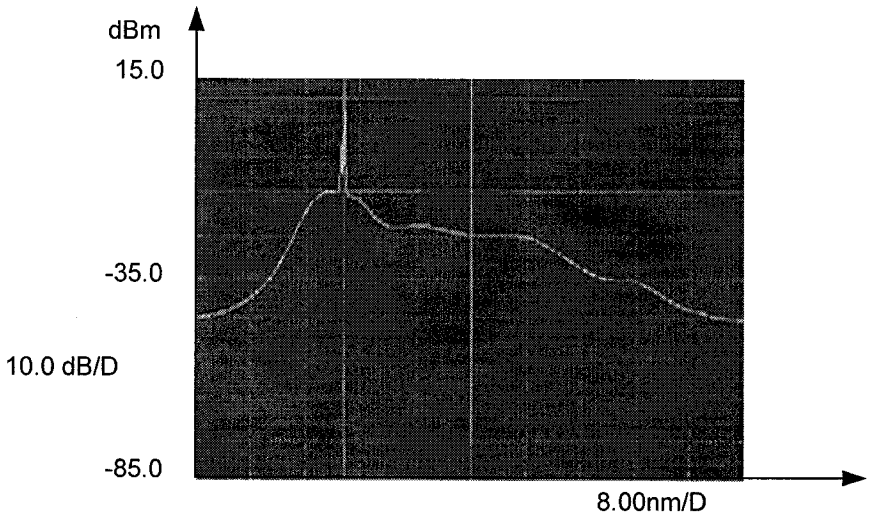

λ1=1531.600nm Δλ=18.320nm;
L1=9.91dBm;ΔL=22.91dB

Figure 5-9 EDFA amplified reflected spectrum of an FBG; EDF length = 5.7m, λ1 = 1531.60nm [20].

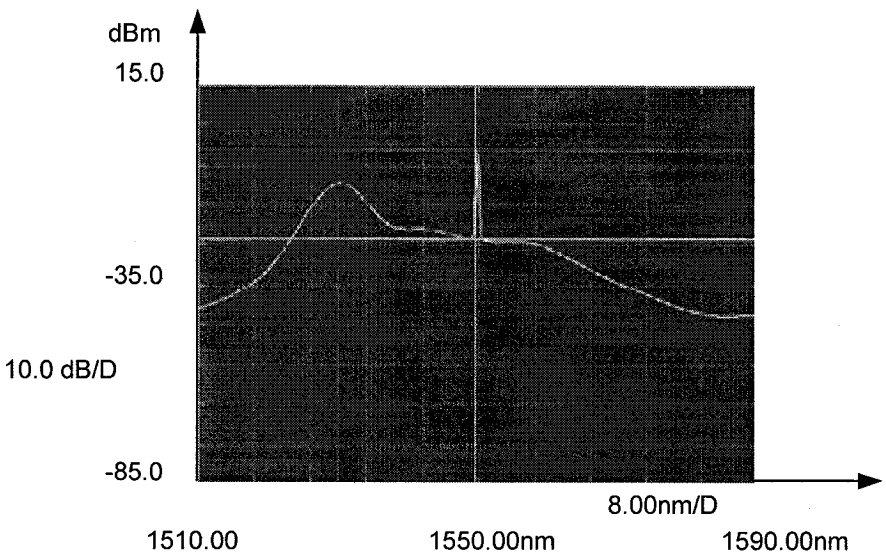

λ2=1549.000nm Δλ=19.600nm;
L1=-0.90dBm;ΔL=22.62dB

Figure 5-10 EDFA amplified reflected spectrum of an FBG; EDF length = 5.7m, λ1 = 1549.00nm [20].

Since the ASE spectrum and the EDFA gain profile are not gain-flattened and have a steep hump at the 1530nm region, the electronic amplifier circuit saturates, as shown in Figure 5-11, when detecting the reflected signals around 1530nm region. Reducing the gain of the amplifier is not possible since the software uses a "threshold level" for detecting the peaks. Reducing the amplifier circuit gain renders the signals in the lower gain area (1570nm-1580nm) of the EDFA undetectable by the software. Hence, the usable spectral range is further reduced. As a result, gain flattening is necessary for increasing the useable spectral range.

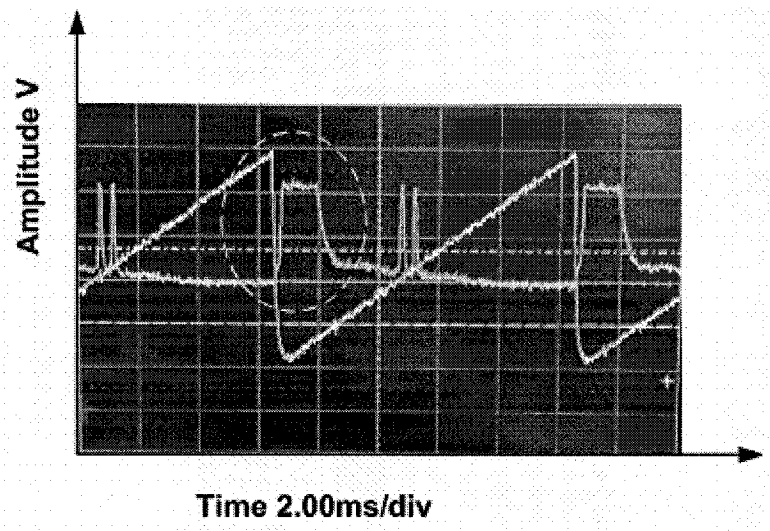

Figure 5-11 SAW-tooth tuning Voltage and Optical receiver output - Saturation observed in the Optical Receiver; SawTooth 2.00V/div, Offset -4.004V; Pulse 5.00 V/div, Offset -707mV; Time 2.00 ms/div; Ramp up driving voltage DC offset = 5 V, 10 V peak to peak, f = 100 Hz; Initial FBG center f = 1531.60nm [20].

5.4.2 Gain flattening

There are many ways [7] to flatten the gain of an EDFA. For instance, the device can be operated at 77°C, and though it produces a fairly flat response, it is not practical. Mixing of other dopant materials, such as Yb (ytterbium) along with Er (erbium) into the fiber core, results in significant improvement in flatness of the gain profile. EDFs with dual cores as well produce a significantly flat gain response. Dynamically controlling the pump power depending on the wavelength to vary the ASE is another way to control the EDFA gain and thus the total amplification. Two common methods are [7] using a Gain Flattening Filter [GFF] to reduce the hump in the gain profile and adjusting the EDF length to optimize the amplifier performance.

Another way to make output signals have almost equal amplitudes is to adjust the power levels of input signals with the knowledge of the gain profile. In practice, it is proposed that the reflectivity of the FBG sensors be adjusted so that the amplified FBG signals have almost the same peak power.

5.4.2.1 Using GFF

The GFF works as an equalizer for the EDFA, whose gains are wavelength-dependent. For the GFF to give a resultant flat gain profile, as shown in Figure 5-12, its own gain profile should inversely match that of the EDFA [32].

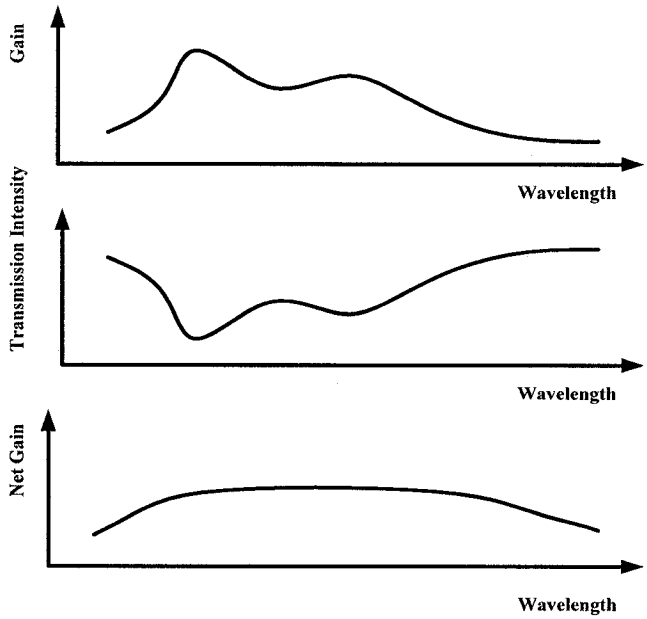

Figure 5-12 Concept of Gain Flattening using GFF [7].

Only then the cross product of these two gains will produce a constant gain, thus relatively flat intensity at all wavelengths in C band. The drawback of basic GFF is its gain profile is static though the EDFA has a dynamic gain profile dictated by wavelength, signal power and pump power. Hence, to get a dynamic flat profile, a dynamic adaptive GFF should be used [33].

5.4.2.2 Adjusting EDF length

As the signal traverses along the EDF, it is amplified and continues to become stronger, whereas the pump power level continues to decrease due to absorption. The gain will start to decrease after a certain length, as the pump power is not enough to handle a

complete population-inversion. In the unpumped section of the EDF, the signal is absorbed and the signal power is lost [3] [7]. If the EDF length is too short, it will result in EDFA saturation and the gain will be very minimal. Hence, selection of optimum length is crucial for EDFA design. Signal and pump power at every point along the EDF are different and so are the gain and absorption spectrums. Amplifier gain for a wavelength is the integral sum of the gain for that wavelength at each point along the EDF at any instant. Hence, by choosing the correct length, we can make the integral sum of the gain for each wavelength relatively constant and achieve a flat gain profile for multi-wavelengths [3] [7]. As a result, finding the optimum EDF length is necessary for EDFA gain flattening. However, due to the shortage of the EDF at our laboratory, the gain flattening tests are only made with four typical lengths: 5.4m, 7.4m, 8.6m and 9.4m. The results of gain flattening tests conducted on different lengths of EDF are shown in Table 5-3.

Table 5-3 Comparison of Gain Flattening Tests results of different EDF lengths with Co-directional and Counter-directional pumping [20]

Parameters	5.4m EDF		7.4m EDF		8.6m EDF		9.4m EDF	
	Forward	Reverse	Forward	Reverse	Forward	Reverse	Forward	Reverse
ASE peak P (dBm)	-6.06	-14.78	-9.47	-14.09	-12.66	-16.68	-18.34	-28.55
ASE ΔP = MAX-MIN (dBm)	23.94	17.72	20.03	16.31	10.01	13.96	22.96	14.95
SNR @ 1530nm (dB)	22.91		21.38		31.25		21	
SNR @ 1550nm (dB)	22.62		30.34		23.62		11.16	

As the measurement of flatness of EDF, ΔP the difference between the maximum and minimum power of the ASE source in C band (1520nm-1570nm) is used. The smaller the ΔP, the flatter the ASE curve and thus the flatter the EDFA gain profile. SNR is the difference of the peak power of amplified FBG signals and the maximum power of ASE background noise. The higher the SNR of the FBG sensor peaks, the easier and more stable for the signal-processing module to detect them. Results show a linear relationship with laser pump power. The device is operated at the rated power of the laser pump as the SNR and the signal power of the amplified signal are the highest at the rated power. As a result, only the test results at the rated power are presented in the thesis. The power of the ASE drops because of absorption as the length increases. ΔP and SNR reaches the maximum for the EDF length at 8.6m and are starting to decrease with either decreasing or increasing the EDF length. Hence, the optimum EDF length is found to be 8.6m.

An EDFA does not distort the signal at saturation, but rather applies reduced gain at saturation. Figure 5-13 shows the gain saturation graphs for an electrical amplifier and for an EDFA. As shown in Figure 5-13, an electronic amplifier distorts (clips) the signal significantly at saturation [7].

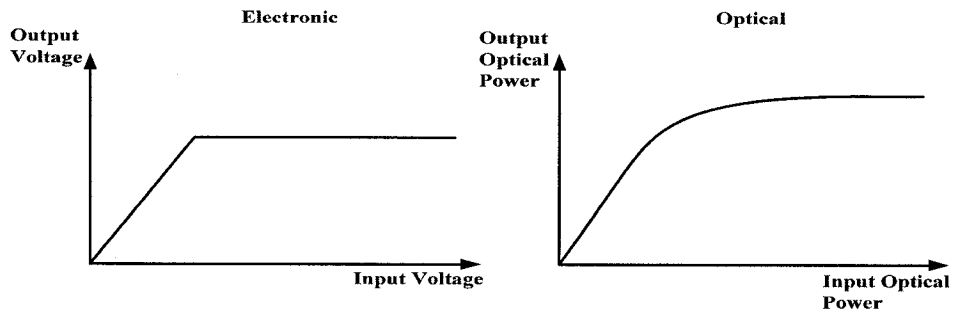

Figure 5-13 Gain saturation and the response of an electrical amplifier and an EDFA [7].

5.4.3 Gain and noise profiles

Amplifier gain and the noise figure of the amplifier are two vital characteristics which play important roles in determining the performance of an optical amplifier. The ratio between signal-to-noise ratio (SNR) at the input to the SNR at the output will give the noise figure of the amplifier. The gain profile and noise profile of the amplifier are dependent on input laser pump power, signal power level and wavelength [7]. To study further, a "Gain Profile" experiment is conducted which mainly consists of an Optical Spectrum Analyzer (OSA) and a tunable laser. Fine adjustment of the output power level and the peak wavelength is made possible with the use of the tunable filter. The output level of the tunable laser source, without being subjected to any amplification, via the EDFA, is first measured by connecting it directly to OSA. Next, the output level is measured again with EDFA amplification. The difference in the amplitudes gives the gain introduced by the EDFA at that particular wavelength. This amplitude difference can be plotted against wavelength and input power level to obtain the gain profile of the

amplifier. After the optimum EDF length is found, gain profile and noise profile measurements are taken again at this optimum EDF length.

In fact, the gain profile and noise profile measurements are not significant to our FBG interrogation system because the useful information is encoded in wavelengths and is interpreted from the peak wavelength shift taking place in the reflected FBG spectrums. However, in the digital optical communication, the amplitudes of the signal are very important and each channel should have the same amount of gain e.g. for a WDM system [7].

The tests are still conducted to gain a full understanding of gain and noise profile of the EDFA. Due to the fact that the measured peak power of un-amplified FBG signals, including single FBGs and FBG arrays, ranges from – 12 dBm to –25 dBm, the EDFA tests are conducted with input signals of the tunable laser, whose peak power is limited to the range of –8.00 dBm to – 28.00 dBm. Figure 5-14 shows the spectrum of the tunable laser output before and after amplification by an EDFA. The EDFA outputs are measured by an Advantest Q8384 OSA for wavelengths varying from 1510nm – 1580nm and the Gain Profiles are plotted as shown in Figure 5-15.

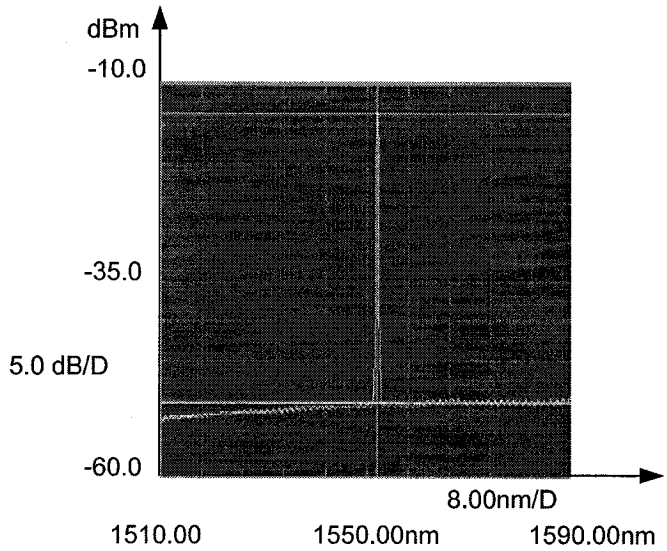

λ1=1552.080nm
L1=-13.510dBm;ΔL=36.69dB

(a)

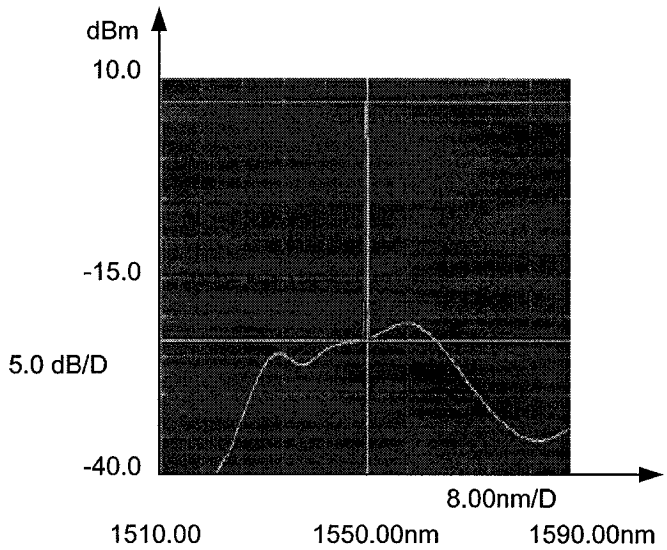

λ1=1550.160nm
L1=7.20dBm;ΔL=30.10dB

(b)

Figure 5-14 Tunable laser output (a) Before and (b) After amplification by an EDFA [20].

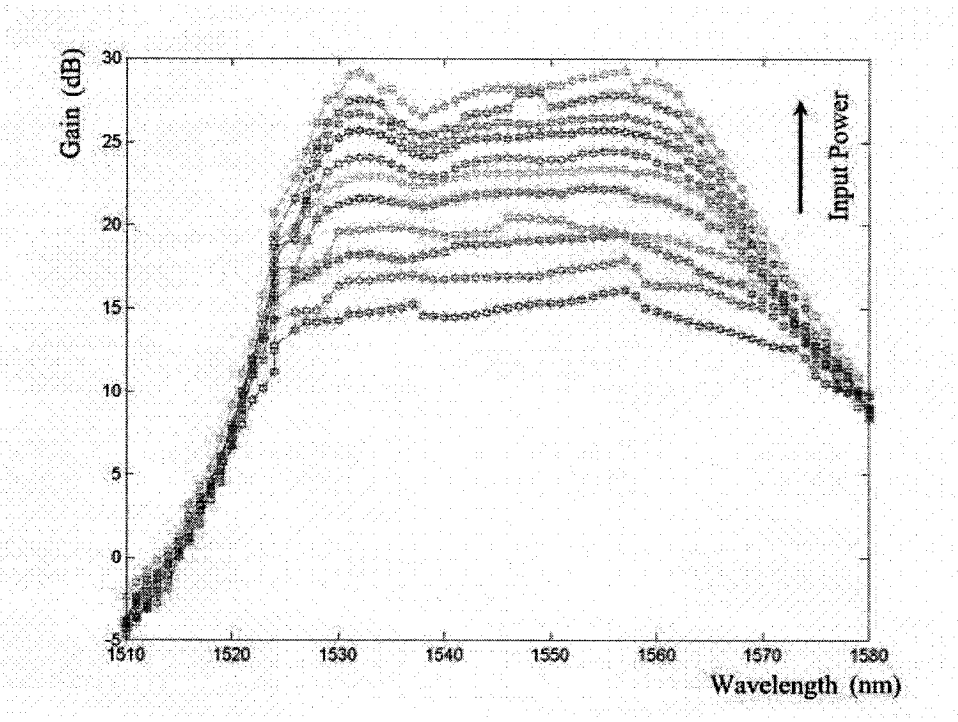

Figure 5-15 EDFA Gain profiles, characterized with tunable laser source input with peak power ranging from –8.00 dBm to – 28.00 dBm [20].

The experimental results as shown in Figure 5-15 confirm that the gain profile of the EDFA is dependent on the wavelength and the input signal power. Gain of the EDFA increases with the increase in the input power. Hence, we can conclude that an input signal at different wavelength with different power level will be amplified by a different gain factor by the EDFA. It can be seen from Figure 5-15 that EDFA gains are largest and relatively flat from 1530nm to 1560nm. The noise profile is very similar in shape to the gain profile of the EDFA. It is proven from these gain profile and noise profile measurements that EDFA gain is dependent on the wavelength and the input power.

5.5 FFP-TF interrogation

This section discusses the circuit design of FFP-TF interrogation. A scanning FFP-TF from Micron optics with 60nm FSR is selected to use on the single-board FBG interrogation design. In addition, provision is made on the PCB to incorporate an FFP-TF from NP Photonics. The advantages of the FFP-TF from NP Photonics include temperature stabilization through a built-in temperature sensor (thermistor type) that can be monitored externally, high repeatability and continuous compensation for optical performance. The scanning speed of the FFP-TF from NP Photonics is low in the range of 1-10Hz. Figure 5-16 shows the cross section of an FFP-TF [7] [34].

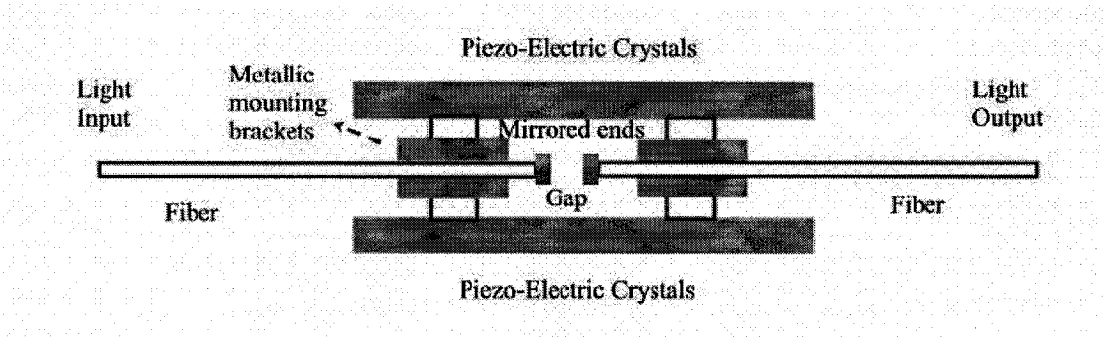

Figure 5-16 Cross section of a Fiber Fabry-Perot Tunable Filter [34].

The two piezo-electric crystals (PZTs) provide the means to alter the distance between the mirrors and thus to tune the resonant wavelength. When the applied voltage across the crystals is varied, the distance between the ends of the fibers is changed and thus the resonant wavelength is changed. In practice, a saw-tooth voltage waveform is used to vary the voltage across the crystal such that FFP-TF can continuously scan the

wavelengths of the input signals. The higher the scanning speed, the larger the bandwidth and the smaller the Finesse, which leads to lower scanning accuracy. Hence, the scanning speed should be compromised to achieve better accuracy. The frequency of the saw-tooth waveform will decide the scanning speed of the FFP-TF, which essentially decides the Finesse of the FFP-TF output. Figure 5-17 shows the characteristics of an FFP-TF with fixed FSR for different Finesse values. Free Spectral Range (FSR) is defined as the frequency separation between adjacent fringes (transmission peaks) of the FFP-TF output [7]. It might be viewed as the measurement window or frequency bandwidth of the FFP-TF [36]. "Finesse" is the ratio between the energy in the filter to the energy passing through it. "Finesse" is expressed as the ratio of "Free Spectral Range" to the "Full width half maximum" spectral width of the transmission fringes. The higher the Finesse, the narrower the spectral width of the transmission peaks with sharp boundaries leading to higher resolution in measurement [7].

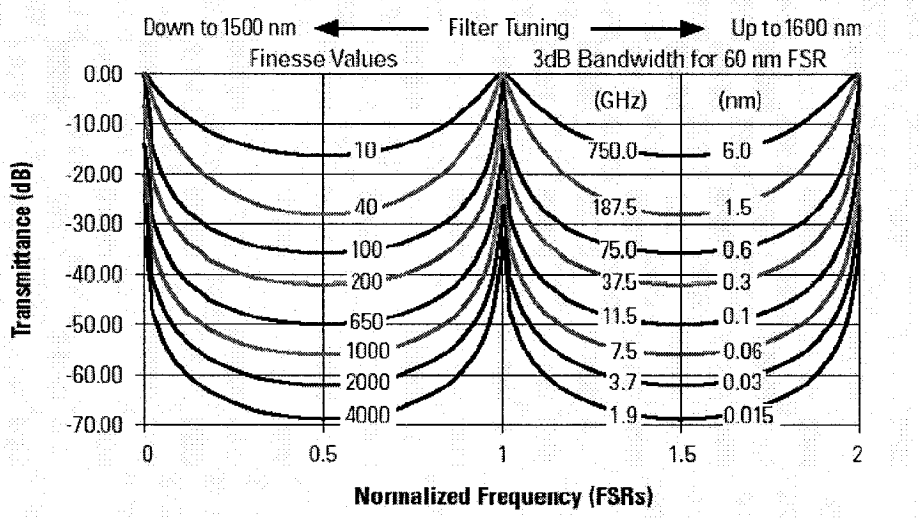

Figure 5-17 Normalized frequency vs. transmittance of an FFP-TF with a fixed FSR [34] [35].

The relationship between the frequency and the 3 dB bandwidth shown in the Figure 5-17 satisfies the relationship $c\frac{\Delta\lambda}{\lambda^2} = \Delta f$; where $c = f\lambda$, c = speed of light ~3x10^8 m/s, center wavelength λ = 1550nm, $\Delta\lambda$ is the 3 dB bandwidth and f is the center frequency.

In order to characterize the FFP-TF as shown in Figure 5-18, measurements are taken with the FFP-TF to check its linearity for different input voltages, before mounting it on the FBGI system. The test resolution is limited by the minimum step size of the tunable power supply. Hence, the manual measurements taken only serve the purpose of verifying the linear relationship between the filter peak wavelengths and the tuning voltage. For FFP-TF control with high accuracy, the FFP-TF response should be measured by using an ADC and a microprocessor (or a DAQ) controlled by the PC-based program and a DAC (or a DAQ). The testing voltage range is limited to 11V.

Test Conditions:

Ambient Temperature: 23°C or 296 K; Test Spectral Range: 1510nm to 1580nm

Test Analog Tuning Voltage Range: 0V to 11 V; Test Resolution: 0.05 V

Test Results: (FFP-TF S/N: TF01S7)

FSR = 61.075nm ; FWHM= 3 dB BW = 0.13nm

$$Finesse = \frac{FSR}{FWHM} = \frac{61.075nm}{0.13nm} = 469.808$$

Insertion Loss = 4.29 dB

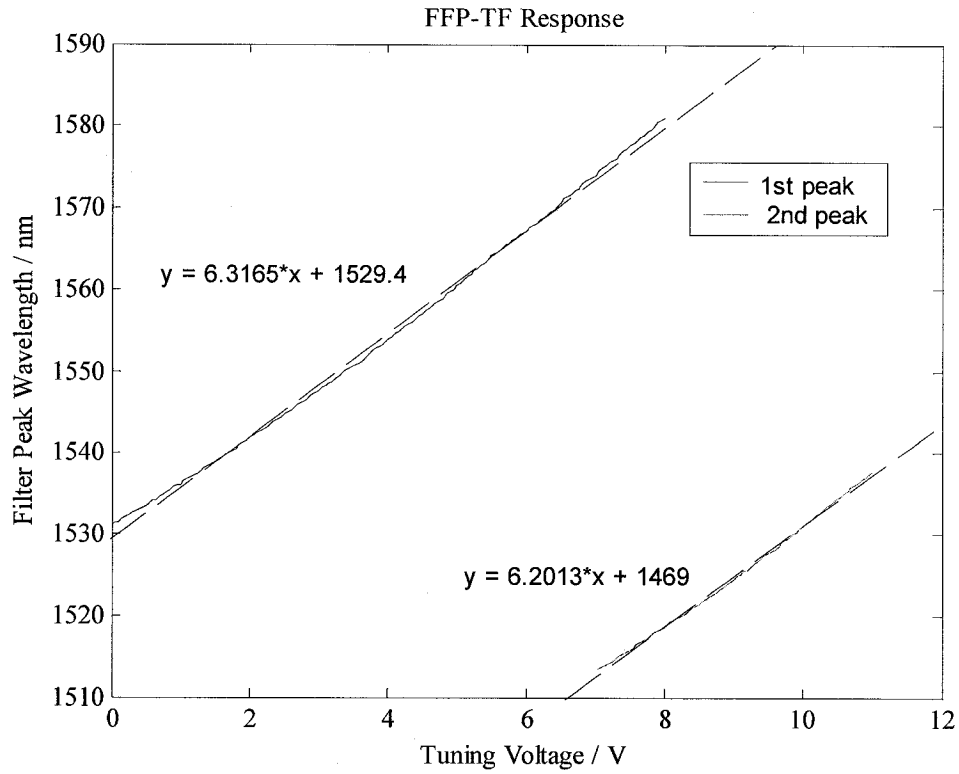

Figure 5-18 Tuning Voltage vs. Filter Peak Wavelength of an FFP-TF.

From Figure 5-18, though it can be seen that the FFP-TF response was non-linear, it can be approximated by a linear curve. It would be more accurate if the non-linear response curve is considered as many linear segments. However, this will complicate the FFP-TF control algorithm required to control the tuning of the FFP-TF. Hence in the software implementation, the non-linear response curve is broken into limited linear segments.

As shown in Figure 5-19, a saw-tooth voltage wave form is used for tuning both in digital and analog domain. In the digital domain, a 16-bit DAC is made available to control the tuning voltage of the FFP-TF. Higher resolution finer steps of the FFP-TF voltage tuning can be achieved at the expense of scanning speed. Hence, a new method is adopted in the

software algorithm to control the FFP-TF, not at the compromise of the scanning speed. Fine sampling (high resolution/smaller sampling steps) at the center of the peak regions, as actual information encoded in the peak wavelengths, is implemented. At the non-center region of the peak regions, coarse sampling (low resolution/larger sampling steps) is carried out. Note: at voltages around 6V the 2nd fringe order values are seen in the tested spectrum of 1510nm – 1580nm.

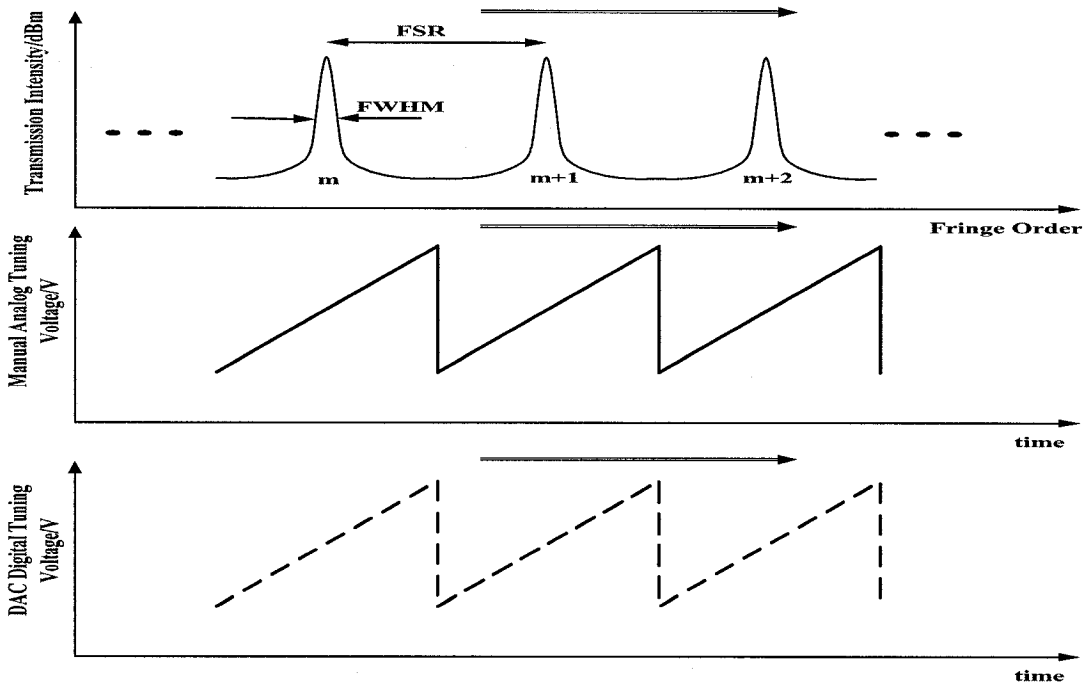

Figure 5-19 Concept of an FFP-TF tuning [34].

The FFP-TF output is the convolution of the FFP-TF pass band spectrum with the FBG signal spectrum. The output is optimized when the spectrum matches that of the FBGs [3] [8]. Figure 5-20 [34] displays the superimposed wavelength shift in the FBG on the output spectrum of the FFP-TF, which continuously tracks the input signals. By monitoring the wavelength changes associated with the reflected peaks of the FBGs, the

information encoded in the wavelength shifts of the FBG sensor signals can be used to measure the perturbations that cause the changes. However, the drawback of this FFP-TF narrowband scanning technique is that it only samples a narrow slice of optical spectrum at a given time [8]. Due to this, the real-time information encoded by the FBGs whose spectrums are located outside the narrow slice region at that given time is lost permanently. In order to increase the measurement accuracy and resolution, the detection speed should be improved significantly to capture the full knowledge of the whole signal spectrum within a very short time slot. Increasing the scanning speed of FFP-TF has limitations. Theoretical scanning speed of FFP-TF can be increased to 2.5 KHz. However, due to the "Finesse effect" explained above and the "Hysterisis-effect" [34], the maximum recommended scanning speed of FFP-TF is too high. In practice, only around 300 Hz FFP-TF scanning speed is utilized for better accuracy. Nevertheless, this speed was fast enough for the requirements of the research. This speed penalty and information loss can be avoided by implementing a parallel detection technique such as an array wave guide and PD interrogation or a CCD device [8].

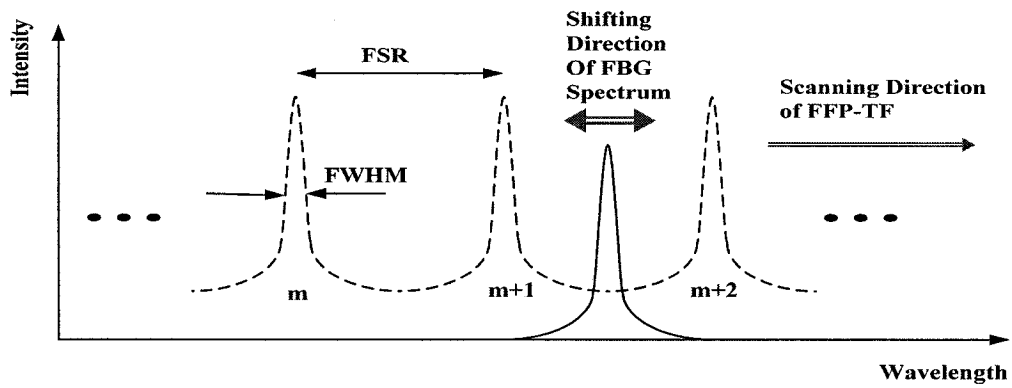

Figure 5-20 FBG Interrogation using an FFP-TF [34] - Continuous scanning by FFP-TF and the superimposed reflected spectrum from an FBG.

5.6 Optical receiver design

5.6.1 Basic optical receiver design

During the design, PIN-TIA module is considered for use as the receiver module. However, it is not chosen as the experimental results showed that the output of the PIN-TIA module contained around 3.1 V DC offset. Though offset correction circuits can be used to remove or compensate for the offset, an InGaAs pin PD was chosen as it is a straight forward design and matches our FBGI design requirements. The minimum responsivity and sensitivity of the PD is ~0.7 A/W and -34 dBm, respectively. The spectral range is from 1250nm to 1600nm (another PD showed a spectral range of 800nm – 1800nm), which covers the ASE source and our FBG signal spectrum. The speed is up to 2 GHz, which is much higher than that of the FFP-TF. The cost of a single PD is much lower than that of a PIN-TIA module.

The basic optical receiver shown in Figure 5-21 consists of the PD circuit and an amplifier circuit. The PD is used to generate the photocurrent signals proportional to the input optical power signals incident on the PD, The task of R_o is the I/V conversion, which basically transforms the photocurrent signals into voltage signals, because most signal processing ICs accept only voltage input signals. The PD must be reverse biased to create the depletion region so as to capture the incoming photons [3]. A photodiode shows a good linearity to incident luminance when it is reverse biased [37]. The reverse current that the PD can take is limited to 5 mA, and a 1 KΩ resistor $\left(R_{\text{lim}} = \frac{5V}{5mA} = 1K\Omega \right)$

is used to limit this current through the PD, which is shown in Figure 5-21. The 68 pF capacitor serves the purpose of suppressing the fluctuations in power supply.

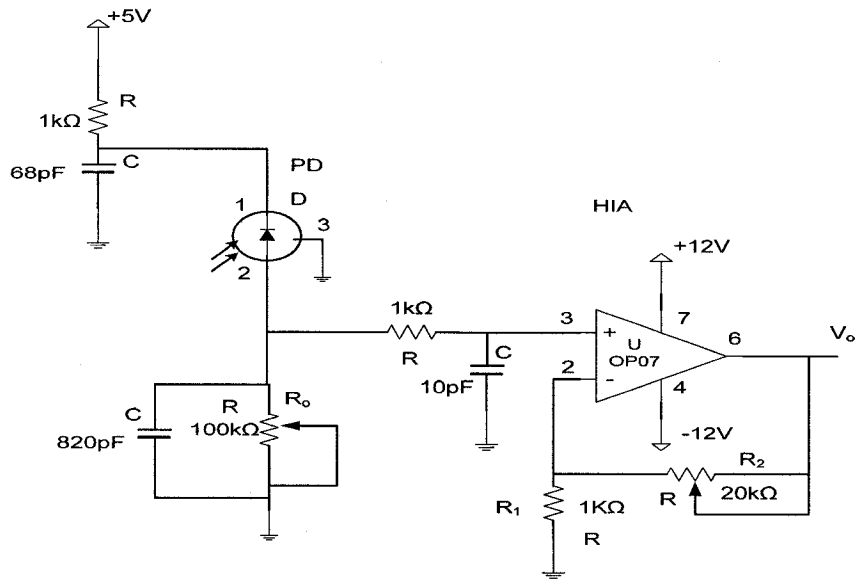

Figure 5-21 Optical receiver circuit.

High frequency noises are attenuated by passing through the capacitor to the ground. The capacitor behaves like a short circuit to high frequency signals. The DC power supply is not affected because the capacitor is an open circuit to DC signals [38]. In figure 5-21, the circuit is mainly made up of an I-to-V block and an inverting amplifier block. By making the resistor R_o variable, the PD output conversion ratio can be adjusted for different FBG sensors. Strong FBG signals produce a strong PD output and thus a high output voltage. This is usually the case of a single FBG sensor. On the other hand, in the case of the FBG array, the reflected signal strength will be low and thus the output voltage signals from the PD circuit will be small in amplitude. This is due to the low ASE

source power and the splice losses at each FBG sensor. The voltage output signals are affected by the reflectivity of the FBG sensors as well [3]. This is also the reason for the variable gain inverting amplifier design. The inverting amplifier consists of IC OP07 and two resistors R_1 and R_2.

The gain of the inverting amplifier is given by [38].

$$A_{inv} = 1 + \frac{R_2}{R_1}$$

The gain of the I-to-V conversion circuit of the PD is given by:

$$A_{TIA} = R_o A_{inv} = R_o\left(1 + \frac{R_2}{R_1}\right)$$

$$R_o \uparrow \Rightarrow A_{TIA} \uparrow \; and \; R_2 \uparrow \Rightarrow A_{TIA} \uparrow$$

The additional 1 KΩ resistor and 10 pF capacitor forms a simple RC LPF with corner frequency 15.9 MHz. The corner frequency is not significant here as the noise is removed stage by stage and at this stage, the purpose is to remove high frequency noise.

$$T(s) = \frac{Z_C(s)}{Z_C(s) + Z_R(s)} = \frac{1}{1 + sCR}$$

$$\Rightarrow T(j\omega) = T(s)\,|_{s=j\omega} = \frac{1}{1 + j\omega CR} = \frac{1}{1 + j2\pi fCR}$$

$$f \uparrow \Rightarrow T \downarrow$$

Since the LPF circuit is before the amplifier the high frequency noise is filtered before the signals are amplified by the inverting amplifier.

Note: By using the op-amp in trans-impedance (TIA) configurations, the current of the PD can be converted into voltage, still offering a high-impedance to the input device (PD). This configuration protects the input device from loading effects [39].

5.6.2 Filter design

It has been realized during the single-board microprocessor-based design that a separate filter on the optical receiver output will help to filter the noise at the input to the ADC and thus a simple Sallen-Key LPF is designed during the DAQ card system design and implementation. Due to the hardware limits, the maximum scanning frequency (the cycling speed over one Free Spectral Range (FSR)) should be less than 2.5 KHz [34]. Since the amplifier output signal frequency f_s is equal to that of the FFP-TF scanning frequency, the amplifier output signal frequency f_s should also be less than 2.5 KHz. As a result, 5KHz is chosen as the -3dB frequency f_1 of the Sallen-Key LPF [40]. Noise with frequency higher than 5 KHz is suppressed and the signal frequency of interest passes through the LPF. Before proceeding with the design, the attenuation in the stop band needs to be specified. Hence, 20dB attenuation is decided at the 20 KHz. The magnitude of frequency response of the n^{th} order Butterworth LPF is given by:

$$|T(j\omega)| = \frac{1}{\sqrt{1+W^{2n}}}$$

where "W" denotes the angular frequency for the un-scaled filter. It can be shown as below that a 2^{nd} order filter is sufficient. Using a higher order filter than required will introduce a large amount of electrical noise.

$$20 \log |T(jW)| = -20 \log \left[1 + W^{2n}\right]^{\frac{1}{2}}$$
$$\Rightarrow 10 \log \left[1 + W^{2n}\right] = K$$
$$\Rightarrow n = 1.659 \Rightarrow N = [n] = 2$$
and
$$W = \left(10^{0.1K} - 1\right)^{\frac{1}{2n}} = \left(10^{0.1\times 3} - 1\right)^{\frac{1}{(2\times 2)}} = 0.999 \text{ rad/s}$$

The Sallen-Key LPF function is given by: $T(s) = \dfrac{A}{s^2 + (3-A)s + 1} = \dfrac{A}{s^2 + (1/Q)s + 1}$,

where, "Q" is the quality factor of the filter. At Q = 0.707, the LPF produces maximally flat response. The amplifier gain A = 1.586 is the DC gain of the un-scaled LPF. The values chosen for the gain resistors R_1 and R_2 of the unscaled sallen-key filter are 10kΩ and 5.86kΩ respectively. However, 5.6kΩ is chosen for R_2. Frequency scaling is done to translate the response to new frequencies. The unscaled filter is designed with normalized frequency of 1 rad/s. For our Sallen-Key LPF, the frequency scaling factor α and the capacitor values are given by:

$$\alpha = \frac{\omega}{W} = \frac{2\pi \times 5K}{0.999} = 31447.374; \quad C' = \frac{1}{\alpha} = 31.8\mu F.$$

To use the 2kΩ instead of 1Ω resisters, the impedance scaling factor β is given by (keep RC constant): $\beta = \dfrac{2K}{1} = 2\times 10^3; \quad C'' = \dfrac{C'}{\beta} = \dfrac{1}{\alpha\beta} = 15.9pF.$

15pF capacitors are chosen as 15.9pF which is rarely available in the market. The transfer function of the scaled Sallen-Key LPF is given by:

$$T(s) = T_o(p)\Big|_{p=\frac{s}{\alpha}} = T_o\left(\frac{s}{\alpha}\right) = \frac{1.586}{\left(\frac{s}{31447.374}\right)^2 + 1.414\left(\frac{s}{31447.374}\right) + 1}$$

$$= \frac{1.56845 \times 10^9}{s^2 + 4.447 \times 10^4 s + 9.889 \times 10^8}$$

As shown in Figure 5-22, MATLAB simulation is carried out to estimate the practical performance of the designed Sallen-Key LPF.

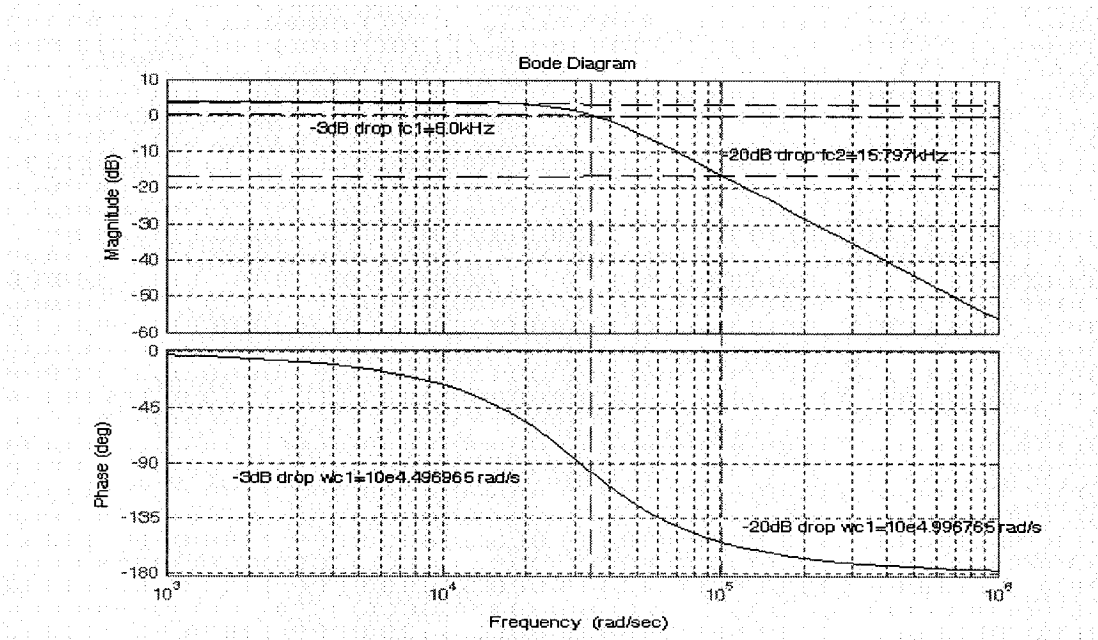

Figure 5-22 MATALB simulation of the Sallen-Key LPF Transfer Function.

The design specifications match the results for the 3 dB frequency. The round-off effect of the order *n* to 2 result in lowering the upper cutoff frequency to 15.797 kHz. Hence, the magnitude frequency response curve has a –3 dB cutoff frequency at 5 KHz and an attenuation about 20 dB at 15.797 KHz. The entire optical receiver circuit with the Sallen-Key Filter is shown in Figure 5-23.

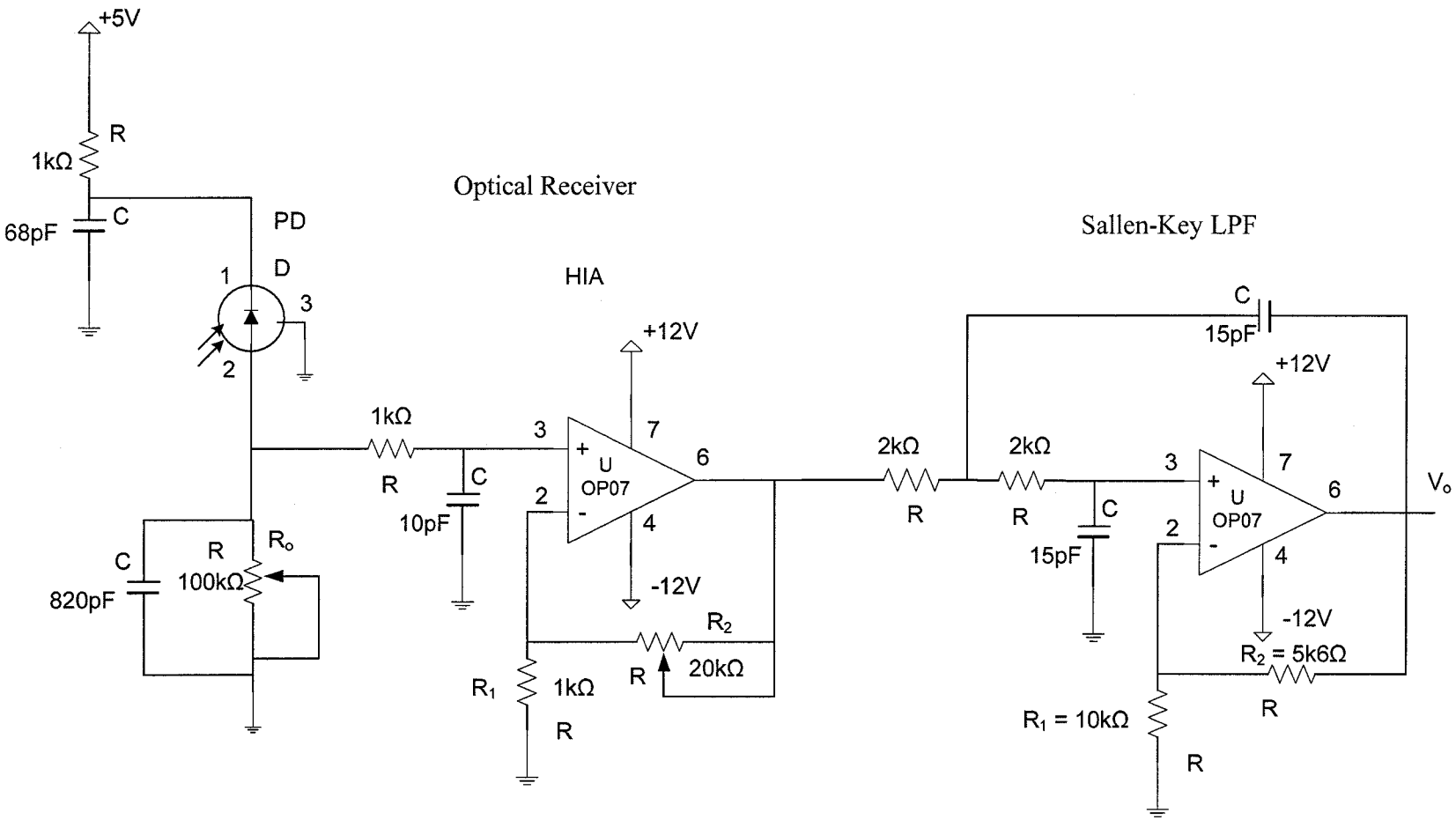

Figure 5-23 Integrated optical receiver circuit [20].

5.7 Microprocessor circuit design

The processor ADSP-2181 used on the single board FBGI system design is selected with the purpose of keeping the central processing unit on the main printed circuit board. However, since main software work is done on a PC, the processing power of the microprocessor is not fully utilized. In this design, the processor essentially operates as an interface between the back-end devices such as ADC, DAC, the display and the front-end device, in this case, a PC connected through a serial port.

The processor comes with an 80 Kbyte of programmable internal memory. An external 128 Kbit flash is provided for additional memory requirement. ADSP-2181 is catered for digital signal processing and other high speed processing. The processor supports external interrupts and interfaced to the back-end devices through Data/Address transceivers. Transceivers are inserted to take care of the peripheral device's current and impedance matching requirements and the load driving capability of the processor.

5.8 ADC circuit

For the on-board system design, A SAR (successive approximation) type 16-Bit Analog to Digital Converter (ADC) ADS8342 from Texas Instruments is selected to sample the output from the optical receiver circuit. The ADC sampling speed can be 250 Kilo samples per second (KSPS) and can multiplex between 4 input channels, with no missing codes. 250 KSPS sampling rate is selected considering the possible multiplexing during

sampling and the future need for the increased sampling rate. Though 3 optical receiver circuits are designed and are interfaced to the ADC, only one optical receiver circuit and thus one ADC channel is effectively used. The ADC is powered with +/- 5 V supply and is designed to take input signals up to + 2.5 V, though the ADC can take bipolar inputs up to +/- 2.5V. ADC is interfaced to the processor via a parallel 16-bit data bus, 2 address lines, interrupt line and control lines to do chip select, start conversion and read enable line. ADC is fed with a 10 MHz external clock and provides an internal clock frequency of 5 MHz. The resolution of the ADC is $(2.5V/(2^{16}/2)) = 76.29\mu V$. If the reference voltage is low, the LSB weight of the ADC resolution will be lower than 76.29 μV and hence the noise susceptibility will increase. A 0.1 μF ceramic capacitor is specifically connected very close to the "REFIN" pin of the ADC to reduce the noise coupling into this high impedance input. The noise in the ADC code is compensated by implementing a moving average filter inside the software.

Since the SAR type ADC is sensitive to noise on the power supply, ground and digital lines such as data and clock lines, extra care is taken during layout to provide quieter supply and ground planes and digital lines. In addition 0.1 μF filter capacitors and 10 μF tantalum capacitors are placed closer to the supply pins to bypass the noise and to stabilize the supplies to the ADC.

5.9 DAC circuit

For the on-board system design, a 16-Bit-monolithic type Digital to Analog Converter (DAC) AD669 from Analog Devices is selected to produce a saw-tooth voltage output to control the FFP-TF. The control of the FFP-TF voltage is implemented by directly connecting the DAC output to the FFP-TF voltage input pin or by connecting DAC output to linear power supply first and connecting the linear power supply output to the FFP-TF input. Implementation deferred depending on the current requirements of the FFP-TF used.

This DAC provides a 16-bit parallel interface and comes with 16-bit built-in double-buffered latches, an amplifier to adjust the gain of the output and a laser trimmed 10 V reference zener diode. The digital interface threshold is 1.4 V and is connected to the DSP microprocessor 5 V logic Data Bus. The analog supply of the DAC is powered with +/- 12 V power supply and the output can swing from +0 – 10 V or +/- 10V. In our application, depending on the FFP-TF used, output voltage ranges 0-6V, 0-7V, 0-10V and 0-11V are utilized. A built-in Op-Amp provides a 10 uS settling time to ½ Low significant Bit (LSB). This 16-bit DAC with the unipolar span of 0 - 10V has a resolution (LSB) of $10V/2^{16}$ = 153 μV, which gives an accuracy of 1.31 pm (60nm / (7V /153 μV) = 1.31pm) for an FFP-TF with 60nm FSR and 0 – 7 V span.

The DAC output pin is placed closer to the FFP-TF input pin on the PCB to avoid loss of resolution due to voltage drop across the trace length. In addition, trace width is kept large to reduce the trace resistance. If the voltage drop on the trace is 153 μV, it will

produce an error of 1 LSB in the FFP-TF offset. The analog and digital portion of the DAC is routed separately to minimize the induced interference by the digital lines on the analog section. The bypass de-coupling capacitors of 0.1 μF are connected close to the power pins to bypass the high frequency noise on the power lines to ground. Separate Analog Ground (AGND) Plane and Digital Ground Plane are provided and interconnected at the DAC.

5.10 Optical switch implementation

On the single-board microprocessor-based FBGI design , the number of FBGs that can be inscribed on a single-channel fiber is limited due to the spectral bandwidth of the system, which is determined by the bandwidth of the broadband source of light, material characteristics of optical components, bandwidth of the interrogation system and the like.

Though FBGs can be made to cover each spectral chip in the full spectrum, commercially available components impose the above-said limitations. For instance, the FBG sensors are usually fabricated to have their Bragg wavelengths in "C" band, though ASE source and EDFA amplification have a span to cover both C and L bands. This is again due to the spectral bandwidth limits of the optical components. In addition "C" band is selected as the operating band in order to reduce the overall system cost by making use of the widely available optical components. The requirement of non-overlapping FBG spectral chips during the perturbations imposes another limitation; if the reflected spectral chips overlap, it would be another tedious task to differentiate them [20]. However, with the

successful research in CDMA technology in FBG sensor network technology, it is feasible to allow the reflected spectrum to overlap [62] [63]. The implementation of the optical switching technique into the FBGI system makes a great difference in the optical performance monitoring. This effectively reduces the cost by utilizing the same interrogation system for multiple sensor channels. The incorporation of optical switch and the optical switching technique utilizes all the three technologies, namely: Space Division Multiplexing (SDM), Time Division Multiplexing (TDM) and WDM network together [20]. In this configuration, each fiber channel is allotted a numbered scanning time slot and all the channels share the same transmission path and the same interrogation system [20]. The scanning works like a polling software mechanism. Since the system works like a polling technique, it is not a true TDM network. The real-time data is lost during the waiting intervals. This is an inherent drawback of the scanning technique.

By improving the scanning speed and sticking to Nyquist sampling theorem sampling, the sampling accuracy can be improved. A better way would be to use CCD (Charged Couple Devices) devices to detect the reflected spectrum in parallel without loss of real-time data. The usage of an optical switching technique makes use of the full spectral bandwidth of the FBGI system for each channel. However, this is achieved at the expense of the overall sampling speed per channel. In general, the commercial FBGI systems provide an option to increase the fiber channel by way of splitting the available total spectral bandwidth among the channels.

5.10.1 A 2x2 electro-optical switch

Among other optical switch manufacturers, O-Net and Agiltron are two manufacturers who provide optical switches suitable for our FBGI applications. O-Net [64] FOSW 2x2 Optical Switches use Opto-Mechanical technology and utilize internal electrical driving coils to control the switch operation. With the FFP-TF scanning speed of 50Hz (20ms), the best switching time between the two switching actions is 20ms. By taking into account the inherent switching time of the internal coils, we can calculate the switching period as T = 2 x (8 + 20) = 56ms. This results in the effective multi-channel scanning speed of $f_{effective} = \frac{1}{T} = 17.857Hz$.

Though by implementing higher order optical switches, we can increase the number of channels that can be multiplexed, it is achieved at the cost of switching speed and loss of spectral information. Hence, it is best to strike a balance between the number of channels, the order of the optical switch and the quasi-static nature of the signal sensed.

5.11 Summary

Different approaches have been taken to design a successful compact FBGI system using FFP-TF. As the first step, efforts were taken to design a compact single-channel FBGI system using FFP-TF. To overcome the defects of the single channel system, a second system was developed to make use of the DAQ card and the optical switch for multi-channel quasi-distributed sensing.

The FBGI system was divided into an interrogation subsystem and PC-based control subsystem. The FBGI interrogation subsystem consisted of mainly a combined optical source and an amplifier module, the key tuning element FFP-TF unit, an integrated receiver circuit and a microprocessor-based digital circuit with ADC and DAC. An ASE spectrum was used as the light source to launch light into FBG array which then reflected selected wavelengths. The configuration of using the ASE source also as the EDFA reduced the system cost and size, but at the expense of signal to noise ratio due to the ASE background noise. The transformed signals were processed by the PC-based software and interpreted into strain information on graphical user interface for the users.

An EDF was used to construct the ASE source and the amplifier. Co-directional and counter-directional pumping effects were tested. The optimal length of an EDFA was selected to achieve more flattened gain of the ASE spectrum. Noise and Gain profiles of EDFA and ASE were measured. Experiments were conducted to better understand the FFP-TF characteristics. Current controller and temperature controllers were used to provide a continuous and stable output from the laser-pump. An optical receiver circuit was designed using an InGaAs pin PD and an op-amp OP07. A Sallen-key Filter was designed to properly filter the out of band noise before feeding the detector output to the ADC. Finally the implementation of an optical switch was discussed.

Successful FBGI-System design took us to the next stage of system integration.

Chapter 6

System Integration and Analysis

In this chapter the system integration of the FBGI system design and a case study analysis of DFBGs for a sleep monitoring system are studied. The FBGI system integration is a challenge. New approaches and techniques are taken to solve the problems found during system integration. This chapter discusses the different challenges taken to integrate the FBGI system. The FBGI system is demonstrated for its capability of scanning a FBG sensor array. The advantages and limitations of the FBGI system are analyzed.

6.1 Introduction

The FBG interrogation systems developed use an Amplified Spontaneous Emission (ASE) source as the broadband light source and an Erbium Doped Fiber Amplifier (EDFA) as the amplifier. This ASE, EDFA combination makes the system performance stable and superior to systems that deploy other light sources. Automatic scanning of a multi-channel FBG sensor array is feasible with a Fiber Fabry-Perot Tunable Filter and an optical switch technology. Any change in wavelengths due to pressure or temperature is captured by the tunable filter and an optical receiver and then sampled by the built-in ADC on board or by the Data Acquisition (DAQ) card. This data is processed and then displayed on a computer screen.

During system integration, DFBG network is first analyzed using an OSA. A broadband light source is used in order to analyze the reflected spectrum of the Bragg wavelengths in the DFBG network. The outgoing light is transmitted to the fiber.

As shown in Figure 6-1, the reflected wavelengths are re-directed to the optical spectrum analyzer (OSA) via a circulator, in order to characterize the reflected spectrum of the DFBG network.

When the sensors are connected in series, it is necessary to make sure that the spectrum of the broadband light covers all the Bragg wavelengths in both strained and unstrained conditions. In addition, Bragg gratings are inscribed and or embedded in such a way that they do not overlap with one another when they experience strain or compression. Typically, Bragg gratings are inscribed in series such that the distance between two wavelengths when not stressed is around 2.4nm [42].

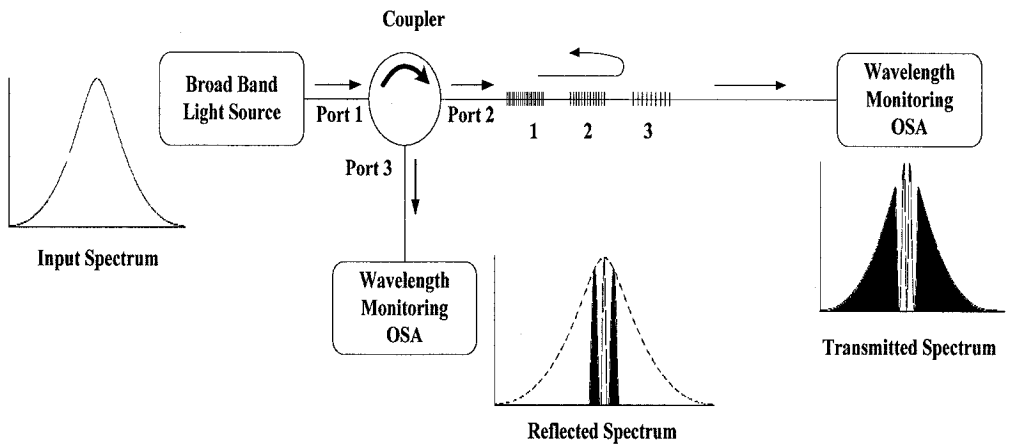

Figure 6-1 Measurement of reflected wavelengths of a DFBG sensor network using a broadband source and an optical spectrum analyzer.

6.1 System integration

First each individual module design is constructed and tested. Then the whole FBGI system is assembled together with the optical circuit. Extensive integration tests are done with the PC-based software and other test equipment. Problems found consist of but are not limited to the insufficient light intensity from SLED light source, the non linear characteristics of FFP-TF response and the scanning speed of the FFP-TF control, a steep hump in the EDFA gain profile, noise filtering of input to ADC, saturation of the optical receiver circuit, thermal runaway of LD current driver and the laser pump, low interrogation speed and a poor user interface. As a result, efforts are taken to solve the challenges faced and recommendations are made for future improvements.

6.1.1 SLED light source

The original design uses 1550nm wideband SLED as the broadband light source to the FBG network. Since the output power intensity of the SLED 7mW is not sufficient, an ASE spectrum from an EDF pumped using a 980nm laser with 200 mW output power rating is used as the light source.

6.1.2 FFP-TF control

The FFP-TF response test served the purpose of verifying the linear relationship and the hysterisis behavior between the filter peak wavelength and the tuning voltage. However, no steps are taken to rectify or compensate the hysterisis behavior of the FFP-TF. The test resolution is limited by the resolution of the tunable power supply and the manual

control. For accurate FFP-TF control, a reference wavelength cell can be used to calibrate the FFP-TF response for improved accuracy [43]. A look-up table inside the software along with the tracking direction control can also be used to compensate for the FFP-TF hysterisis behavior. The results show that FFP-TF response is actually nonlinear, but it can be approximated as many linear segments. The more the linear segments used for approximation, the higher the accuracy is, but requires a complicated algorithm for the FFP-TF control.

6.1.3 EDFA gain flattening

Due to the unflattened EDFA gain profile especially at 1530nm region, the amplification of the reflected signal is high and results in the op-amp saturation for wavelengths around 1530nm region. The FBG signal amplitudes amplified by EDFA in the 1530nm region are clipped by the Op-Amp in the optical receiver circuit. Although this gain saturation can be removed by reducing the gain of the Op-Amp, this gain renders some of the FBG signals in the 1570nm region undetectable due to their small signal amplitudes falling below the peak detection threshold set in the software algorithm. The usable spectrum is narrower, if the peak signal amplitudes in the 1570nm region are undetectable. This problem is addressed during the design by gain flattening through adjusting the EDF length and the laser pump power. Gain flattening the EDF widens the usable spectral range of the FBGI system from 45nm (1535nm to 1580nm) to 60nm (1520nm to 1580nm). Another way is to reduce the op-amp gain and increase the reflectivity of each

FBG sensor by increasing the length of the FBG during inscribing. For 1570nm FBG signals with small amplitude, increasing the reflectivity of the FBG could increase the reflected signal amplitude. Automatic gain control of the op-amp gain is another feasible solution. In addition, gain of the Op-amp can be reduced and a dynamic threshold level can be implemented in the peak detection algorithm.

6.1.4 Adjustments to optical receivers

First of all, the idea of using a PIN-TIA module is abandoned since they are AC coupled devices specifically used in telecommunications and the DC offset is high (though many have DC offset control). In an FBGI system, useful information is contained in the DC signal. In addition, the cost of PIN-TIA module is prohibitive for our FBGI sensor application compared to that of a PD and an op-amp acting as a high impedance amplifier or a TIA. Hence, a PIN-TIA is not used. An integrated receiver module consisting of a PD, an Op-amp and a Sallen-Key LPF is constructed as part of Optical-to-Electrical conversion and signal amplification.

6.1.5 Interrogation speed

The interrogation speed is limited. Although modifications to the FBGI subsystem are made, the interrogation speed is still low. In the single-board microprocessor system, the overall interrogation speed is low mainly due to and not limited to the serial communication between the PC and the single-board system to control the FFP-TF via DAC and to analyze the data from the microprocessor which leads to a much lower

tuning speed (lower than 100 Hz) of FFP-TF . The DAQ Card is used to replace the microprocessor circuit to improve the interrogation speed and to implement a USB communication to the PC. This method is still not successful since readings from the DAQ Card sent to the PC for analyses and control signals sent from the PC to the DAQ Card introduce timing delays due to communication. To improve the overall system speed, steps are taken in software to reduce the waiting time between communication and the looping periods if there are any implemented in the software. The total interrogation speed is increased to nearly 1 Hz (with DAQ). The fine and coarse sampling software technique that is implemented to better optimize the tuning speed and the tuning resolution of the FFP-TF as well contributed to a lower interrogation speed. A better way of improving the system speed is to use a single-board microprocessor system with a powerful microprocessor with on-board controls and display such that there is no dependency on a PC during signal interrogation and processing.

6.1.6 User interface

Efforts are taken to improve the user interface, which could display the spectrum, wavelength shifts of the FBGs and also the pressure-bar views. User interfaces designed with VEE and Visual Basic are later replaced by a user interface designed using LABVIEW. The user interface designed also provides Ethernet communication for sending data to another PC. Figure 6-2 shows the user interface with the ASE spectrum and the sensor positions of a multi-channel DFBG patient monitoring system.

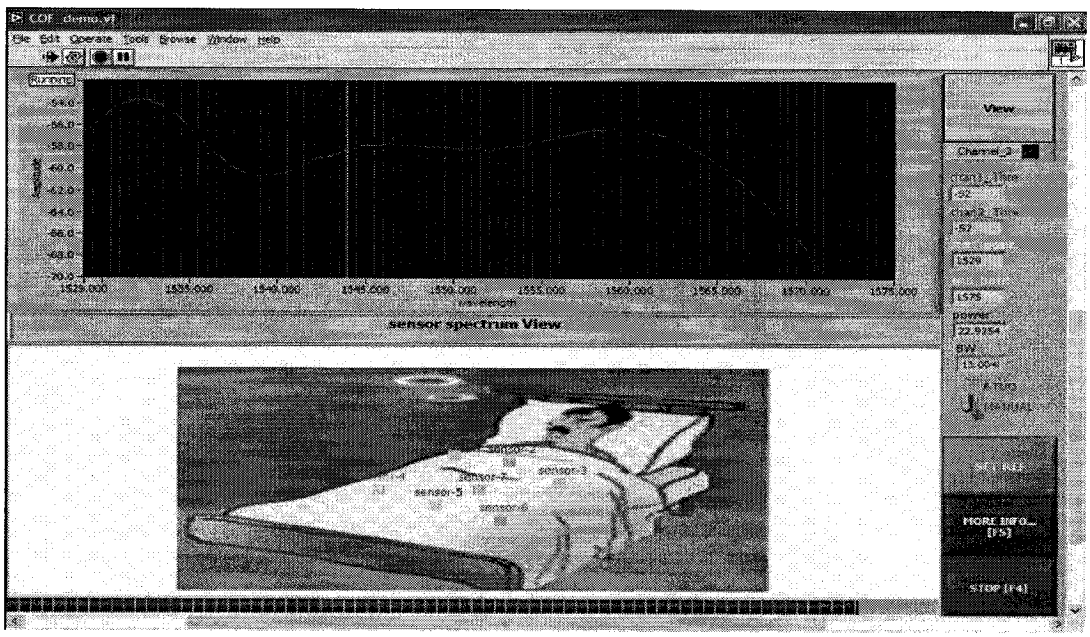

Figure 6-2 User interface of a multi-channel DFBG system showing an ASE spectrum [44].

6.1.7 Sleep monitoring FBG sensor

In this case study, FBG sensors are used to monitor the sleeping patterns of subjects based on wavelength shifts due to pressure.

Bedsores, also known as decubitus sores or pressure sores, frequently develop on patients confined to bed who are, in general, unable to move for a long period of time, such as patients with paralyzed spinal cord injury or patients recovering from surgical operation.

For patients vulnerable to developing bedsores, special attention should be paid to areas of bony prominences [45], e.g. areas such as the hipbones, tailbone, ankles, buttocks, etc. Once deep bedsores develop, they are difficult to treat and they are often very slow to heal [46] [47] [48]. A bedsore develops when blood circulation to the skin is cut off for more than two to three hours. Hence, the immobile patients should be moved quite frequently at a frequency of less than two hours [45] [47]. As the skin dies, the skin will show as a red or pink, painful area. If not treated, the skin can break and will grow into open wounds. A bedsore can easily get infected and become larger and spread deep into the muscle. Deep bedsores will cause severe medical problems such as bone and blood infections, and scar cancer (scar carcinoma) may develop and may even lead to the patient's death [45] [47] [49]. The best way to avoid bedsores and the severe complications associated with them is by advance protection of the skin [45].

A bed with an intelligent dynamic support surface would help to move a patient's body from time to time at a programmable interval. However, such beds would be required in large quantities, are costly and once programmed, the surfaces will move even if not required. Prior studies [45] [50] show dynamic surfaces are effective in preventing bedsore development. Further improvement can be done to the dynamic surfaces to make them smart by incorporating our DFBG network into the dynamic surfaces, though it will be at an increased cost. DFBG networks can be implemented into the static beds to prevent bedsore development as an inexpensive solution compared to the dynamic surfaces.

A better theory would be to have a monitoring system that can constantly monitor the movements of the bony prominence areas by sensing the dynamics of the pressure inserted by these bony prominence areas on the bed or on the mattress, and thus the patient's sleeping pattern. The monitoring system would give the information related to each bony prominence area and thus could alert the surveillance system, a nurse can activate and control the dynamic support surfaces to move the patient's body. A fuzzy-logic algorithm can be developed to display the motion of the bony-prominence areas on a display.

In our monitoring system, FBG fiber optics sensors, and the interrogation system are employed to monitor the patient's movement and to alert the hospital staff and thus to stop bed sore development. This is possible with the greater sensitivity and the larger dynamic range the FBG sensors exhibited. The FBG sensors are made to the required sizes and configurations during the FBG inscribing and embedding process and then connected in serial and or multiplex configurations to cover a large measuring area. An FBG sensor has the great advantage of eliminating the hazards of electric shock. FBG sensing fiber-reinforced carbon elements will not be affected when in contact with water or urine (except they would sense slight temperature variation) and thus would not agitate normal activities of sleep [46].

6.1.7.1 Bed-bound patient and FBG sensor positions

In order to layout the FBG sensors such that the sensors are sensitive to the movement of the bed-bound patient, the bony prominence area of a bed-bound patient is studied and the FBG sensors are layout accordingly. The position lying flat on the back as shown in Figure 6-3 (a) results in the body mass resting on the bony prominence of the sacrum or coccyx and heels. The side view position shows that the body mass is resting on the bony prominence of the hips and "lateral malleoli" of the ankles [50]. To monitor the movement of different pressure points, 7 FBGs of different wavelengths are inscribed in series on a single SM fiber and placed below the different bony prominent points of the body. These 7 embedded FBGs are located as shown in Figure 6-3(b) such that FBGs are sensitive to movement of the bony prominence spots of the bed-bound patient. The FBG modules S1, S2, S6 and S7 are placed such that they cover the inner and outer ankles. The length of the carbon composite of each sensor S1, S2, S6 and S7 is 4 cm. The FBG modules S4, S5 and S6 are located such that they cover each side of the hipbones and the tailbone. The length of the carbon composite of each sensor S4, S5 and S6 is 6 cm. The fiber-reinforced carbon sensors are made smaller in size for ankles as ankles have smaller surface area compared to that of the hipbones and tailbone sections. However, the same width of 5mm is maintained for all the sensors.

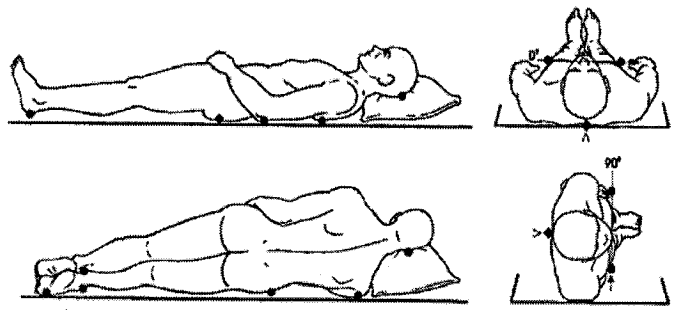

(a)

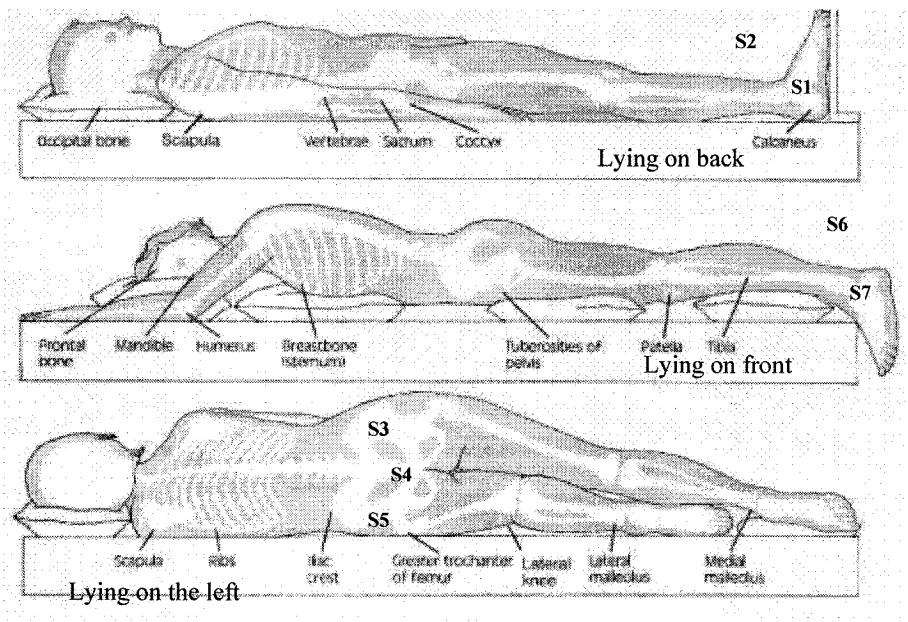

Sensor Positions:

S1. Outer right ankle
S2. Inner right ankle
S3. Right hipbones
S4. Tailbones
S5. Left hipbones
S6. Inner left ankle
S7. Outer left ankle

(b)

Figure 6-3 (a) Positions of the bed-bound patient [50] (b) FBG Sensor positions on a bed-bound patient [20].

In order to increase the sensitivity to pressure and to facilitate single point bending, all the 7 FBGs are embedded in arc shapes. In addition, all the FBGs are embedded in carbon laminar in the 0/FBG/0/0/0 configuration. The calibration graph for one of the 7 FBG sensors is shown in Figure. 6-4. The square of the correlation coefficient between wavelength shift and applied force is around 0.9997.

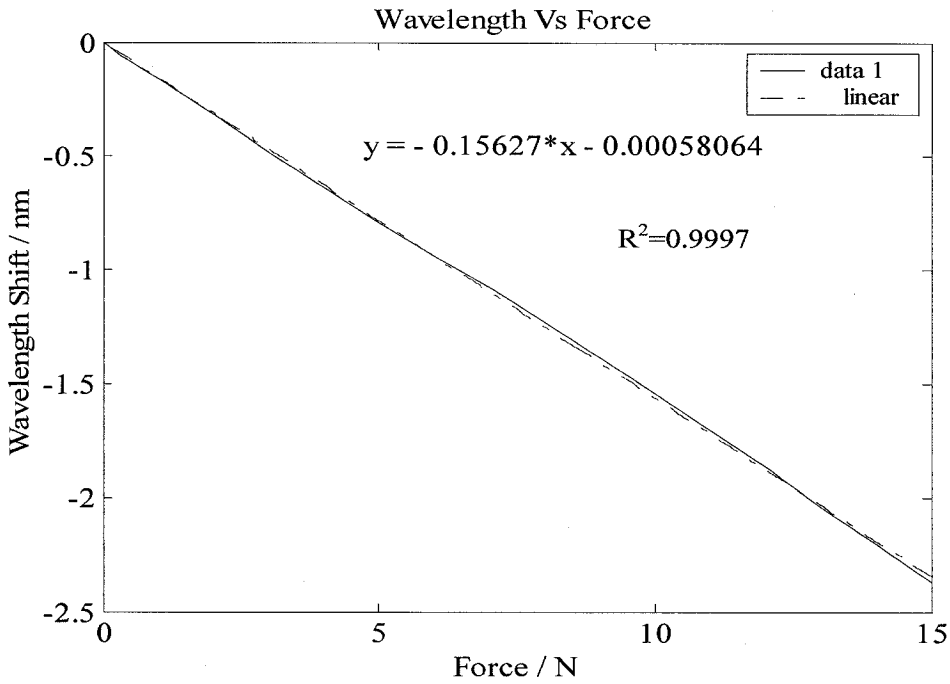

Figure 6-4 Wavelength Shift vs. Force characterization of an FBG sensor used in the sleeping pattern monitoring.

The reflection spectrum of these 7 FGBs is shown in Figure 6-5. Under no-load condition, the Bragg wavelengths of the fiber-reinforced carbon composites FBG sensors S1 to S7 are 1537.211nm, 1544.623nm, 1548.098nm, 1553.166nm, 1557.576nm,

1563.045nm and 1569.002nm respectively. Care is taken while inscribing to ensure that the wavelengths will not overlap one another under strain or unstrained conditions.

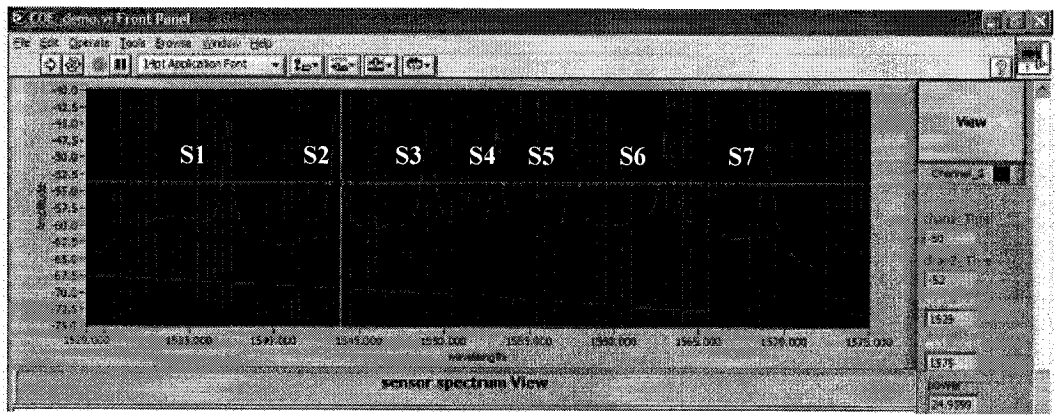

Figure 6-5 Reflection spectrum from the DFBG sensor network used for patient monitoring [20].

6.1.7.2 An experimental setup

It is ideal if the sensors can be attached to the patient's body directly such that the sensors are always in contact with the bony-prominence areas of the patient. Figure 6-6 shows an interrogation system interface to patient sensors. However, this method has a serious drawback in that it is not possible to attach the quite hard fiber-reinforced carbon sensors directly to the patient's body as the fiber-reinforced carbon composites can simply scratch the body and even damage the weakened skin.

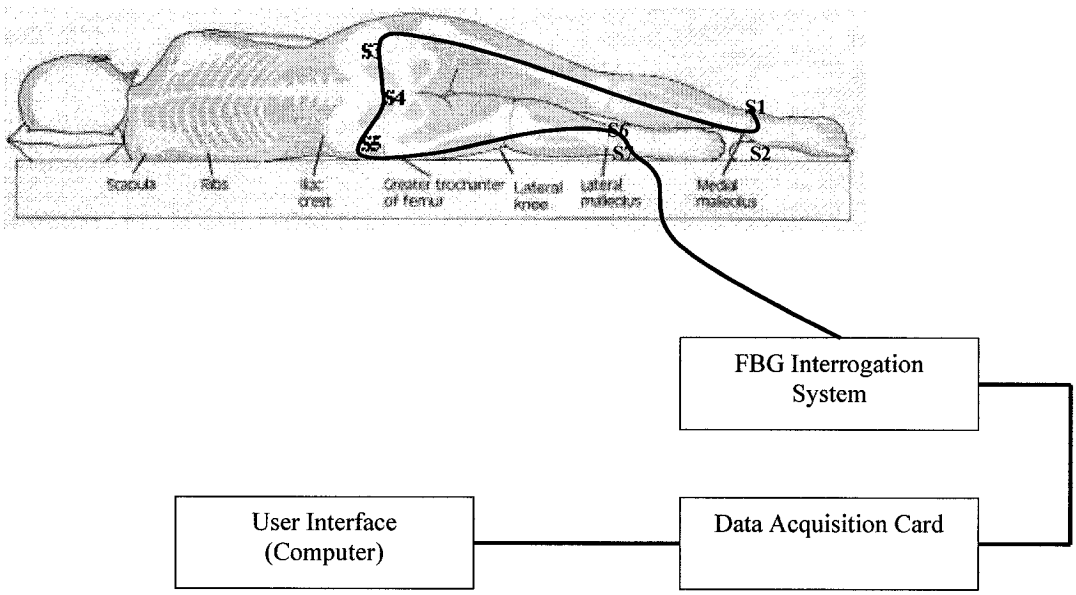

Figure 6-6 Bed-bound patient monitoring. An experimental setup [20].

There are two solutions proposed for mounting the sensors to monitor sleeping patterns of bed-bound patients. As shown in Figure 6-7, by locating the sensors on the hospital pants the sensors are made wearable in the first solution. This configuration does not work well. Pressure is not always inserted on the sensors as the sensors on the pants are quite often freely moving and not in contact with the bony prominence areas.

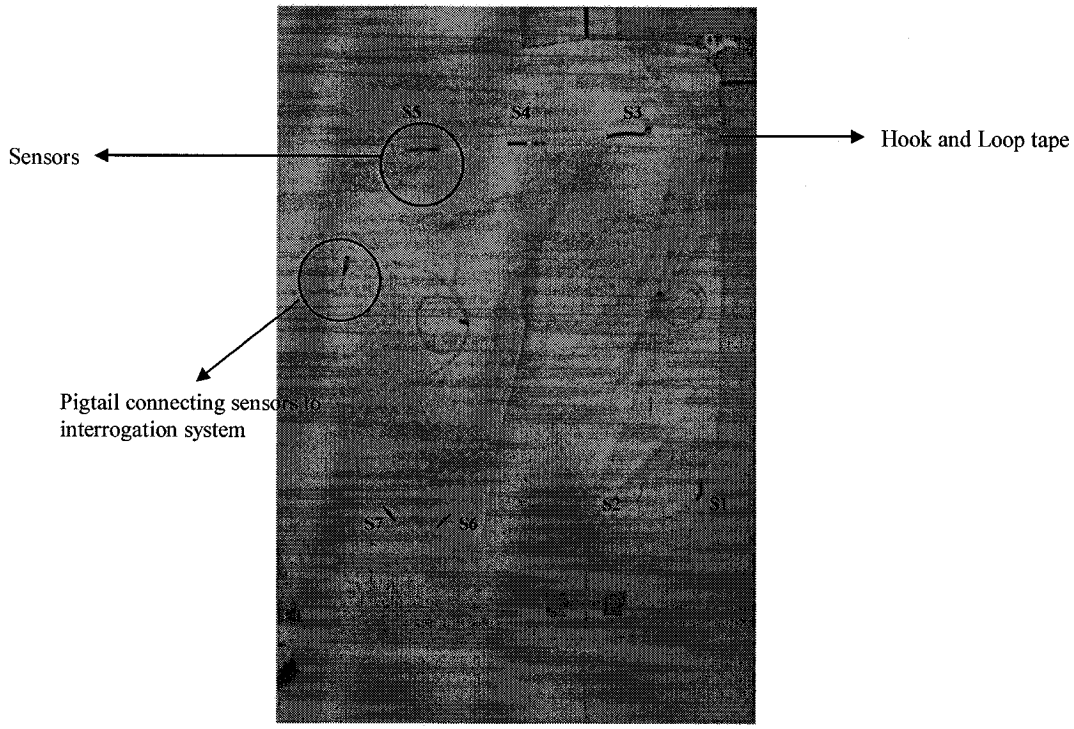

Figure 6-7 FBG Sensors attached to the back of hospital pants to match the configuration shown in Figure 6-6 [20]. Figure shows a pigtail connection from the FBG network that can be connected to the remote interrogation system.

In the second solution, all the sensors are placed on the hard surface below the mattress as shown in Figure 6-8 and Figure 6-9. This solution is the best as each sensor element can sense the dynamics of a larger area around each location. Figure 6-9 shows the complete interrogation system with sensors placed on the bed. This configuration is used in the lab to take the measurements as shown in Figure 6-10.

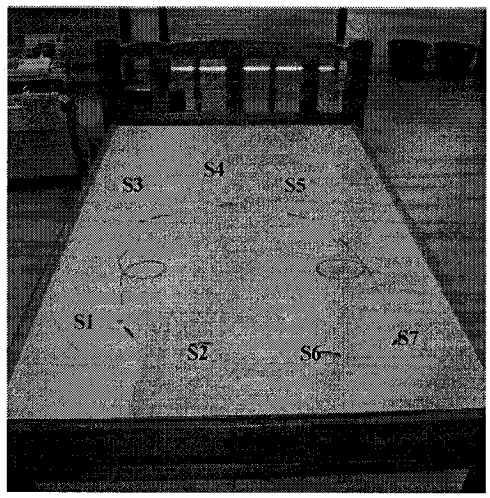

Figure 6-8 FBG sensors located onto bed-board to match the configuration shown in Figure 6-6 [20]. Figure shows a pigtail connecting the FBG network to the remote interrogation system.

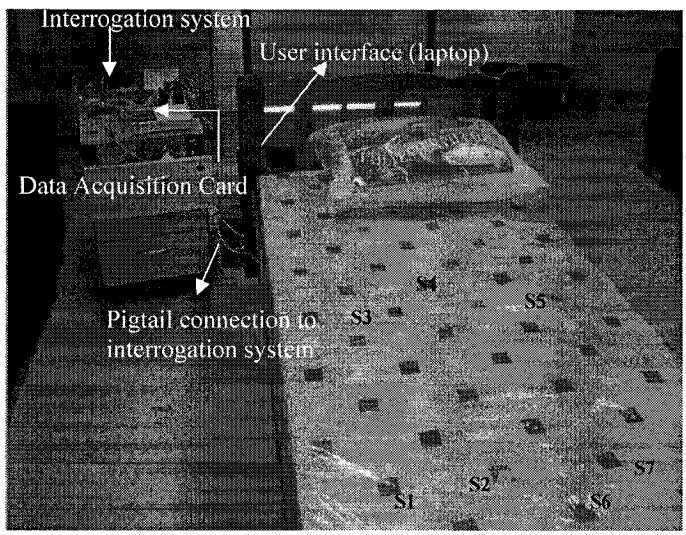

Figure 6-9 FBG sensors are located below the mattress on a bed board to match the configuration shown in Figure 6-6 [20]. Figure shows the remote interrogation system with Data Acquisition Card and a user interface (laptop) where the control resides and the data is processed and displayed [20].

In both techniques, sensors will show different wavelengths shift when there is a change in the sleeping posture. Figure 6-10 shows the results of a test that is conducted for 350 seconds to monitor the motion of a 22-year-old female weighing 45 kg. When a particular wavelength remains constant versus time, it indicates no motion of the body around the surroundings of the particular sensor associated with that wavelength. If the wavelength remains constant for an excessively longer period of time (which is set through the user interface at the step of 5 minutes), it is used as an alarm condition. An automatic alarm is generated so that nurses or doctors can visually inspect the graph and take action manually.

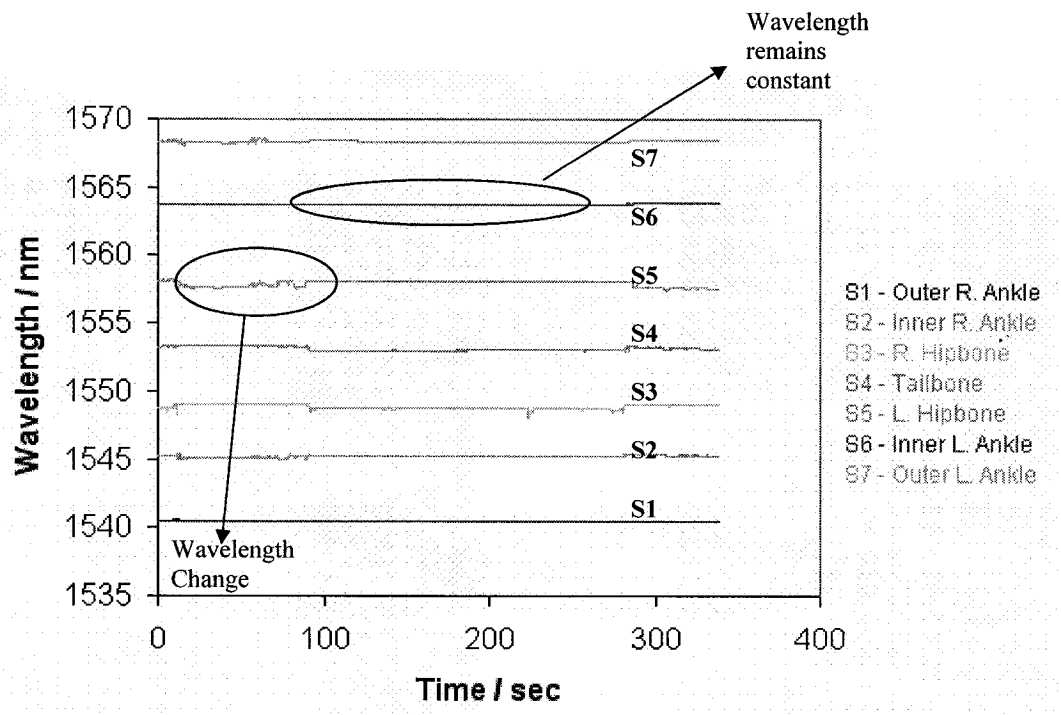

Figure 6-10 Wavelengths vs. time for all the 7 FBG sensors [20].

The variation of pressure on each sensor is dynamically monitored on a pressure bar view. Figure 6-11 shows the monitored wavelength shifts for pressure variations as the Pressure-Bar View. In addition, the Pressure variations at the Pressure points are shown as color variations on the Body View. Since the FBGs are embedded above the neutral layer, when a downward pressure is applied, the sensors experience compression and thus show a blue shift in the reflected wavelength. When pressure increases, to indicate the changes as compression the pressure bars will shrink to the left. When the pressure is released, the pressure bar will return to the relaxed position. Since the applied pressure is linearly proportional to the wavelength shift, the dynamics of the movement of the patient can be easily tracked.

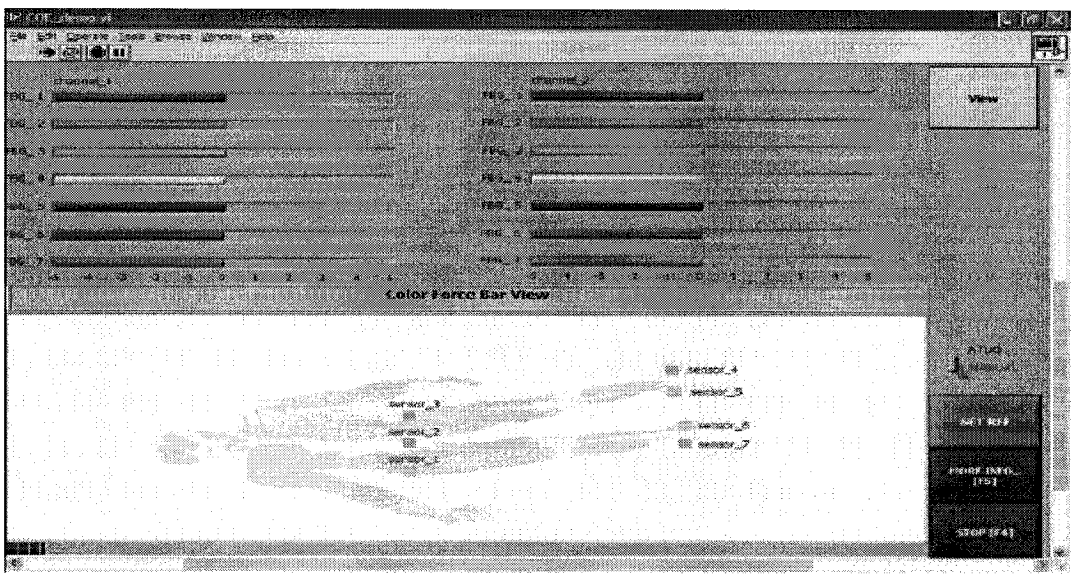

Figure 6-11 Pressure-bar view and body view of patient monitoring system, displayed by LABVIEW interface [20].

6.2 Advantages and limitations

Though a number of challenges faced during system integration are resolved, there are still some improvements that can be made to achieve high performance and to meet commercial market needs. The advantages and limitations of our developed FBGI systems are studied and compared with some commercialized systems below.

6.2.1 Multi-channel scanning capability

Incorporating the optical switching technology brings great enhancement to the FBGI system and it is a milestone in FBGI development at NTU/Singapore. Multiple fibers with FBG sensors inscribed in series are connected to different output ports of the optical switch. This configuration brings in the multi-channel scanning capability to the FBGI system. By implementing an optical switch, the scan-able spectral range per channel still remains as the full spectral bandwidth of the input light source or that of the tunable filter, whichever is the smallest. Total cost per system is reduced as multiple-channel FBGI system reduces the number of single-channel FBGI systems otherwise required to monitor the multiple sensor points. In general, the commercialized FBGI systems, in order to achieve multi-channel scanning capability, divide the full spectral range into several smaller sections and allocate each of the smaller sections into different channels. This method has the drawback of effectively reducing the number of FBGs that can be used per channel.

6.2.2 Low system cost

The total system cost is less than US$10,000, which is much less than the commercialized single-channel FBGI systems. For instance, the cost of the single channel MOI FBGI system SI425 made by Micron Optics, with limited graphical user interface and limited functionalities, is around US$32,000. The cost is even higher if the system comes with the multi-channel upgrade option. If our FBGI system is commercialized for mass production, the system cost will be further reduced.

6.2.3 Low weight and compact size

Most commercialized FBGI systems are meant to be desktop systems and are bulky and heavy and they are not designed for portable applications. In contrast, our FBGI system is compact and portable. If the design is targeted for mass production, the single-board design can be further reduced in size by using multi-layer layout and ball grid array components technology.

6.2.4 User-friendly interface and multiple software functions

In general, at the time of this analysis, most of the commercialized software for the FBGI systems only displays the peak wavelengths of the reflected signals of FBG sensors. The improved graphical user interface of the FBGI system takes into account the end-user

needs and offers different viewing options such as the peak wavelengths, wavelength shifts, spectrums, the pressure-bar view, strain view, temperature view and the like. A fuzzy logic algorithm is being developed to display the patient's movements from the information encoded in the wavelength shifts. All these end-user graphical user interface features eliminate the trouble of raw wavelength data analysis, which can only be understood by fiber experts. Software also has the feature of date stamping and logging the measurement data at different time intervals. Remote access of the measured/stored data is made possible through the ethernet such that data can be retrieved remotely for further analysis [46].

6.2.5 Low interrogation speed

With all the improvements, the interrogation speed of our system is low and less than 1 Hz. The average speed of most commercialized FBGI systems is around 0.5 - 250 Hz [51]. Although our system meets the speed requirement of many sensor applications, it has the obvious drawback of speed limitation, compared to that of the commercially available FBGI systems. To improve the speed, a future plan is to use DSP-processors and high speed on-board embedded micro-processors to analyze the signals and interface with the end-user.

6.2.6 Poor accuracy

Many factors contribute to the accuracy of the system. Tuning speed of FFP-TF, the hysterisis characteristics of the FFP-TF, resolution of the DAC used to control the FFP-TF, ADC used to measure the detected voltage of PD-Amplifier circuit, and tolerances of each component are some of the factors contributing to the system accuracy. However, since the final data processing is based on the relative wavelengths shifts and not on the absolute wavelengths, the resolution of the interrogation is higher and the errors contributed by the system tolerances are cancelled. A 16-bit DAC is used to control the ~60nm FSR FFP-TF at a step of 32 counts, which yields an accuracy of around 30pm. Around ~1pm accuracy can be achieved with a step of 1 count. Commercialized systems are available with accuracy of 0.2- 6 pm. (with aging, considering long-term use accuracy of 2- 6 pm) [51].

6.3 Summary

New approaches and techniques were taken to solve the problems found during the system integration test for further improvements. Its advantages and limitations were analyzed. Since the Bragg gratings were inscribed in series such that the distance between two wavelengths when not stressed is around 2.4nm, the wavelengths did not overlap under stress or stress-free conditions. Problems found included the FFP-TF control, a steep hump in the EDFA gain profile, saturation of the optical receiver, low interrogation speed and a poor user interface. Though FFP-TF characteristics were verified and

methods were suggested to overcome the shortcomings of the FFP-TF response, no steps were taken in this design to rectify or compensate the hysterisis behavior of the FFP-TF.

Due to the unflattened EDFA gain profile, especially at 1530nm region, the amplification of the reflected signal was high and resulted in the op-amp saturation for wavelengths around 1530nm region. This way the problem was addressed during the design by gain flattening through adjusting the EDF length and the laser pump power.

The idea of using an off-the-shelf PIN-TIA module as the optical receiver was abandoned due to its inappropriateness for our analog design. The interrogation speed was found to be still low at about 1Hz.

The user interface was improved by using LABVIEW software, which could display the spectrum, wavelength shifts of the FBGs and also the pressure-bar views. The interface designed also provided functions like saving measured data and sending data via the ethernet. A case study on FBG Sensors for Sleep Monitoring [20] was successfully analyzed and conducted using 7 FBG sensors on a network to monitor the sleeping patterns of patients based on wavelength shifts due to pressure.

Chapter 7

Conclusions and Future Work

7.1 Conclusions

The objectives of this thesis are to design and develop an FBGI instrumentation system using an FFP-TF to monitor the reflected wavelength shifts from a Distributed Fiber Bragg Grating (DFBG) network and to interpret those wavelengths shifts into environmental temperature, strain and pressure variations. With large amount of research and systematic work, we have designed and built the FBGI system successfully. The peak wavelengths shifts were interpreted into strain, pressure and temperature information. We have designed and demonstrated a single channel FBGI system and a multi (dual)-channel FBGI system successfully. We have conducted numerous research works during this thesis on a variety of topics and employed new methods to improve different aspects of the design. New methods were employed in FBG inscribing and embedding, hardware design and in software algorithms. In addition, recommendations were discussed throughout the design process to enhance the performance in the future.

In Chapter 1, an introduction to the overall research, the scope and the objectives of the thesis were presented. The major contributions were also briefly captured as well as an explanation of how the thesis is organized.

In Chapter 2, the theory behind FBG structure was discussed and the equations for strain, temperature and pressure sensitivities were given as well as the relationship of peak reflectivity to length of FBG and the equations for the bandwidth of the reflected spectrum.

In Chapter 3, different application areas of FBG and the theory models of different FBG interrogation technologies were discussed and their relevance to our FBGI system design was established. We highlighted the efficiency of parallel detection and described the influence of temperature over strain sensing.

In Chapter 4, we presented the embedding techniques in detail. We fabricated the FBGs using phase masked technique and the FBGs were embedded in carbon composites. The effects of FBG embedding in different configurations also were analyzed. We presented the approach of neutral layer embedding for temperature compensation during strain sensing, and experimented with wavelength shifts caused by strain and temperature effects and presented the results.

In Chapter 5, we described the FBGI system circuit design. Both the electronic circuit and the optical circuit design were described in detail. The architectures of the single-board microprocessor-based interrogation system design and the DAQ Card based interrogation system design were presented. We discussed the different experiments conducted and the results taken during: the 980nm laser pump circuit design, ASE source

design and EDFA design. In addition FFP-TF interrogation and characterization were discussed in detail. We proposed gain flattening for EDFA via different methods and implemented gain flattening by choosing an optimum length of EDF fiber. The design of an optical receiver circuit and the LPF design were also discussed. An optical switch was implemented to add multi channel scanning capability to the FBGI system. The rest of the circuits were also discussed in this chapter.

In Chapter 6, we presented the FBGI system integration efforts and the challenges faced. The FBGI system was demonstrated for its capability to scan an FBG sensor array. The advantages and limitations of the FBGI system were analyzed. In addition, a case study FBG sensor for patient monitoring was presented.

In conclusion, the FFP-TF-based FBGI system was found to be well suited for sensing applications, especially in cases where signals are quasi static in nature. Based on our above research, we will summarize the advantages, existing problems and possible solutions in the following sections for future FBG interrogation system design.

7.2 Advantages of the FBG interrogation

One and probably the most important advantage of the FBG interrogation system is its flexibility to be used in wide applications such as aerospace, telecommunications, defense, civil structures, bio-medical, and chemical engineering. Unlike other sensors,

FBG-based sensing is not affected by light intensity levels. FBG acts as a transducer and transformed information is encoded into wavelength shifts. Though the accuracy depends on the magnitude of the changes produced being measurable, all we needed to know was how to map the wavelength shifts to the sensed perturbations of the environmental parameters. FBG sensors have the added advantage that they are not affected by electromagnetic fields. In addition, they are lightweight and can withstand high temperature.

Another advantage of an FBG sensor is that it exhibits the characteristics of a chip optical filter that filters a single wavelength of information and passes the rest. FBGs are easier to fabricate using a phase mask technique. FBG exhibits an advantage in that it can be used for dynamic as well as quasi-static sensing applications. For dynamic strain sensing, we proposed that the performance of the interrogation system can be improved by parallel detection using array waveguide and photo diode array.

Since the FBGs are easy to embed within materials, the added advantage is that their strength can be easily increased by embedding them into carbon composite materials. By embedding, we have removed the fragile nature of the sensor and increased the linear sensing range and controlled the undesired large value of the thermal expansion coefficient of the bare FBG sensor. In addition, embedding brought an added advantage in that with different embedding configurations we can have FBG modules to exhibit compression, tension or insensitiveness to the same applied force. These attributes of the

embedded FBG module indirectly brought a significant advantage in that the configuration which was insensitive to strain was able to be used as a reference sensor.

The FBG sensor can be used in a wide range of applications, and the wavelength encoded information is independent of light intensity. This brings flexibility to the architecture of the interrogation system. Another advantage is that, FFP-TF-based design was produced at an affordable cost as the signals to be measured were quasi-static in nature. We proposed linear segmentation and a lookup table approach for resolving the non-linear FFP-TF characteristics instead of using costly and complex references for continuous calibration of FFP-TF characteristics.

We proposed the fine and coarse sampling technique to control the tuning speed. This provided the advantage of faster sampling of the useful spectral information and at the same time helped to maintain the average tuning speed of FFP-TF low. We implemented a 16-bit DAC, which enabled finer control on the tuning voltage of the FFP-TF such that ~1pm resolution was detectable.

The 980nm laser pump was stabilized for: i) its center wavelength via an FBG on its pigtail, ii) temperature via a temperature controller and iii) drive current via a current controller. This brought the advantage of consistent performance of the circuit across different environmental conditions. We used an EDF as the light source to the FBG network as well as an amplifier to the reflected spectrum from the FBG network. This

brought additional advantages of cost and space savings. We flattened the gain of the EDFA by adjusting the length rather than using costly GFFs. We used a PD for the optical receiver circuit instead of a costly PIN-TIA module. We implemented a 16-bit ADC, which enabled us to have finer resolution on the LSB of the detected signal.

An optical switch was implemented to increase the detectable FBG channels and still keep full light spectrum available for each channel. This not only provided the advantage of increasing the channels, but helped to increase the number of FBGs in the network.
This multipurpose interrogation instrument brings an invaluable and perhaps the most significant advantage in that it can be used in a variety of applications to monitor their performance. The instrument has been demonstrated for general purpose interrogation such as strain and temperature monitoring and bed-bound bedsore patient monitoring.

7.3 Existing problems and some possible solutions

As a complete interrogation instrument, the FBGI system has some shortcomings due to: i) Characteristics and tolerances of the components ii) Architecture of the design iii) Aging of the components iv) Environmental variances and the like. In addition, errors resulted in the recording of measurements and due to the instruments used. Accuracy of the measurement depends on the accuracy and the resolution of the OSA, oscilloscope and digital pressure gauge, multi-meter and the like used to take the measurements. When an experiment was not completed in one day, the results of the measurements were

affected by the drift due to room temperature and the time factor. During the research process, most of the problematic aspects and shortcomings were discussed and possible solutions proposed if not resolved during this research.

One of the shortcomings was the fragile nature and the sensing range of the fiber. By annealing and embedding, we strengthened the fiber and increased the sensing range to a very good extent. To remove the fast decay of the written gratings on the fiber, we annealed the grating-inscribed fiber at an elevated temperature, which stabilized the optical properties of the FBG. Since the lifetime of the fiber also depends on the amount and depth of the cracks developed on the surface of the optical fiber, we recoated the fiber with acrylate immediately after inscribing it with UV exposure. To increase the linear strength of the bare FBGs, we embedded the bare FBGs between the plies of carbon laminars. We experimented with the effect of aligning the fibers at 0^{o} and 90^{o} orientations and found that, when the grating fiber was oriented as 90^{o}-uni-ply, the grating fiber was completely damaged. When the carbon composite modules were fabricated, the flat shaped sensor showed measurable wavelength shifts to 3-point bending force only. Hence, an arc-shaped sensor was made as it showed significant wavelength shifts to both single point uniform force and 3-point bending force.

During our initial tests of the reflected spectrum from FBG, we observed frequent phenomena of many peaks appearing when a force was applied to the FBG sensor module. To mitigate this problem we used an apodization technique during FBG

inscribing to vary the index profile grating gradually rather than abruptly. Temperature effects on the wavelength shifts were a problem during strain sensing. To eliminate this, we used a temperature compensating composite sensor.

During the design and testing process, accuracy and repeatability of the system were among the major questions. The major problem with FFP-TF was the hysteresis effect and the Finesse effect of the PZT. This was the reason for the nonlinear wavelength response against tuning voltage. If the FFP-TF is still to be used as the interrogation unit, to achieve high accuracy of the scanning results, it requires external wavelength reference for repeated calibration. We did not do the calibration of FFP-TF by using a gas cell or with the reference FBG due to its complexity and cost, but we implemented linear segmentation in software and proposed the look up table method to address the nonlinearity of the FFP-TF.

We used an EDF as the light source and an optical amplifier. This had the undesirable effect of producing ASE as background noise, which in turn reduced the SNR of the reflected signal. Since we are interested in the information encoded in the wavelength shifts only and not on the power intensity levels, theoretically we did not need the gain profile of the EDFA to be flat However, the non uniform ASE spectrum with a steep hump at the 1530nm region, lead to the saturation of the detection circuit. We resolved this problem by gain flattening the EDFA, reducing the gain of the op-amp at the output stage and adjusting the peak detection threshold in the software algorithm.

Another shortcoming was electrical noise on the output of the optical receiver, which caused fluctuation to the input to the ADC. We filtered this noise effectively by implementing a 2^{nd} order Sallen-Key filter at the output of the optical receiver circuit.

Another critical shortcoming of the FFP-TF-based interrogation system is the information loss which occurred during scanning and multiplexing. Only a narrow slice (chip) of information is sampled every time. The information outside of this chip, both in time domain and space domain, is lost. However, by sticking to Nyquist sampling rate, the signals were re-constructed. Hence, FFP-TF-based interrogation system could not be used for dynamic strain sensing. We propose AWG and PD array combination for the detection of signal information more accurately.

The drawback of our single channel system to detect a large number of FBGs in a network was taken care by our multi(dual)-channel system design. The multi(dual)-channel scanning that was implemented by using an optical switch could only connect to two FBG channels with eight to ten FBG sensors on each channel. The number of channels could be increased by using an optical switch with higher order de-multiplexing capability e.g. 1xN cross connects, but this would result in lower interrogation speed of the whole system and lower speed may not be acceptable. We can reach a compromise between the number of channels and the speed of interrogation, which depends on the quasi-static nature of the signal.

Another shortcoming of the FBGI system is poor speed. The first and foremost idea to improve the interrogation speed was to replace the slowest component in the system with a high-speed or superior processing power component. The speed of our interrogation system was slowed down by the signal-processing module. Speed was also affected by serial port communication and PC-based processing. The way of addressing these problems are to use USB port to connect to the PC or to use a powerful processor to process and display data on an internal display. Once we improve the signal processing circuit, improving the interrogation system hardware and optical circuit will show improved performance. One more major problem was system size. Discrete type electrical components were used during system design. The system depended on PC-based software processing and external display. At present, portable applications are impossible due to the size of the instrument. One of the major tasks of future enhancement is to use, a powerful embedded high-speed processor, a Real time Operating systems and a 640x480 pixel resolution Liquid Crystal Displays (LCD) to handle all the processing and display requirements.

7.4 Future work

Future work will focus on resolving the existing problems and adopting novel approaches to improve performance of the FBG interrogation system. FBGI interrogation needs to be improved as a full-fledged interrogation system such that it can be used to measure Optical Signal to Noise Ratio (OSNR), Q-factor, Bit-Error-Rate (BER). If feasible, future

work will extend further to measure Chromatic Dispersion (CD) and Polarization Mode Dispersion (PMD) and will look for new application areas where FBG sensors and FBGI systems can be used. Some of the areas of focus will be on FBGs for Bio-medical instrumentation and Optical performance monitoring (OPM) of the optical networks in the telecommunications industry.

One of the necessary future works to resolve existing problems would be to improve the accuracy of the system. If the FFP-TF is still to be used as the interrogation unit, to achieve high accuracy of the scanning results, it requires external wavelength reference for repeated calibration. A spectrum of evenly spaced wavelength peaks generated by an LED illuminated temperature-stabilized etalon filter can be used as a calibration source [51].

A Gas Cell(CH_4) can also be used as a reference source for calibration by simultaneously sampling the absorption spectrum using the tunable filter [56]. Gas cells are insensitive to temperature changes and this property of the gas cell illiminates the need for temperature control circuit. On the otherhand a Fabry-Perot laser diode with temperature stabilization circuit can also be used as a wavelength reference [57]. Figure 7-1 shows a monitoring system which uses wavelength spectrum with multiple peaks as the wavelength reference.

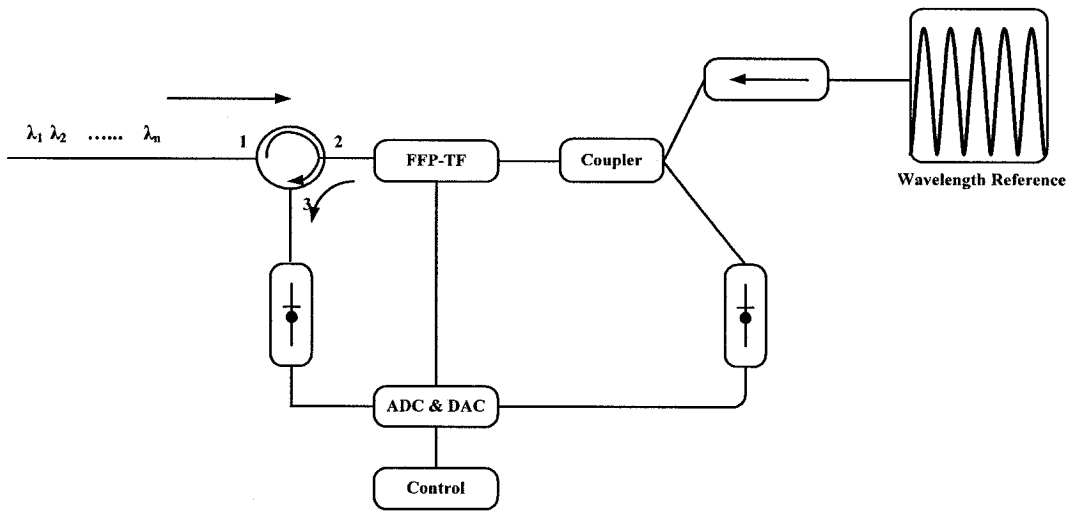

Figure 7-1 FFP-TF calibration via a multi wavelength reference [57].

Another focus area for the future work is to improve the signal conditioning part such as EDFA, FBG reflectivity, Filter design and the like. As such, adaptive gain flattening can be considered for flattening the EDFA gain profile as shown in Figure 7-2. Dynamic gain flattening of the EDFA gain profile is required as the gain profile of the EDFA depends on both the input power and the wavelength of the signal. In dynamic gain flattening, the output wavelength and the output power are tapped and feedback is given to the Dynamic Gain Equalizer (DGE) by a controller such that the DGE maintains a constant EDFA gain across the interested band of wavelengths. An optical performance monitor can be used to monitor the output wavelength and the power.

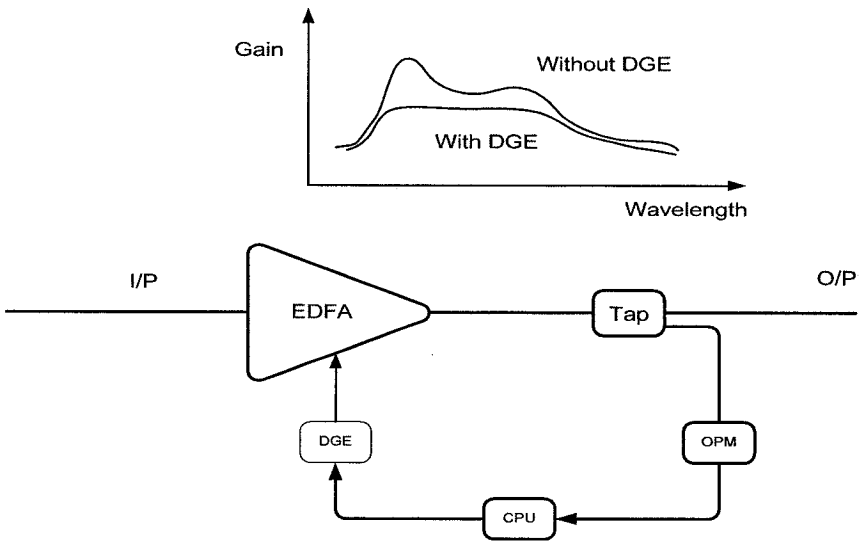

Figure 7-2 Adaptive gain flattening of an EDFA using a dynamic gain equalizer DGE [59].

The Dynamic Gain Equalizer (DGE) is a superior option for dynamically flattening the EDFA gain profile.

In order to improve the speed of the FBGI system, the central processing unit which is a microcontroller ADSP 2181 or a DAQ Card 6015, needs to be replaced with a powerful processor e.g. a DSP processor, OMAP series from Texas instruments. Instead of the FFP-TF-based interrogation, we can use AWG and PD array based interrogation techniques with multiplexing as shown in Figure 7-3. PC-based processing and display of data need to be removed and on-board processing needs to be done and data needs to be displayed on an onboard VGA display.

The fundamental proposal for modifying the interrogation technique is to use light demultiplexing and then use a PD array parallel detection, which would lead to parallel processing. One method is to use a 1xN splitter to split the light into many outputs (Light can still remain broad band) and then use a single filter for each optical output path, as in Figure 7-3. The fastest way is to use AWG (Array Waveguide Grating) to demultiplex the optical wavelengths as shown in Figure 7-4 [3] [13] [14] [15] [22] [55].

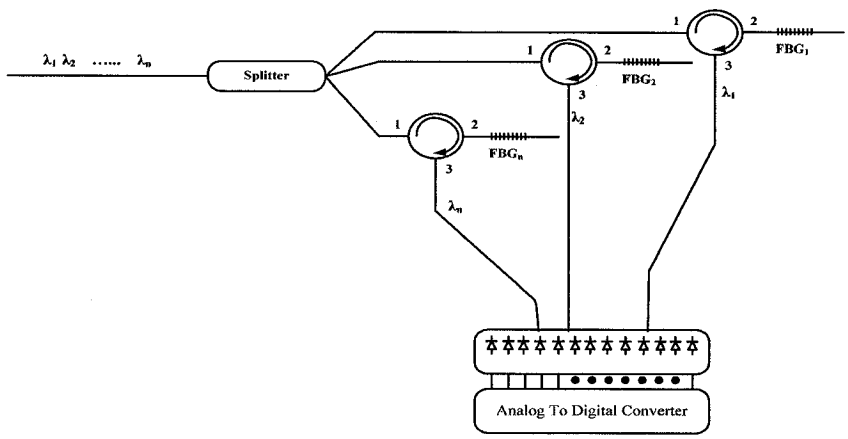

Figure 7-3 FBG Interrogation – Parallel detection using 1xN splitter and a PD array.

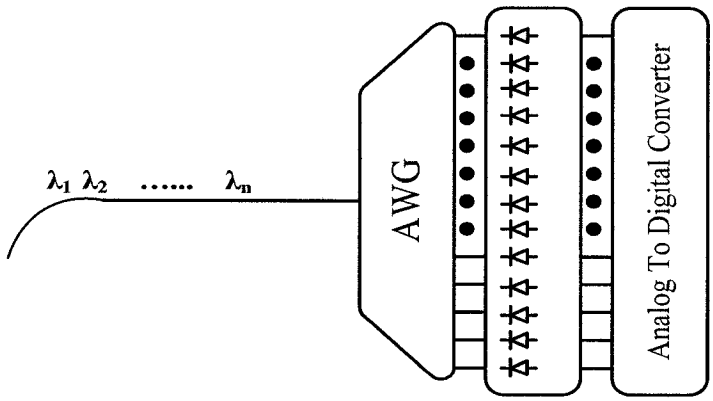

Figure 7-4 FBG Interrogation – Parallel detection using an AWG and PD array.

In future work we can incorporate the CDMA technology for FBG interrogation. In CDMA, a correlation technique is used to separate the reflected sensor signals (CDMA) [62]. Delayed and multiplexed sensor signals are scanned using an electrical scanning technique. The CDMA method can offer stronger sensor signal power and the method is continuous in time. In addition larger reduction in wavelength separation between sensors in the order of 0.3nm can be achieved [63].

Finally steps need to be taken to reduce the system size to make it portable.

7.5 Summary

This chapter serves as the concluding chapter for the overall effort of this thesis. In this chapter, conclusions were presented and the existing problems, possible solutions and future works were discussed.

Appendix

A. Optical Interrogation System – The single-board microprocessor-based design.

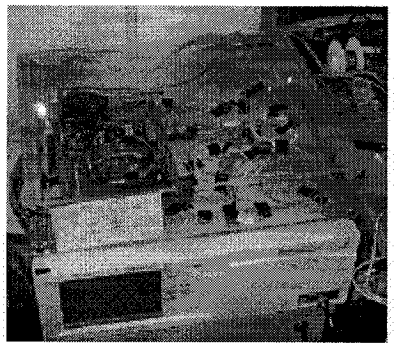

Figure A-1 Optical interrogation system.

B. Experiment Apparatus - The fiber inscribing platform.

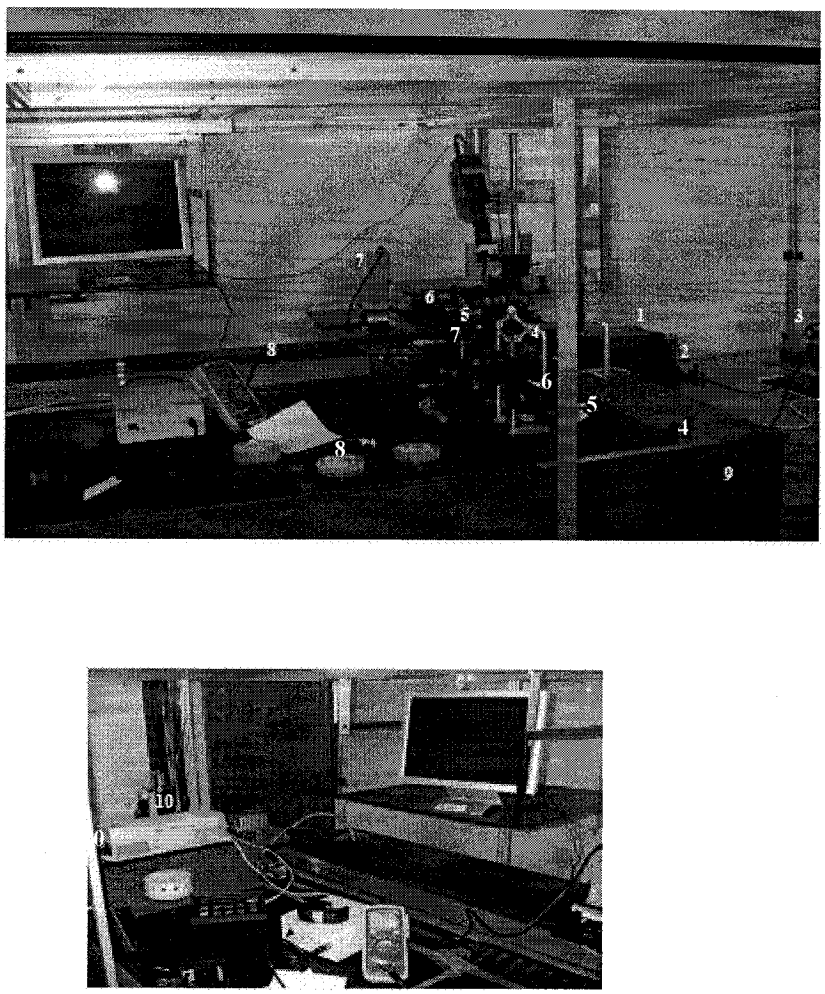

Figure B-1 (1) Ar-ion laser (2) Acoustic optic modulator (3), (4) Mirror (5) Cylinder lens (6) Phase mask (7) Strain Gauge (8) Air bearing stage (9) Granite table (10) Helium Neon laser [20].

C. Experiment Apparatus – Oven, MicroScrew.

(a)

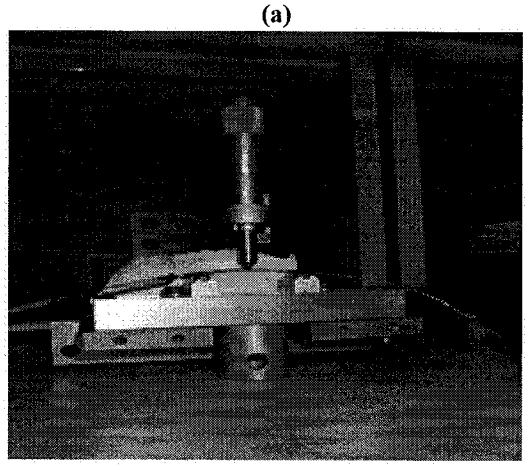

(b)

Figure C-1 (a) Sensor heated in the oven. No force is applied to it. (b) Micro-screw meter used to add force (in the form of vertical displacement) to the sensor [20].

D. Schematic – Single-board microprocessor-based design

DSP Closed-Loop FOG Processing Circuit_rev0.5.sch-1 - Tue Jan 10 09:37:46 2006

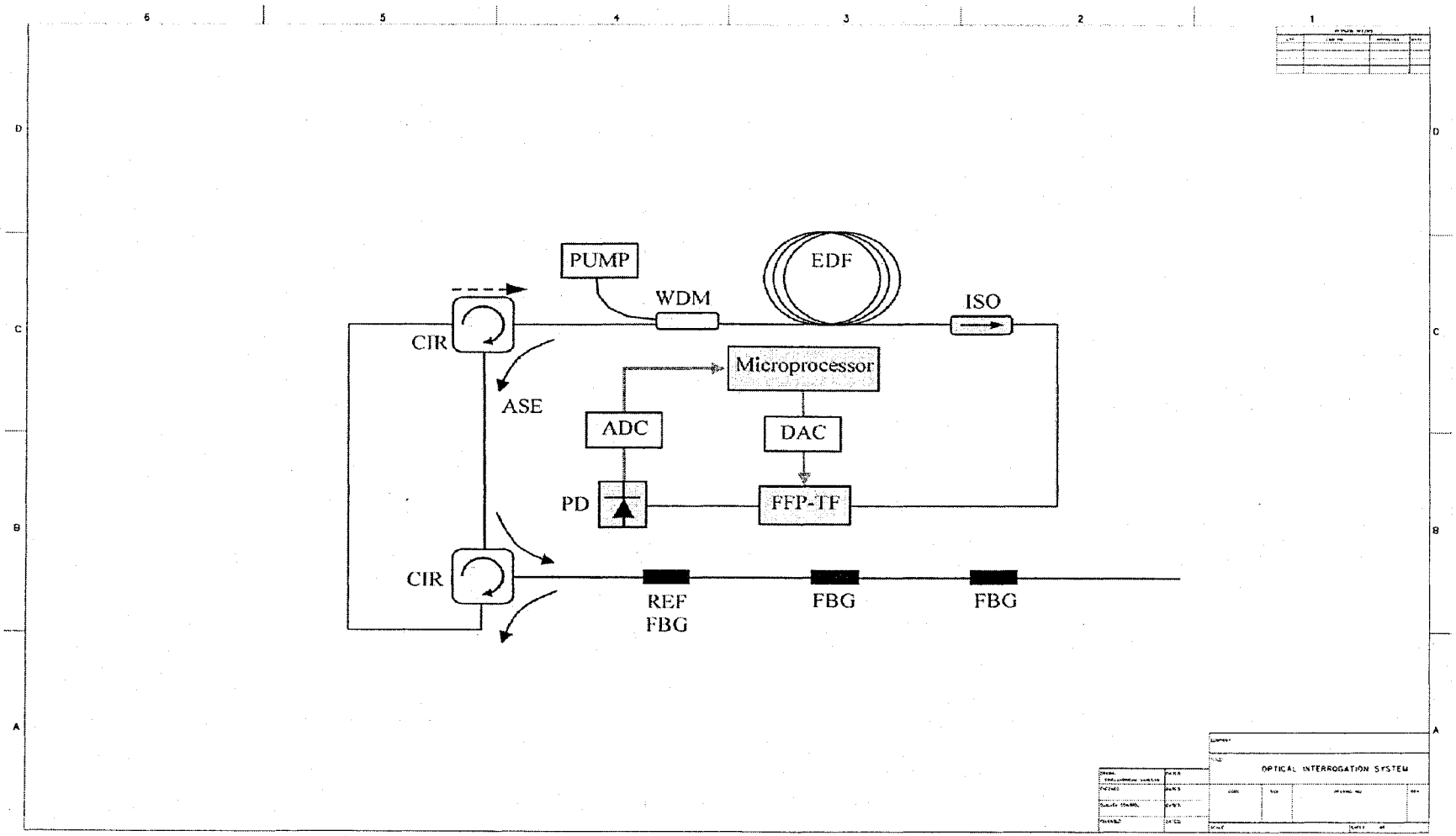

DSP Closed-Loop FOG Processing Circuit_rev0.5.sch-2 - Tue Jan 10 09:37:46 2006

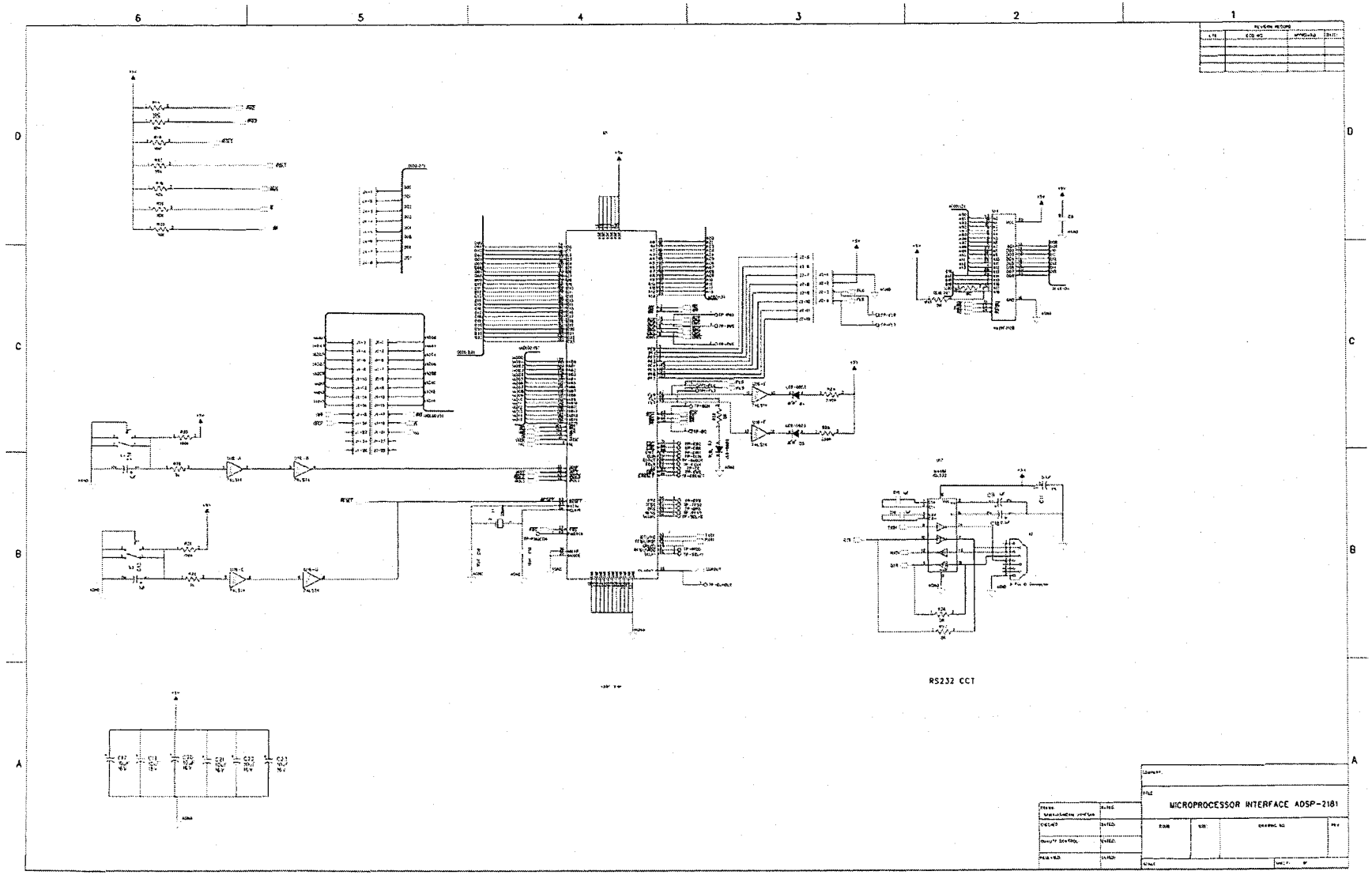

DSP Closed-Loop FOG Processing Circuit_rev0.5.sch-3 - Tue Jan 10 09:37:47 2006

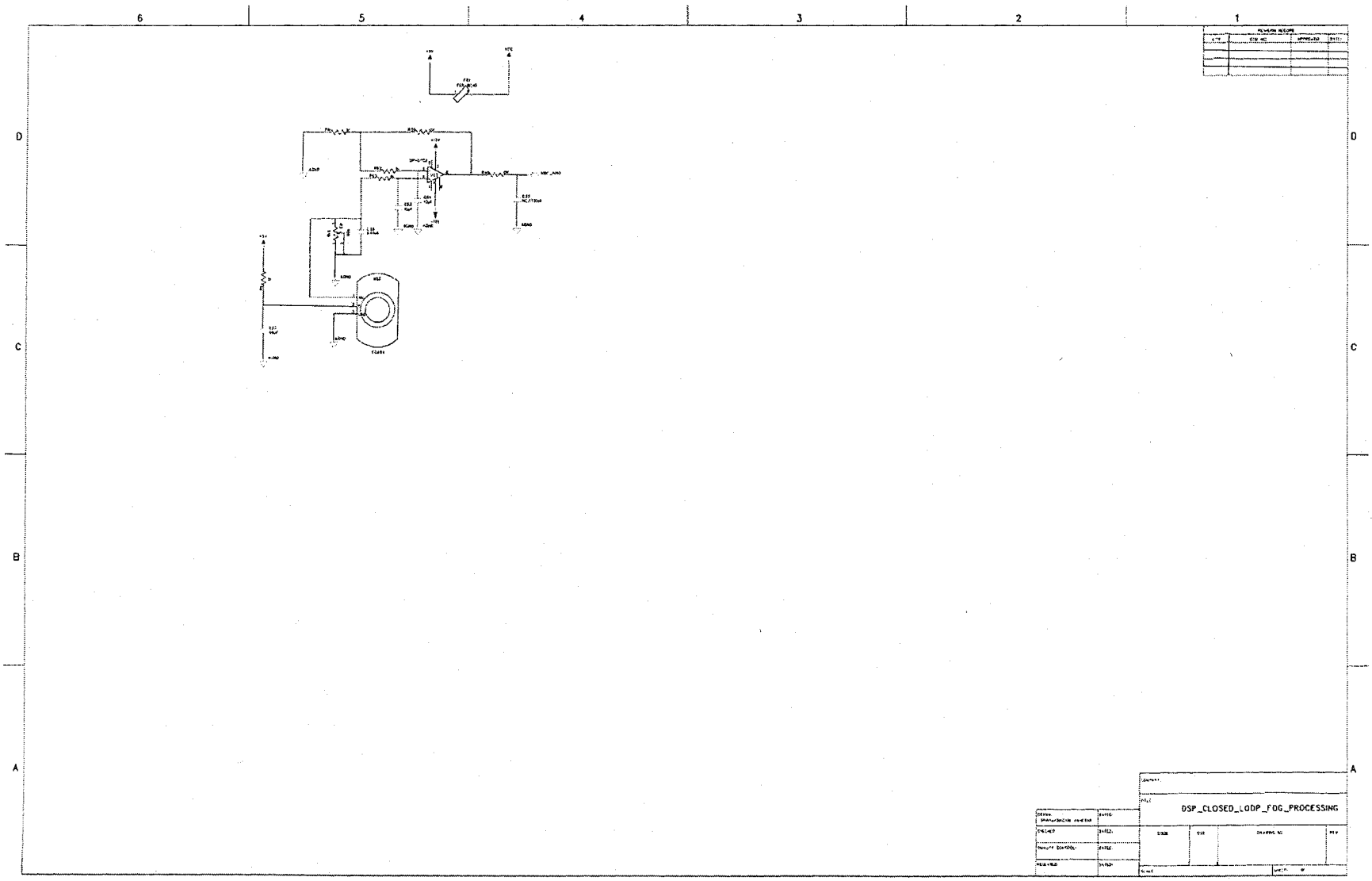

DSP Closed-Loop FOG Processing Circuit_rev0.5.sch-4 - Tue Jan 10 09:37:47 2006

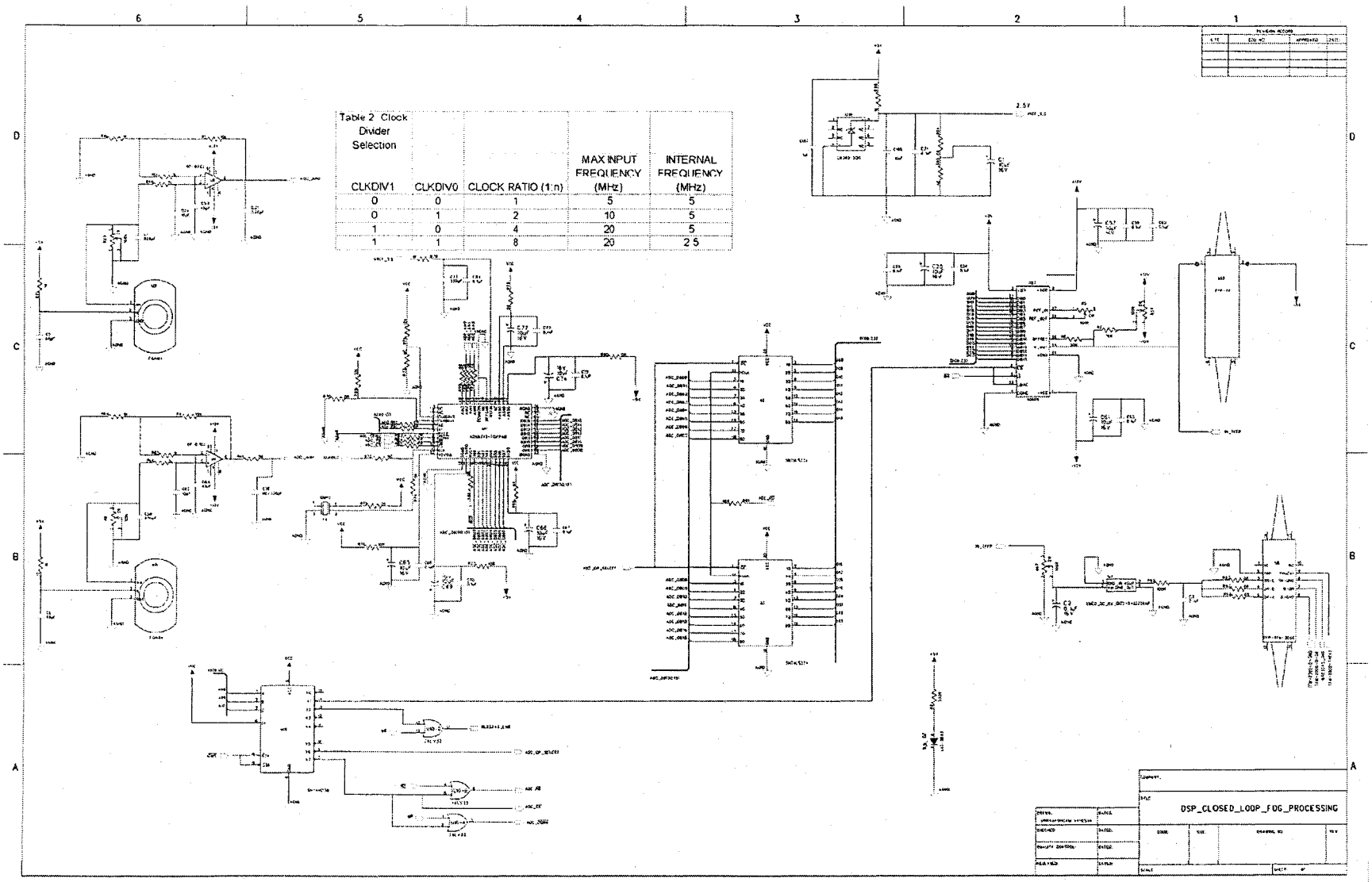

DSP Closed-Loop FOG Processing Circuit_rev0.5.sch-5 - Tue Jan 10 09:37:47 2006

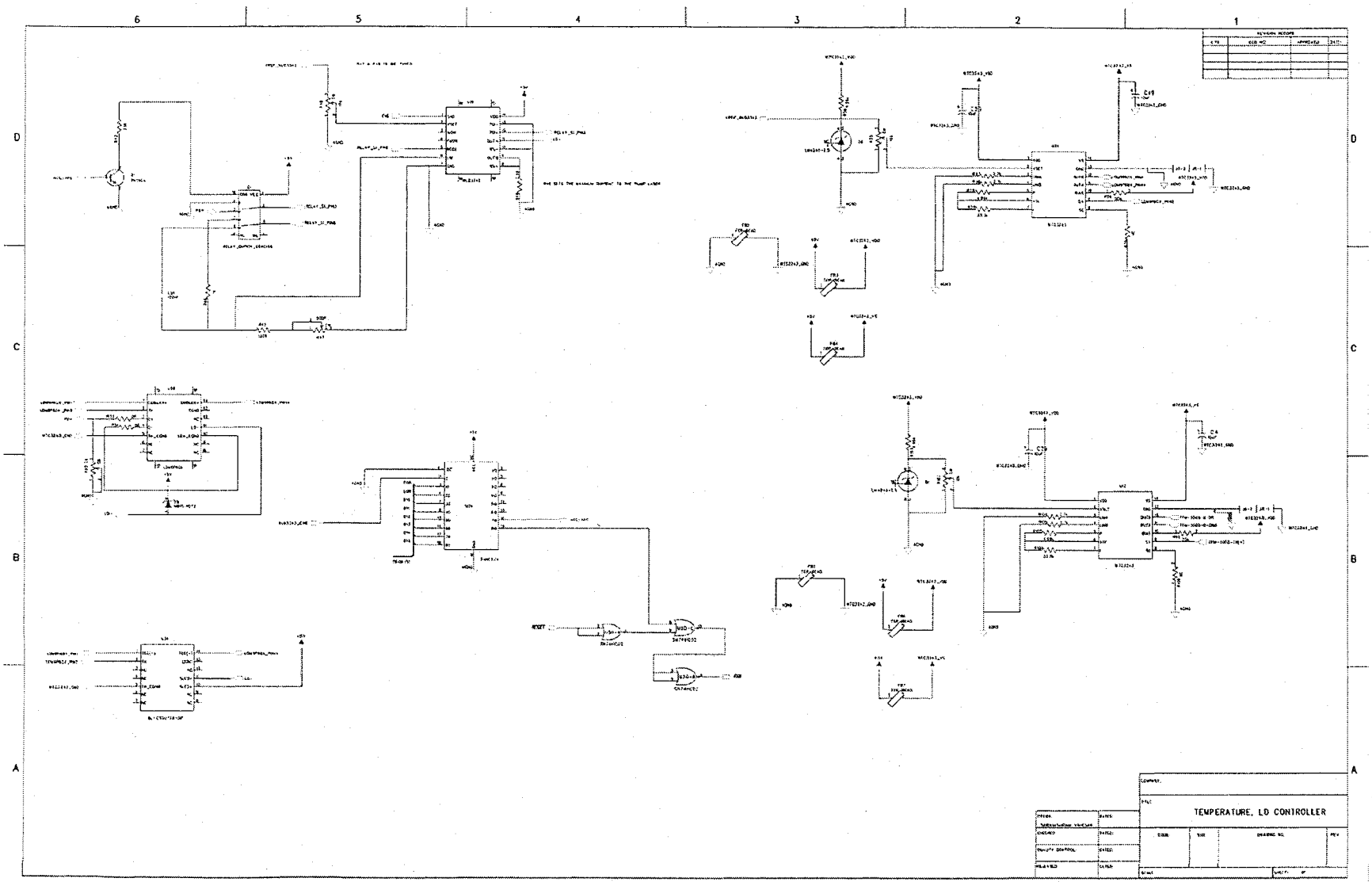

DSP Closed-Loop FOG Processing Circuit_rev0.5.sch-6 - Tue Jan 10 09:37:48 2006

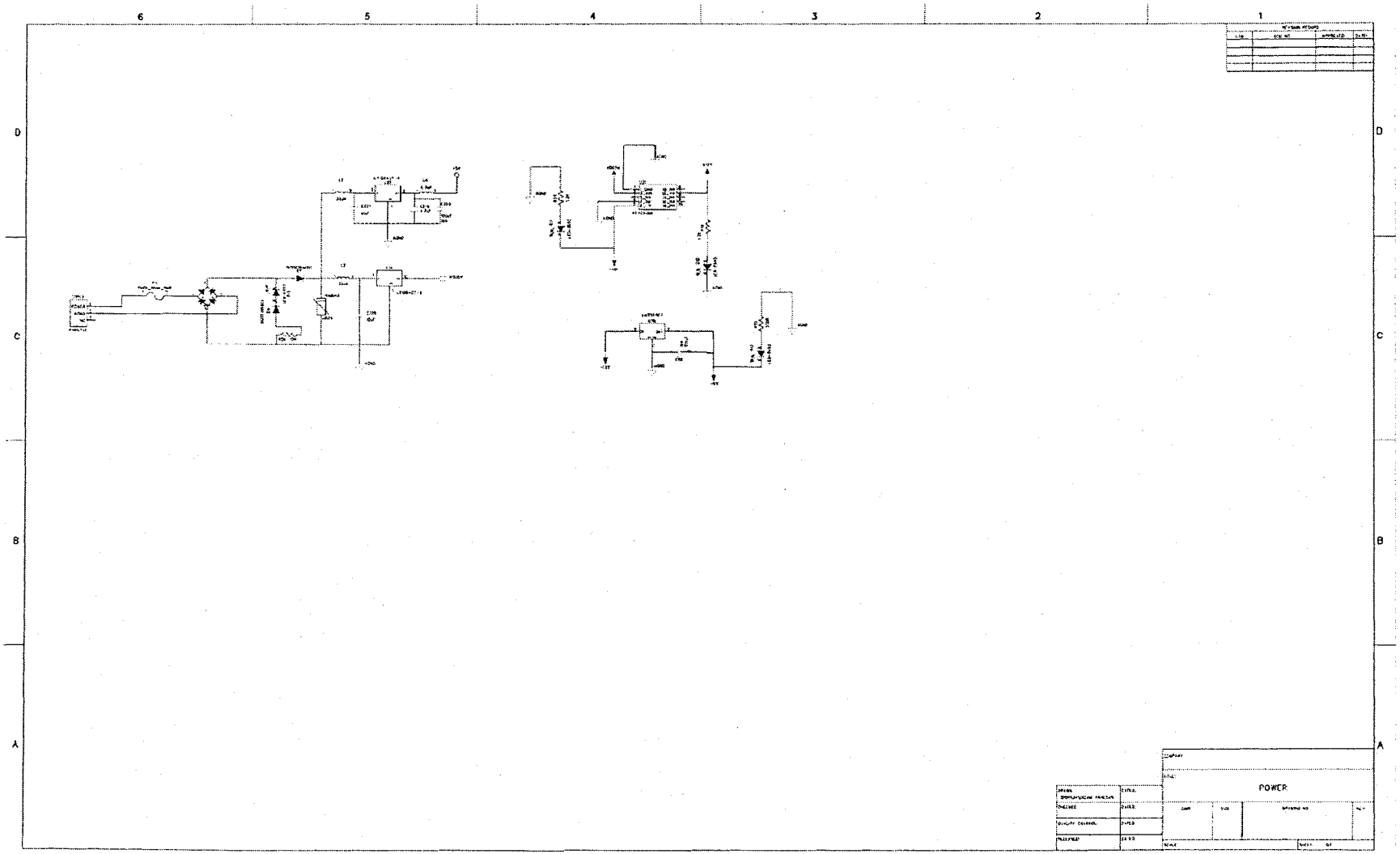

E. Printed circuit board of single-board design – Top view

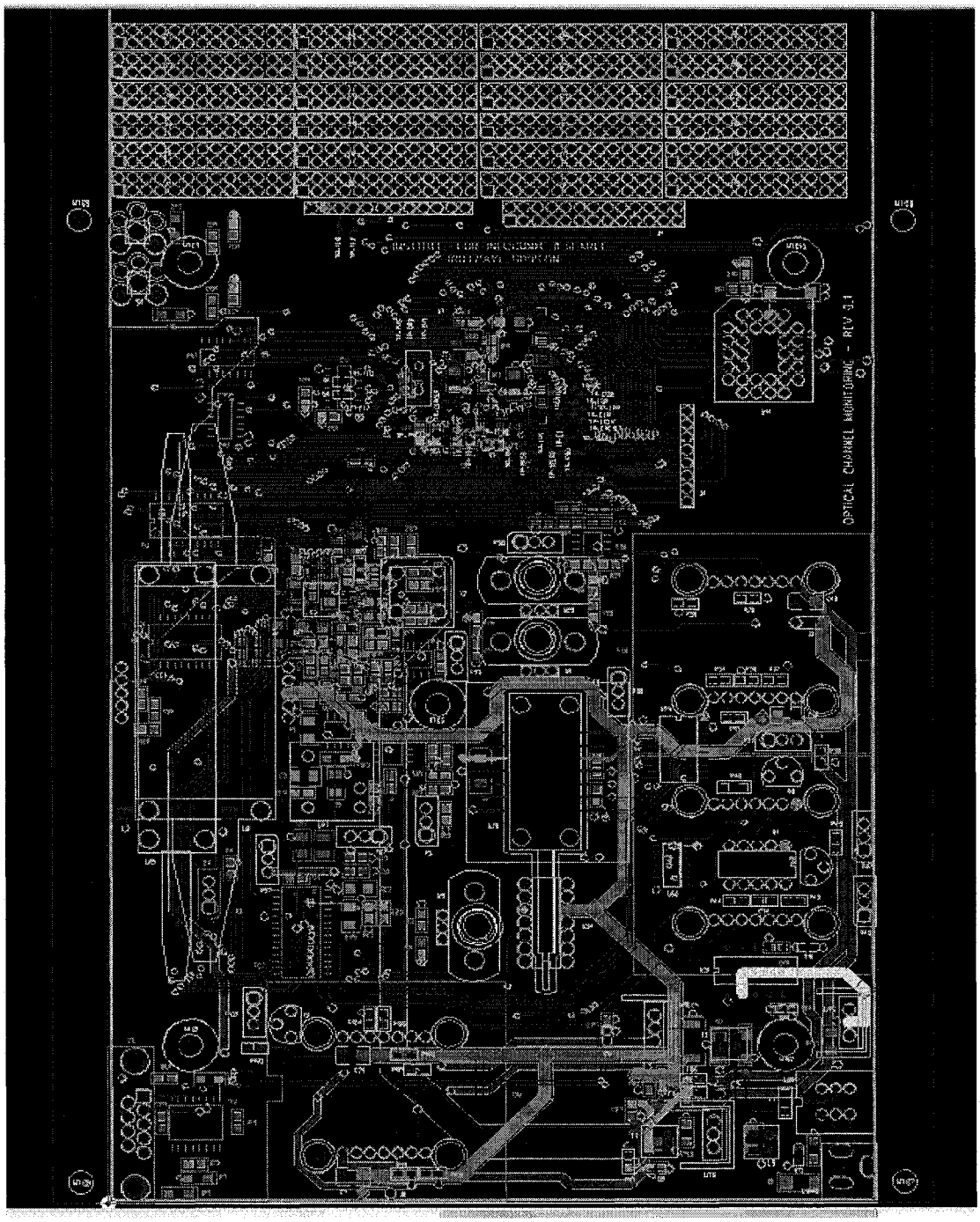

F. Printed circuit board of single-board design – Bottom view

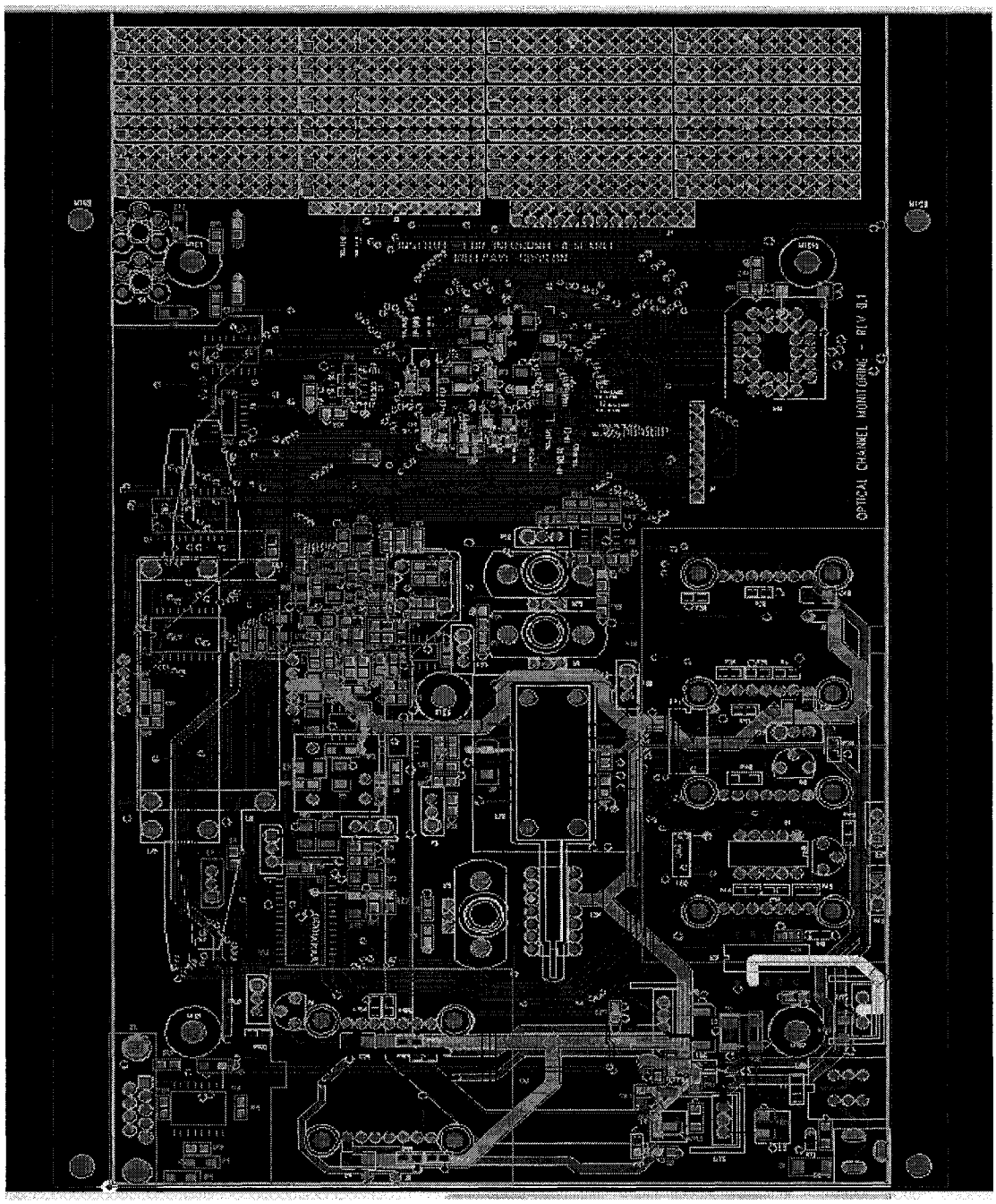

References

[1] A. Selvarajan and A. Asundi "Photonics, Fiber optics sensors and their applications in smart structures".
http://www.ntu.edu.sg/mae/Research/programmes/Sensors/sensors/fos/fosass/photonics.html

[2] Francois Ouellete, Fiber Bragg Grating Spie OE magazine January 2001.

[3] Fiber Bragg Grating – Fundamental & Applications in Telecommunications & Sensing. Edited by Andreas Othonos, Kyriacos Kalli, Artech House, Boston US, London UK, 1999.

[4] Eric Udd, 1995, Fiber Optic Smart Structures, John Wiley & Son, Inc., pp 171-665

[5] C. Z. Shi, C. C. Chan and M. Zhang, 2002, Simultaneous Interrogation of Multiple Fiber Bragg Grating Sensors for Dynamic Strain Measurements, Journal of Optoelectronics and Advanced Materials Vol. 4, No. 4, pp 937 – 941.

[6] Keiser, Gerd, 2000, Optical Fiber Communications, McGraw-Hill, Chapter 2-7, 10-11 and 13.

[7] Dutton, Harry J. R, 2002, Understanding Optical Communications, Prentice Hall, pp 261-277.

[8] Alan D. Kersey, Michael A. Davis et al. "Fiber Grating Sensors", Journal of light wave technology, Vol.15, No.8, August 1997.

[9] 3M, "Fiber Bragg Grating Application Note – The Mechanical and Optical Reliability of FBG", Feb 1996.

[10] C. Boulet, D. J. Webb, M. Douay, and P. Niay, 2001, Simultaneous Interrogation of Fiber Bragg Grating Sensors Using an Acousto-optic Tunable Filter, IEEE Photonics Technology Letters, Vol13, No.11, pp1215-1217.

[11] Gregg A. Johnson, Michael D. Todd, Bryan L. Althouse, and C. C. Chang, 2000, Fiber Bragg Grating Interrogation and Multiplexing with a 33× Coupler and a Scanning Filter, Journal of Lightwave Technology, Vol. 18, No. 8, pp 1101-1105.

[12] Anartz Unamuno and Deepak Uttamchandani, 2005, Hybrid MOEMS Tunable Filter for Interrogation of Fiber Bragg Grating Sensors, IEEE Photonics Technology Letters, VOL. 17, NO. 1, pp 202-205.

[13] P. Niewczas, A. J. Willshire, L. Dziuda, and J. R. McDonald, 2004, Performance Analysis of the Fiber Bragg Grating Interrogation System Based on an Arrayed Waveguide Grating, IEEE Transactions on Instrumentation and Measurement, Vol 53, No. 4, pp 1192-1196.

[14] Okamoto, K.; Hattori, K.; Ohmori, Y.; "Fabrication of multiwavelength simultaneous monitoring device using arrayed-waveguide grating," Electronics Letters, Volume: 32 Issue: 6, Page(s): 569 -570, 14 Mar 1996.

[15] Teshima, M.; Koga, M.; Ken-Ichi Sato; "Performance of multiwavelength simultaneous monitoring circuit employing arrayed-waveguide grating," Journal of Lightwave Technology, Volume: 14 Issue: 10, Page(s): 2277 -2285, Oct. 1996.

[16] J. Z. Hao et al., "Realization of Embedded Fiber Bragg Grating-Based Pressure Sensor in Fiber-Reinforced Composites: Embedding Techniques and Performance Characteristics", Proceedings of SPIE, Vol. 5279, 2004, pp111-125.

[17] S. S. J. Roberts and R. Davidson, "Mechanical Properties of Composite Materials Containing Embedded Fiber Optic Sensors", Proceedings of SPIE – Fiber Optic Smart Structures and Skins IV, Vol. 1588, 1991.

[18] G. P. Carman and G. P. Sendeckyij, "Review of mechanics of embedded optical sensors", Journal of Composites Technology and Research, Vol. 17, 1995, pp183-19.3.

[19] Jianzhong, Hao et al.,"Impact of embedding techniques on FBG sensors", 2004 Ninth IEEE Singapore International Conference on Communication Systems (ICCS 2004), 6-8 Sept 2004,ICCS 200, RASA Sentosa, Singapore, pp559-563.

[20] Resources from "Institute of Infocomm. Research", Light Wave Division, NTU/Singapore. http://www.i2r.a-star.edu.sg. Experiments conducted at NTU under Prof. Chao Lu and Dr. Jian Zhong Hao Emily as a wide team with number of students, technical staff and technical assistants during the years of 2004 – 2006. "Application studies of Fiber Bragg Gratings", research and experiments on "Design and Fabrication of an optical fiber sensor network" and "FBG Sensors for Sleep Monitoring" are particularly of interest. Test results are obtained with the support of Mr. Chin Yi Liaw, Mr Feng Zhang and Miss. Kai Hsing Goh and included in this thesis with the permission of Prof. Chao Lu and Dr. Jian Zhong Hao Emily.

[21] Ferninand P. Beer, E. Russell Johnston, Jr. and John T. Dewolf, Mechanics of Materials", Copyright 2000 by McGraw-Hill Higher Education, pp213-214.

[22] Raman Kashyap, "Fiber Bragg Gratings", Copyright 1999 by Academic Press, pp313.

[23] http://www.fitel.com; "Development of high power 980nm laser diode for optical amplifiers"; News release March 15, 2002.

[24] http://www.fitel.com "FOL0906A / 980nm High Power Stabilized LDM" datasheet.

[25] http:// www.wavelengthelectronics.com "WTC3243 Ultrastable Thermoelectric Controller" WTC3243-00400-A Rev D 2003 Datasheet.

[26] http:// www.wavelengthelectronics.com "WLD3343 Ultrastable Driver for Laser Diodes" WLD3343-00400-A Rev B 2001 Datasheet.

[27] Agilent 86140B optical spectrum analyzer, Application Note 1550-5,"Accurate Characterization of Source Spectra Using an Optical Spectrum Analyzer".

[28] http://www.fitel.com; 980nm/signal(C&L) WDM Coupler Data Sheet DW201-915, 916.

[29] http://www.agiltron.com;"FiberOpticWDM Coupler 980/1550nm".

[30] A.A. Rieznik et al,"Determination of Er-Fiber L-Band Gain coeffiecient from measured ASE spectra".

[31] http://www.fujikura.co.jp/optde/pdf/07edf04.pdf; "Erbium doped fiber".

[32] http://www.fitel.com;" Dielectric Filter based GFF Module" *EQ201 Series* Data Sheet November, 2001.

[33] DGE1020 Adaptive Gain Flattening.

[34] FFP-TF User Manual. URL: http://www.micronoptics.com

[35] Micron Optics Inc., "Fiber Bragg Grating Interrogation System Instruction Manual", Document #3.1a, 1997.

[36] By Jeff Kondziela, Product Line Manager, EXFO Burleigh Products Group, Application note 094,"Accurately measure laser spectral characteristics".

[37] http://www.web-ee.com/primers/files/photodiodes.htm; "A primer on photodiode technology".

[38] Sedra, Adel S., Microelectronic Circuits, Oxford University Press, Chapter 12.

[39] Hambley, Allan R, 2000, Electronics, Prentice Hall, Chapter 2&6.

[40] Franco, Sergio, 2002, Design with Operational Amplifiers and Analog Integrated Circuits, McGraw-Hill, Chapter 3&4.

[41] Millman, J. and Halkias, C. Electronic Fundamentals for Engineers and Scientists, McGraw-Hill, New York, pp. 332-336, 1976.

[42] Tjin S.C.; Hao J. et al, "A Pressure Sensor Using Fiber Bragg Grating" Fiber And Integrated Optics, Volume 20, Number 1, 1 January 2001, pp. 59-69(11).

[43] Rex M. Craig, Chih-Ming Wang, "Measurement Assurance Program for Wavelength Dependence of Polarization Dependent Loss in Fiber Optic Devices over the Wavelength Range from 1535nm to 1560nm", NIST Special Publication 250-60.

[44] Captured from the screen when the system was integrated. LabView Software done by another team inside NTU. Resources from Nanyang Technological University, Singapore. http://www.i2r.a-star.edu.sg

[45] "Risk Assessment & Prevention of Pressure Ulcers", Nursing Best Practice Guideline Shaping the future of Nursing, March 2005.

[46] http://www.i2r.a-star.edu.sg/files/phatfile/ ; Resources from Nanyang Technological University; Singapore.

[47] http://www.la4seniors.com/bedsores.htm

[48] http://www.injuryboard.com/view.cfm/Topic=266

[49] www.fria.org/html/fria2_pressuresores.htm

[50] Smith, D. M. "Diagnosis and Treatment Pressure Ulcers in the Nursing Home"; Annals of Internal Medicine, 15 September 1995, Volume 123 Issue 6 , Pages 433-438.

[51] Micron Optics Inc., URL: http://www.micronoptics.com

[52] Erdogan T. and Mizrahi V., "Decay of UV induced fiber Bragg gratings," Proc. Optical Fiber Conference, OFC'94, pp50 (1994).

[53] Kapron PF.P. and Yuce H.H., "Theory and Measurement for predicting stressed fiber lifetime", Opt. Eng. 30(6), 700-708 (1991).

[54] Dr. Martin Guy and François Trépanier; "State-of-the-Art Manufacturing Techniques Push Fiber Bragg Gratings Components to New Levels of Performance"; Photonics Spectra March 2002.

[55] Jae-Hoon Lee; Tae-Yong Kim; Tae-Hoo Kim; Jae-Seung Lee; Chang-Soo Park; Wan-Seok Seo; "Arrayed-waveguide grating with branched outputs for simultaneous multichannel monitoring purposes," Photonics Technology Letters, IEEE , Volume: 13 Issue: 11 , Page(s): 1185 -1187, Nov. 2001.

[56] Tongxin Lu; Zheng Yan; "Optical performance monitor with tunable filter and simultaneous gas cell wavelength reference," Optical Fiber Communication Conference and Exhibit, 2002, OFC 2002, Page(s): 752 -753, 17-22 March 2002.

[57] W. H. Chung, H. Y. Tam, M. S. Demokan, P. K. A. Wai and C. Lu, "Wavelength and power monitoring of DWDM systems using scanning F-P filter calibrated with a F-P laser," Optics Communications, Pg 1-6, August 2002.

[58] Martin Nord, "Optical Switching Technologies for optical line-burst and packet switches"; Scientific Report R 32/2002. ISBN 82-423-0561-7. 30-5-2002.

[59] http://www.lightconnect.com/products/dge_dge.shtml

[60] Kuo, Sen M., 2005, Digital Signal processors: Architectures, Implementations, and Applications, Pearson Prentice Hall, Chapter 9.

[61] Widrow, Bernard, 1985, Adaptive Signal Processing, Prentice-Hall, Chapter 1&6.

[62] Hojoon Lee, 2002, Multiple fiber Bragg grating sensor system using code-division multiple access, APPLIED OPTICS, Vol. 41, No. 25, pp 5245-5248.

[63] Lee; Ho-Joon et al, "Signal processing system of multiplexed fiber bragg grating sensor using CDMA"; US Patent: 6,892,031: applied July 19, 2001.

[64] http://www.o-netcom.com/file/products/voa/1x2,2x2%20Optical%20Switch.pdf

[65] Ronald J. Tocci, 1995, Digital Systems, Principles and Applications, Prentice Hall, Chapter 1&10.